UNIVERSIDADE FEDERAL DO RIO GRANDE DO SUL
INSTITUTO DE FÍSICA
Programa de Pós-Graduação em Física

Mixing, space-charge and thermal effects in free-electron lasers

Eduardo Alcides Peter

A THESIS SUBMITTED TO THE INSTITUTO DE FÍSICA OF UNIVERSIDADE FEDERAL DO RIO GRANDE DO SUL IN PARTIAL FULFILLMENT OF THE REQUERIMENTS FOR THE DEGREE OF DOCTOR OF PHILOSOPHY

Advisor: Prof. Dr. Felipe Barbedo Rizzato - UFRGS
Co-Advisor: Prof. Dr. Antonio Endler - UFRGS

Porto Alegre, RS
2016

Abstract

Free-Electron Lasers (FELs) are devices which efficiently convert the kinetic energy from a relativistic electron beam into the energy of coherent electromagnetic modes. Energy is drawn from the electron beam, as electrons are trapped in the ponderomotive well formed by the simultaneous action of the electromagnetic mode and wiggler field. In this work we describe a FEL, its components, different types and regimes of operation. After the derivation of the particles-wave equations to describe the system evolution, we propose a model based on the compressibility factor to estimate the results given by the simulations. The laser growth was emulate through a linear set of equation obtained by the linearization of the particles-wave equations. The space-charge and thermal nonlinearities were kept for the second order differential equations that represent the evolution of the particles. The model is transformed according to the initial conditions: first, we considered a cold beam (no beam initial energy spread); second, we considered a water bag distribution for the longitudinal velocity; and, at last, we considered a Gauss distribution for the longitudinal velocity. For the cold beam, the zeroes of the compressibility indicates the onset of the mixing process (the mixing occurs when the distribution is not a single valued function in the phase-space energy-position anymore). While for the warm beam, the breakdown of the laminar regime occurs when the lower border of the distribution becomes a non single valued function. The warm beam analysis is limited to very small velocity spreads, in the hydrodynamical regime − in which the beam is expressed as a fluid. The model was compared with particles-wave simulations, in all cases, with well agreement with them and proved to be able to estimate some relevant physical quantities of interest in FELs. This way, the simplified model could be used as a powerful tool to produce reasonable reliable data for the optimization of the device operation.

Resumo

Free-Electron Lasers (*FELs*) são dispositivos que convertem eficientemente a energia cinética de um feixe relativístico de elétrons na energia de modos eletromangéticos de forma coerente. A energia é retirada do feixe de elétrons, na medida em que os elétrons são aprisionados no potencial ponderomotriz formado pela ação simultânea dos campos do modo eletromagnético e do *wiggler*. Neste trabalho descreve-se um *FEL*, seus componentes, diferentes tipos e regimes de operação. Depois da derivação das equações de partículas-onda para descrever a evolução do sistema, propõe-se um modelo baseado no fator de compressibilidade para estimar os resultados gerados pelas simulações. O crescimento do campo do laser é emulado através de um conjunto de equações lineares obtido pela linearização das equações de partículas-onda. As não linearidades causadas pelo efeito de carga espacial e térmico são mantidos nas equações diferenciais de segunda ordem que representam a evolução das partículas. O modelo é transformado, ao longo do trabalho, de acordo com as condições iniciais: primeiro, considera-se um feixe gelado (sem distribuição inicial de energia); segundo, considera-se uma distribuição do tipo *water bag* para a velocidade longitudinal das partículas; e, por fim, considera-se uma distribuição de Gauss para a velocidade longitudinal. Para o feixe gelado, os zeros da compressibilidade indicam o início do processo de mistura no espaço de fases (a mistura acontece quando a distribuição não é mais uma função de valor único no espaço de fases energia-posição). Enquanto para o feixe quente, a quebra do regime linear ocorre quando a borda inferior da distribuição passa a não ser mais uma função de valor único. A análise para o feixe quente é limitada a pequenos valores de distribuição de velocidades, dentro do regime hidrodinâmico − no qual o feixe pode ser expresso como um fluido. O modelo foi comparado com as simulações de partículas-onda, em todos os casos, apresentando uma concordância satisfatória nos resultados. O modelo provou ser capaz de estimar algumas quantidades físicas de interesse para *FELs*. Deste modo, o modelo simplificado pode ser usado como uma ferramenta poderosa para produzir dados razoavelmente confiáveis para a otimização da operação do dispositivo.

Contents

Chapter 1

Introduction

Electromagnetic waves are everywhere, even without human being presence. Without them, life would not be possible. Nowadays, the generation of coherent electromagnetic waves (with well-defined frequency and same phase) has great importance to the scientific and technological development, in different areas of knowledge, as physics, medicine, chemistry and biology, in a wide range of wavelengths. In telecommunication, for example, radio waves have wavelengths from $1\ millimeter$ to $100\ kilometers$.

Through the invention of LASER (Light Amplification by Stimulated Emission of Radiation), in 1954 (Charles Townes and Arthur Schawlow invented, in this year, the MASER, Micro-wAve Stimulated Emission of Radiation, before the optical LASER, using ammonia gas and microwave radiation), it was possible to generate radiation in infrared, visible and near UV regions of spectrum, contributing a lot in the development of science. Laser is based in population inversion of an atomic or molecular medium. However, the spatial resolution of the laser is limited by several factors, including the overheating of the medium and the generation of a series of non-linear phenomena that reduce the quality of radiation, being far from the atomic scale ($\cong 1\mathring{\mathrm{A}}$).

In this context, a search arises for a device that is able to produce intense and coherent radiation in the X-rays region of the spectrum. In this region, it is possible, for example, determining the structure of crystalline materials[1, 2, 3].

In 1953, Motz and his group made an electron bunched beam, accelerated by a linear accelerator at Stanford University, pass within an undulador (is a device which produces a spatially periodic magnetic field). It was observed coherent radiation emission, with few millimeters of wavelength. This wavelength was close to the distance between the electrons bunches, generated by the linac (linear accelerator). Motz wrote that collective effects due the bunching process are the responsible by the coherent radiation. In the work about the experiment, the authors treated the results as, in their words, promising[4].

Later, in 1971, Madey published a paper[5] suggesting similar device geometry as proposed by Motz, but not requiring an initially bunched beam. According to his theory, an appropriate combination of radiation wavelength, wavelength of the external magnetic field (this wavelength is related to the distance between the magnets in undulators and wigglers) and electron injection energy could amplify the laser field, i.e., the radiation field. Without the initially bunched beam restriction, this device would then be able to generate coherent electromagnetic radiation in a wide spectrum width. To show its potentiality, Madey, in this work, also calculated the gain for Compton scattering. It was the beginning of free-electron laser (FEL) (the name free-electron laser was coined by John Madey in 1976 at Stanford University) theory[5, 6]. In 1977, Madey and his group published an article[7] about the first operation of a FEL, corroborating the idea that this device could be used to generate radiation in many different frequencies.

In few words, the FEL is a device in which an electromagnetic wave co-propagates with a relativistic electron beam in a wiggler. For correct initial injection conditions, seen in this work, the superposition of radiation and wiggler vector potentials creates a spatially periodic potential, in a stationary approach, which confines electrons in its bottom, called ponderomotive potential, forming bunches. These bunches emit coherent radiation, losing kinetic energy, increasing exponentially the amplitude of the laser wave until nonlinear processes begin to dominate the system dynamics, leading to the saturation of the laser field. Many studies were done in order to estimate the gain, the maximum growth rate, the efficiency and to understand the processes involved in the FEL[6, 8, 9, 10, 11, 12, 13, 14, 15].

The present work is divided in six main topics:

I. A brief description of the FEL types, regimes, physics and dynamics: To understand the FEL dynamics, it is necessary to know its principles of operation, which and how are its components, the different types of FEL, the different regimes of operation and the physics behind its operation. These topics are shown in Chapter 2.

II. Development of the particles-wave equations: After a brief description of the FEL, in Chapter 3, we start the development of the particles-wave equations to describe the evolution of the main physical quantities of interest of each particle (phase and energy), as well the wave evolution. With this set of equations is possible to derive the famous FEL pendulum equation, in the limit of a single electron. To build this set of equations, we make a lot of considerations, as an unidimensional system, an infinite electron beam, a single pass configuration, and, initially, a static and spatially periodic magnetic field produced by a wiggler. Space-charge effects were considered only in the longitudinal direction.

III. Development of a semi-analytical model to describe FEL dynamics in the case of a monoenergetic electron beam: In Chapter 4, a semi-analytical model to describe the system evolution in the case of an initially monoenergetic electron beam is proposed. The laser field evolution is emulated by a set of linear equations. This set of equations was derived from the particles-wave equations, through the introduction of collective variables. The nonlinearities of the system were introduced through the connection between the longitudinal velocity and the energy. This connection made possible the use of the compressibility factor, which zeroes indicate the onset of mixing and the end of the linear regime of the FEL. The model proved to be an useful tool to predict the time until the onset of mixing, the saturated amplitude of the laser field and to delimit Compton and Raman regimes (in Compton/Raman regime, the space-charge effect is insignificant/significant for the system evolution).

IV. Development of a nonlinear model to describe FEL dynamics, including thermal effects, considering a water bag initial distribution for the particles velocities: In Chapter 5, we develop a nonlinear model able to deal with thermal effects, exploring the Vlasov equation and the hydrodynamical regime (the spread must be very small). The beam is treated as a fluid with pressure, where

the pressure depends on the initial velocity spread: the pressure becomes an extra term to be add in the linear set of equations. We consider a water bag distribution for the longitudinal velocities. The compressibility factor is used again to predict the breakdown of the laminar regime. But, because of the pressure term, the compressibility cannot vanishes. Thus, the signature of the breakdown is the discontinuity in the compressibility (and also in the longitudinal electron density $-$ once the compressibility is the inverse of the density). The results shows a good agreement between the particles-wave simulations and the nonlinear model.

V. Introduction of Gaussian distribution for the longitudinal velocity and the equivalent initial spread concept: The nonlinear model can be expanded for other distributions. In the end of Chapter 5, we apply the nonlinear model for Gaussian distributions. In the limit of spreads which we are interested in, these two distributions are equivalent. Thus, we define an equivalent initial spread (we build the original distribution through a sum of water bag distributions and we relate the spread of each water bag distribution and its area bellow the original distribution). This equivalent initial spread is based on the superposition of different fluids, and it is valid in the hydrodynamical regime because the density in the phase-space of each fluid is conserved. Once again, the particles-wave simulations produced results close enough to the nonlinear model.

VI. Final remarks and future perspectives of work: At last, in Chapter 6, the final remarks and future perspectives of the work are presented. As a perspective, we expect to extend the understanding of the FEL introducing transverse space-charge effects and another $3D$ effects. We plan, also, to study the case of a another electromagnetic wave to act as the wiggler.

Chapter 2

Principles of Operation of Free-Electron Laser

As already stated, the FEL is a device capable to efficiently convert kinetic energy from a relativistic electron beam into electromagnetic energy in the form of radiation. To make this possible, the beam and the electromagnetic wave to be amplified (the radiation) propagate in a spatially periodic magnetic field, produced by a wiggler. The combined action of the wiggler and radiation fields forms the ponderomotive potential, which is responsible for the energy conversion[16, 17, 18].

2.1 Components of the Free-Electron Laser

A FEL is composed, as can be seen in Fig. 2.1, by: a particle accelerator, which provides the high energy (relativistic) electron beam; a transport system to drive the beam to the wiggler; a wiggler to generate the spatially periodic magnetic field; and, for the oscillatory configuration of FEL, a resonant cavity[6, 11].

Two configurations of FEL are used: oscillator type and single pass. FELs oscillators have resonant cavity, and for this reason are applied only for radiation wavelengths contained in the spectrum bands where it is possible to produce mirrors with extremely high efficiency. This type of configu-

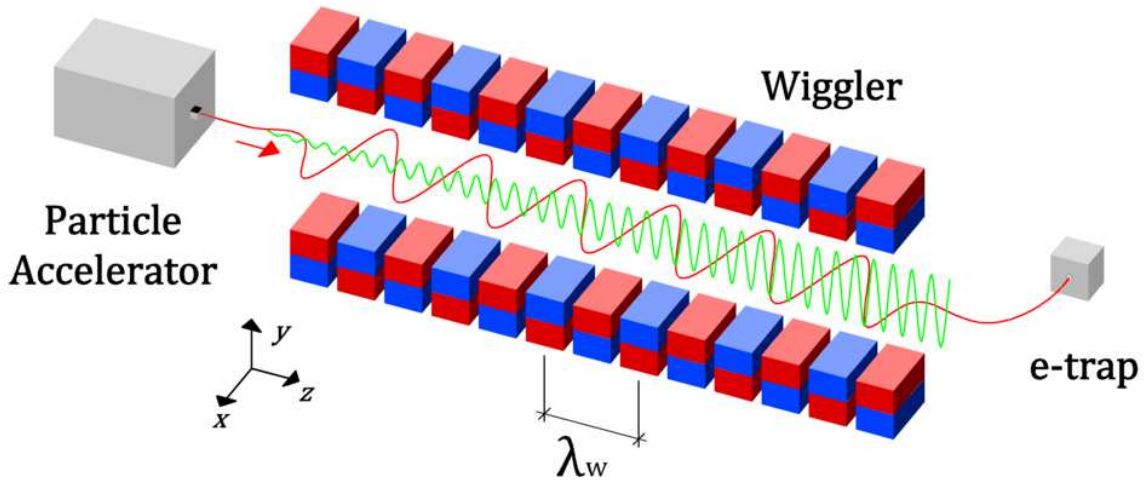

Fig. 2.1: To the left of the figure is the particle accelerator that feeds the FEL with a relativistic electron beam. The beam passes through the wiggler, composed of alternated magnets, and, in red, its deflected trajectory, in the perpendicular direction, while in green is shown the ponderomotive potential.

ration usually works in the limit of small signal gain and to be viable requires that the signal gain exceeds the losses occurring in the resonant cavity and, in particular, in the mirrors. This type of configuration demands shorter wiggler lengths[19, 20]. The present work considers only the single pass configuration, in which all the energy transfer occurs on one beam passage by the wiggler. Then, the whole discussion refers to this configuration.

2.1.1 Particle Accelerators

Particle accelerators are devices that use electromagnetic fields to accelerate beams. There are several types of accelerators, including electrostatic generators (the acceleration process is due to an

electrical potential difference and for this reason they are limited to the electric breakdown of the medium), cyclotron magnetic resonance accelerators, betatrons, linear particle accelerators, synchrocyclotrons, cyclic accelerators and many others[21].

2.1.2 Wigglers

The two most common geometries for the wigglers are the helical and the planar. Helical wigglers generate helical magnetic fields, with spatial periodicity along its axis of symmetry. Planar wigglers generate uniform magnetic fields in transverse direction with spatial periodicity along its length. Examples of wigglers formed by magnets are shown in Fig. 2.2.

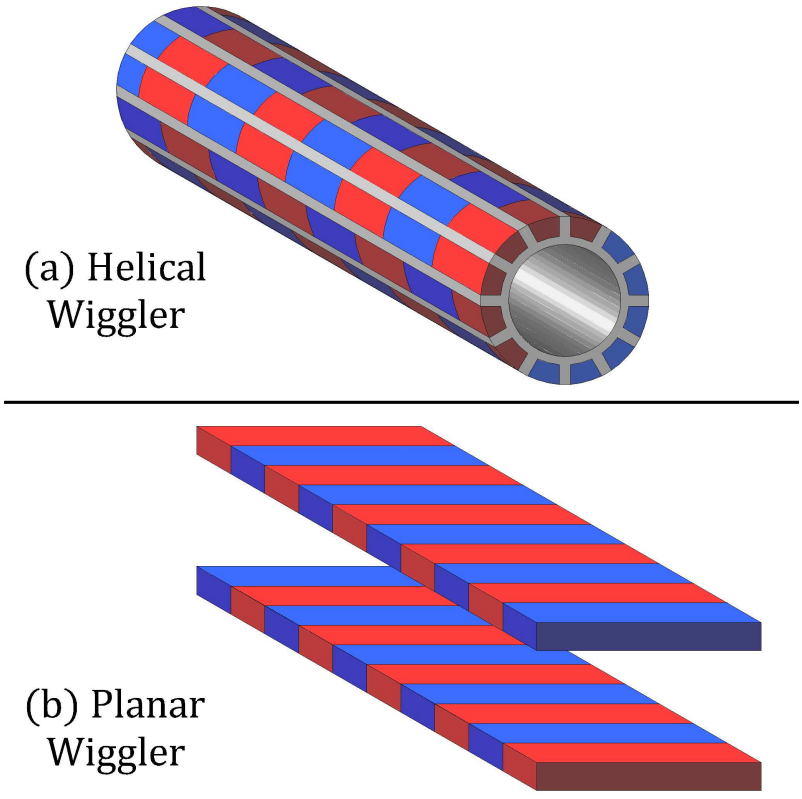

Fig. 2.2: Two common wiggler configurations. Each hatching symbolizes a different direction of the magnetic field generated by each magnet. In the panel (a), an example of helical wiggler, where the magnets arrangement is delayed to generate spatially-periodic magnetic field. In the panel (b), an example of planar wiggler, where magnets are rotated to generate a sinusoidal magnetic field.

2.2 The Physics of Free-Electron Laser

A single pass FEL can operate in three different ways. In *spontaneous emission FELs*, no radiation field is excited before the entrance of the electron beam into the wiggler. While in the *stimulated emission FELs*, a radiation field copropagates with the electron beam (this radiation field can be produced by another laser), and the electrons interact with the radiation and the wiggler fields. In the stimulated emission FELs, current densities are so small that the system dynamics is analyzed as a collection of single particles dynamics. At last, the *high gain* FELs, the most interesting of them and the one studied in the present work. In this case, electrons interact with the radiation and the wiggler fields and with themselves (this interaction is called space-charge effect). There are collective processes which lead to instabilities and exponential growing of the radiation field[11].

2.2.1 Spontaneous Emission FEL

When a relativistic charged particle, without being excited by a radiation field, is injected into a spatially periodic and transverse magnetic field, its trajectory has helical (for helical wigglers) or sinusoidal (for planar wiggler) behavior and, due to this change of the direction, the particle emits spontaneously radiation. This form of radiation is called synchrotron radiation. One of its most important features is that radiation is not emitted in all directions: the radiation is confined to a region that forms a cone with opening α ($\cong mc^2/\varepsilon = 1/\gamma$, where m, ε and γ are respectively the mass, the energy and the Lorentz factor of the particle) with respect to the vector of instantaneous velocity of the particle. The wavelength of radiation, seen in the laboratory frame, is obtained by a few steps[11, 22].

Considering the presence of a planar wiggler, the vector potential associated to the wiggler is described by:

$$\vec{A}_w(z) = \frac{mc^2}{e}\frac{a_w}{\sqrt{2}}\left(e^{-ik_w z} + e^{ik_w z}\right)\hat{x}, \tag{2.1}$$

where m and e are respectively the mass and the charge of the particle and $a_w (= e\lambda_w B_w/2\pi mc^2)$ is

the dimensionless amplitude of wiggler vector potential. The oscillation frequency associated to the wiggler, ω_w, is written as:

$$\omega_w = k_w c = \frac{2\pi}{\lambda_w} c, \tag{2.2}$$

where k_w and λ_w are the wavenumber and the wavelength of the wiggler field.

In a frame moving with the particle, the oscillation frequency of the particle is changed due to the Lorentz transformation ($\tilde{\omega}_w = \omega_w/\gamma$). In this frame, the particle oscillates perpendicularly and emits radiation in all directions.

Finally, to find the oscillation frequency of the particle in the laboratory frame, ω_0, it is necessary to apply relativistic Doppler effect. Then:

$$\omega_0 = \sqrt{\frac{1+\beta_z}{1-\beta_z}}\tilde{\omega}_w = \frac{1+\beta_z}{1-\beta_z^2}\omega_w, \tag{2.3}$$

where β_z is the light-speed-normalized longitudinal velocity of the particle.

Performing approaches for highly-relativistic regime, $\beta_z \to 1$, and solving Lorentz equation for the transverse direction (the solution is given by $|\beta_x| = a_w/\gamma$), we obtain:

$$\lambda_0 = \frac{(1+{a_w}^2)}{2\gamma^2}\lambda_w, \tag{2.4}$$

where λ_0 is the radiation wavelength in the laboratory frame.

This radiation source has a narrow bandwidth at half height, depending on the number of periods of the wiggler, N_w, ($\Delta\omega/\omega \approx 1/N_w$) and the intensity of the radiation increases proportionally with the number of particles. However, the phase of the radiation depends primarily on the time that the particle enters the wiggler. Since there is a random initial distribution of particles, the phase of the radiation generated by each particle is also random. This is a huge problem when we want a coherent source of radiation.

Usually, the electron beam energy varies from few MeV to few GeV. The wiggler period is in

$\lambda_w(cm)$	a_w	$B_w(T)$	v/c	γ	$\lambda_0(\mu m)$
	0.2	0.043	0.990	7.229	497.5
5	0.3	0.064	0.990	7.401	497.5
	0.2	0.043	0.999	22.81	49.97
	0.2	0.021	0.990	7.229	995.0
10	0.3	0.032	0.990	7.401	995.0
	0.2	0.021	0.999	22.81	99.95

Tab. 2.1: The table presents the radiation wavelength λ_0 for different values of the λ_w, B_w and γ. It is important to notice the high v dependence to change λ_0. For $a_w = 0.2$, $\lambda_w = 5cm$ and $\gamma = 7.229$, the radiation wavelength is ~ 100 times smaller than the wiggler wavelength.

the range of few centimeters ($\lambda_w > 2\,cm$). The wiggler field strength B_w is in the range of some KG, while the wiggler length is between 2 and 20 m. Some physical (and realistic) values for the Eq. (2.4) can be seen in the Table 2.1.

2.2.2 Stimulated Emission FEL

In stimulated emission FELs, a radiation field copropagates with the electron beam along the wiggler. Thus, the electrons undergo the presence of the wiggler and radiation fields[8]. The current densities are so low that the system dynamics is analyzed as a collection of single particles dynamics[11]. Assuming that λ is the radiation wavelength, the phase between the radiation and the transverse oscillations remains constant if the energy of the electrons respects a relation obtained through Eq. (2.4):

$$\gamma_r = \sqrt{\frac{(1 + {a_w}^2)\,\lambda_w}{2\lambda}}. \tag{2.5}$$

That energy, γ_r, is called resonant energy.

Considering the presence of the same planar wiggler seen before, the vector potential associated to the wiggler would be described by:

$$\vec{A}_w(z) = \frac{mc^2}{e}\frac{a_w}{\sqrt{2}}\left(e^{-ik_w z} + e^{ik_w z}\right)\hat{x}, \tag{2.6}$$

while the radiation vector potential (with radiation frequency $\omega = kc = 2\pi c/\lambda$) would be described by:

$$\vec{A}(z,t) = -i\frac{mc^2}{e}\frac{1}{\sqrt{2}}\left(ae^{i(kz-\omega t+\phi)} - a^* e^{-i(kz-\omega t+\phi)}\right)\hat{x}. \tag{2.7}$$

Neglecting the interaction between the electrons, the electron dynamics obeys the Lorenz Equation:

$$\frac{d\left(\gamma m\vec{v}\right)}{dt} = e\vec{E} + e\frac{\vec{v}}{c}\times\vec{B}. \tag{2.8}$$

Using that:

$$\vec{B} = \vec{\nabla}\times\vec{A} = \vec{\nabla}\times\left(\vec{A}_w + \vec{A}\right), \tag{2.9}$$

and:

$$\vec{E} = -\frac{1}{c}\frac{\partial}{\partial t}\vec{A}_{tot}. \tag{2.10}$$

Substituting Eqs. (2.9) and (2.10) into (2.8), and projecting the equation in the perpendicular direction, we obtain:

$$\frac{d\left(\gamma m\vec{v}_\perp\right)}{dt} = -\frac{e}{c}\left[\frac{\partial}{\partial t}\vec{A}_{tot} - \left(\vec{v}\times\vec{\nabla}\times\vec{A}_{tot}\right)_\perp\right]. \tag{2.11}$$

Executing the cross product and using that the total derivative is the sum of the partial derivatives, finally:

$$\vec{v}_\perp = -\frac{c}{\gamma}\vec{a}_{tot}, \tag{2.12}$$

where $\vec{a}_{tot}$ is the total adimensional vector potential amplitude and $\vec{v}_\perp$ is the perpendicular velocity.

The energy evolution for the electrons (γmc^2) is given by a power equation:

$$\frac{d\left(\gamma mc^2\right)}{dt} = e\vec{E}\cdot\vec{v}_{\perp}. \tag{2.13}$$

Considering that the electric field acting over the electrons is caused due the presence of the total vector potential amplitude ($\vec{E} = \partial_t \vec{A}_{tot}/c$), then:

$$\frac{d\gamma}{dt} = -\frac{\omega a_w}{2\gamma}\left[ae^{i\theta(z,t)} + a^* e^{-i\theta(z,t)}\right], \tag{2.14}$$

where $\theta(z,t) = (k_w + k)z - \omega t + \phi$, by definition, is the phase of the electron in the ponderomotive well (the ponderomotive well is formed by the superposition of the wiggler and radiation fields). Depending upon its phase, the electron can be accelerated or decelerated by the ponderomotive well which is spatially periodic (with $k_p = k_w + k$ and $\lambda_p = 2\pi/k_p$). The evolution of the phase of each electron is obtained through the time derivative of the phase definition:

$$\frac{d\theta}{dt} = \left(k_w + k\right)v_z - \omega. \tag{2.15}$$

When $d\theta/dt = 0$, the phase of the electron remains the same. It occurs because the electron velocity (v_z) is equal to the ponderomotive well velocity (v_p). This velocity is called resonant velocity and is described by the relation:

$$v_p = \frac{k}{k_w + k}c = \frac{k}{k_p}c. \tag{2.16}$$

To reach Eq. (2.16), it was made the assumption of a quasi-vacuum medium ($\omega \approx kc$).

Finally, to obtain a complete set of equations to define the electron dynamics, we have a relation that connects γ and v_z:

$$v_z\left(\gamma, a_{tot}\right) = c\sqrt{1 - \left(\frac{1 + \left|a_{tot}\right|^2}{\gamma^2}\right)}. \tag{2.17}$$

It is important to mention that in this regime the vector potential amplitude of the laser is maintai-

ned constant, but, in fact, it is not, because the electron can deliver (or receive) energy to (from) the radiation field.

The FEL Pendulum Equation

In the limit of a single electron, the electron interacts only with the wiggler and radiation fields (there is not interaction with another electrons). Near this limit, Free-Electron Lasers work in low gain regime.

In the low gain regime, the ponderomotive well tends to attract the electron to its bottom (for a more stable condition). It causes a force which can decelerate or accelerate the electron, according to the phase evolution Eq. (2.15). A picture of this mechanism can be seen in the Fig. 2.3.

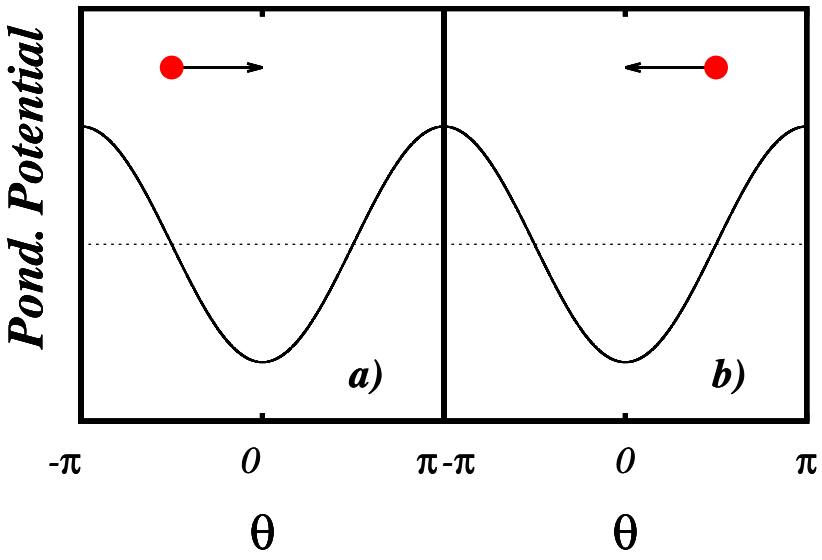

Fig. 2.3: In the vertical axis, the ponderomotive potential (that is sinusoidal) which can a) accelerate or b) decelerate the electron.

The decrease (increase) of the electron's kinetic energy, evidently, cause a gain (loss) in the radiation amplitude. But, in the case of the low gain regime, the changes in the radiation amplitude could be neglected. Thus, it allows us to consider that the laser amplitude is constant. Then, we rewrite Eq. (2.14):

$$\frac{d\gamma}{dt} = -\frac{\omega\, a_w\, a}{2\gamma}\sin\theta. \tag{2.18}$$

To find the famous FEL pendulum-like equation, we make use of the second time derivative of the phase definition:

$$\frac{d^2}{dt^2}\theta = (k_w + k)\,\frac{d}{dt}v_z. \tag{2.19}$$

The velocity modulus of the electron can be expressed by a sum of the longitudinal and transverse components of the electron's velocity ($v^2 = {v_z}^2 + \langle v_x\rangle^2$). Then, we have:

$$\langle v_x\rangle \cong -\frac{c}{\gamma}a_w\langle e^{-ik_w z}\rangle = -\frac{c}{2\gamma}a_w, \tag{2.20}$$

and, in the relativistic limit ($[1 + a_w^2/4]/\gamma^2 \ll 1$):

$$v_z = c\sqrt{1 - \frac{1 + {a_w}^2/4}{\gamma^2}} \cong c\left(1 - \frac{1 + {a_w}^2/4}{2\gamma^2}\right). \tag{2.21}$$

Applying the time derivative in the Eq. (2.21), it is possible to connect γ and v_z:

$$\frac{d}{dt}v_z = c\left(\frac{1 + {a_w}^2/4}{\gamma^3}\right)\frac{d}{dt}\gamma. \tag{2.22}$$

Substituting Eq. (2.22) and then Eq. (2.18) in Eq. (2.19), we finally find:

$$\frac{d^2}{dt^2}\theta = -\omega\, c\, a_w\, a\, k_p\left(\frac{1 + {a_w}^2/4}{\gamma^4}\right)\sin\theta. \tag{2.23}$$

Defining $\Omega^2 = \omega\, c\, a_w\, a\, k_p\,((1 + {a_w}^2/4)/\gamma^4)$, we can rewrite Eq. (2.23) in the traditional pendulum form:

$$\frac{d^2}{dt^2}\theta = -\Omega^2\sin\theta. \tag{2.24}$$

In this equation, Ω represents the oscillation frequency for small angles (when $\sin\theta \sim \theta$).

Basically, two equations (one for the phase and the other for the energy) are enough to understand the FEL dynamics in the low gain regime. To see the pendulum behavior in the phase-space ($\gamma \times \theta$), we integrate the equations over the time using computational methods. To simplify the equations, we make use of some normalizations: $v_z/c \to v_z$, $\omega t \to t$ and $t \to v_p z \approx z$. These normalizations allow us to rewrite the set of equations:

$$\frac{d}{dt}\gamma = -\frac{a_w\, a}{\gamma}\sin\theta. \tag{2.25}$$

$$\frac{d}{dt}\theta = \frac{v_z}{v_p} - 1. \tag{2.26}$$

$$v_z = \sqrt{1 - \frac{1 + |a_{tot}|^2}{\gamma^2}}. \tag{2.27}$$

The result of the integration for 15 different initial conditions is shown in Fig. 2.4 (setting $a_w = 0.4; a = a_w\, 10^{-5}; k_w = 0.01; k = 0.99$).

The closed trajectories in the phase-space (the red lines inside the separatrix) represent the electrons with energy comparable to the ponderomotive potential. Then, those electrons are trapped by the ponderomotive potential and they execute an oscillatory motion around a fixed point. The electrons which are trapped by the ponderomotive well effectively exchange energy with the laser field.

The open trajectories in the phase-space (the green lines outside the separatrix) represent the electrons with greater or smaller energies in comparison to the ponderomotive potential. In fact, the velocities difference between the ponderomotive potential and the electrons are so high that the electrons cannot be trapped by the wiggler and laser fields. Those electrons do not effectively exchange energy with the laser field.

The definition of the fixed point is the point where there is no resultant force over the electrons and it represents a stable condition (the trajectory in the phase-space, in this case, is a single point). The

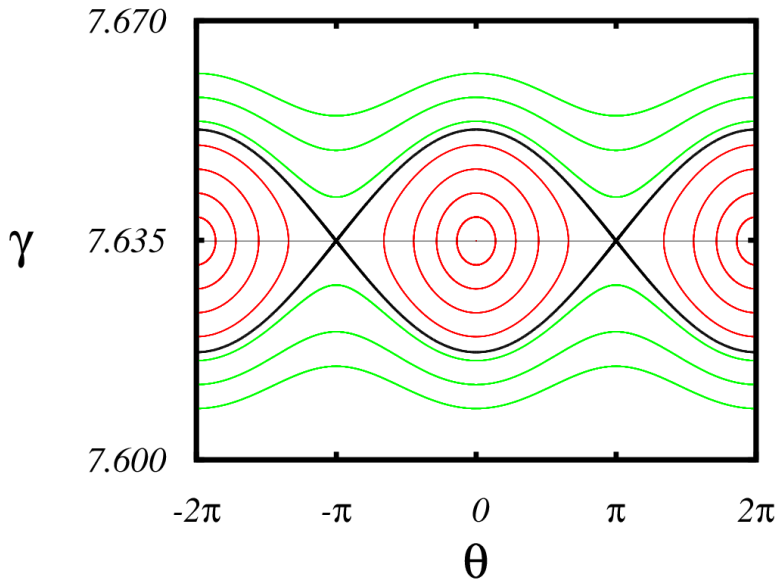

Fig. 2.4: The phase-space for some different initial conditions. The bottom of the ponderomotive well is located at $\theta = 2n\pi$, where $n = 0, \pm 1, \pm 2$. The ponderomotive well has 2π-periodicy. The red trajectories represent the trajectories made by trapped electrons. The black line is the separatrix between trapped and untrapped electrons. The green lines represent trajectories of electrons that are not trapped by the ponderomotive well. At last, the resonant energy is denoted by the grey line.

fixed point can be obtained when $d\gamma/dz = 0$ and $d\theta/dz = 0$. In according to Fig. 2.4, applying the proper conditions in Eqs. (2.25) and (2.26), the position of the fixed point is $\theta_{fp} = 0$ and the velocity is $v_{zfp} = v_p$. When the velocity of the electron is equal to the ponderomotive potential velocity, the corresponding energy is the resonant energy.

The ponderomotive potential can decelerate or accelerate the electrons. When it decelerates the electrons, the electrons deliver energy to the radiation field, increasing the laser amplitude, while when the electrons are accelerated, the electrons drain energy from the radiation field, decreasing the laser amplitude. It is interesting for a FEL to maximize the energy transfer from the electron beam to the laser field and it implies that we are pursuing to have the maximum number of decelerated electrons.

In a scenario where we need to have closed trajectories (because the electrons with closed trajectories effectively exchange energy with the laser field) and the maximum number of decelerated

electrons, some solutions can be suggested. If we consider a monoenergetic and resonant electron beam, on average half of the electrons will accelerate and half of them will be decelerated, with no net gain. One of the suggestions is to increase a little bit the injection energy, to be higher than the resonant energy, but with a superior limit (the limit is imposed by the sepatrix). In this situation, there will be a low net gain. Another suggestion is to use short-wigglers. Where short here is related to the time (or in terms of length, the time and velocity of the electrons) to complete a closed trajectory in the phase-space, near the fixed point (this time is related with the pendulum frequency, $T_{wiggler} < 2\pi/\Omega$, and the length of the wiggler must be $L_{wiggler} = v_p T_{wiggler} < 2\pi v_p/\Omega$)[11].

Although the low gain regime is quite intuitive, illustrative and pedagogical, it is not interesting from the point of view of the FEL operating capacity. To increase the gain and the laser maximum amplitude it is necessary to increase the current density in the system and this increase lead to collective behaviors that change the FEL dynamics significantly. With high current densities, the laser field cannot be considered constant anymore. For this reason, we must develop an evolution equation to describe the radiation field dynamics. Space-charge effects must be also included.

2.2.3 High Gain FELs

High gain FELs work with long wigglers and high current densities, thus self-interaction among the electrons must be considered[11]. The electrons self-bunch around a phase corresponding to gain on the scale of the radiation wavelength (it implies that energy modulation becomes space or phase modulation). The self-bunching is responsible to coherent radiation and exponentially growth of radiation. The saturation of the growing of the radiation field occurs when nonlinear effects become relevant to the system. The main nonlinear effect is, as we shall see, a wave-breaking-like phenomenon (that we call mixing). This phenomenon is associated to the spread of particles in the phase-space.

We can classify two different regimes for high gain FELs: Compton and Raman regimes. In Compton regime, the self-interaction of the electronic population is negligible. In the Raman regime,

the electronic density is sufficiently high that self-interaction is relevant. Raman regimes involve space-charge plasma waves, whose resulting forces acting on the electronic population are comparable to the forces produced by the ponderomotive potential well[11, 23, 24, 25].

Relaxation in FELs occurs through dynamical mixing. During the mixing process, the electrons, that are self-bunched, are so close that the electronic repulsion is big enough to cause a phase-space spread of the electrons. After the start of this phase-space spread the growth ceases. If the charge in the system is small, the ponderomotive well mainly drives the particle dynamics. In this case, the electronic distribution is attracted to the bottom of the ponderomotive well, revolving as a whole around itself in the particle phase-space.

As the charge increases, the electronic repulsion offers resistance against the ponderomotive well. In this case, not only the relaxation is delayed with respect to Compton approximations[26], but also the way the system relaxes reveals new features associated with the presence of density waves. The mixing process is very similar to the wave-breaking process in the case of magnetically focused charged beams[26, 27, 28].

The bunching action of the ponderomotive well plays an equivalent role to the focusing action of the guiding magnetic field, and in both cases space-charge effects oppose the focusing drive. We can summarize the high gain FEL dynamics in the Fig. 2.5.

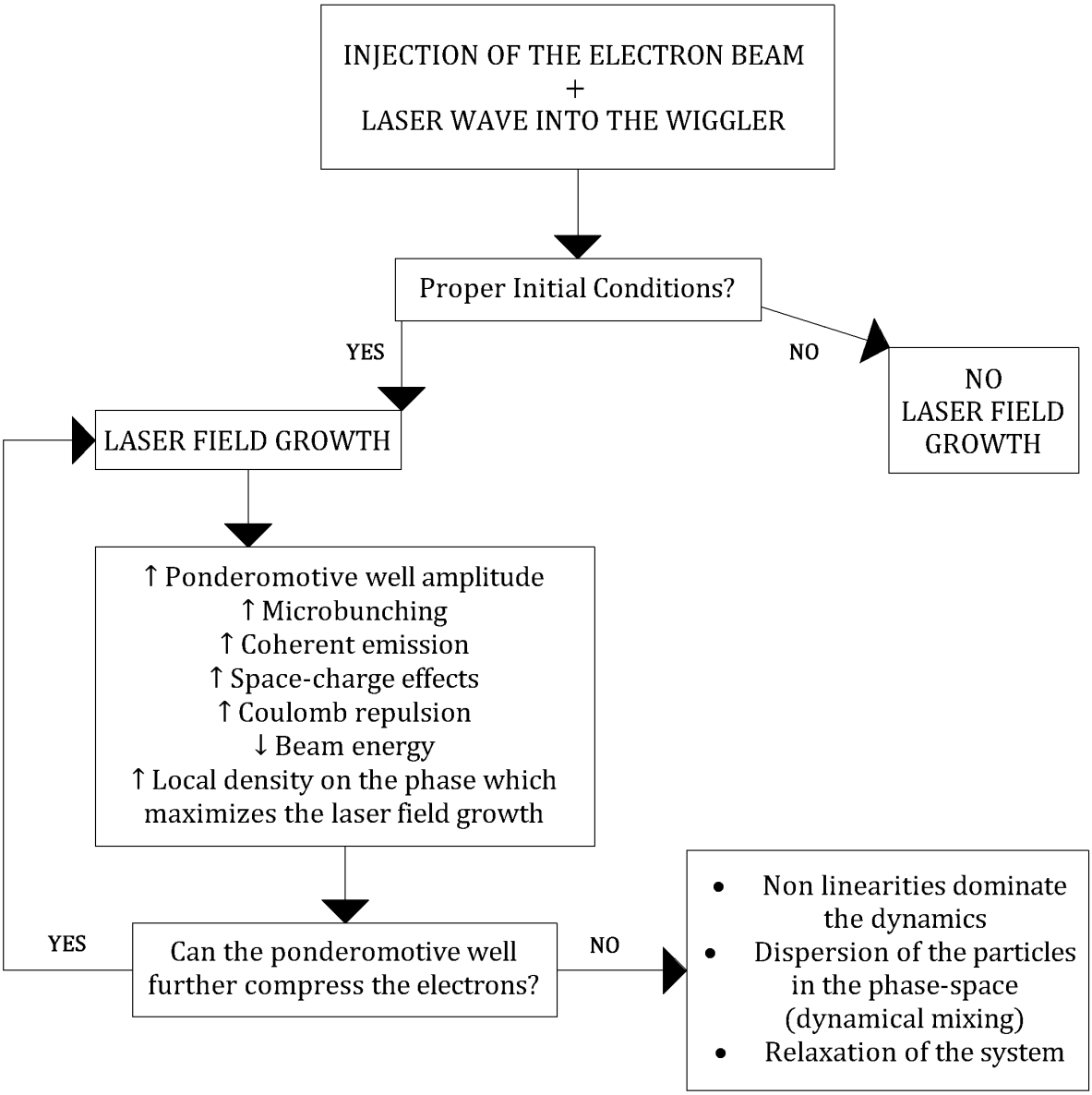

Fig. 2.5: Oversimplified flow chart of FEL operating in high gain regime.

Chapter 3

High Gain Regime: Particles and Laser Equations

The FEL dynamics in the high gain regime involves a description of the phase and energy evolution of each particle, as the space-charge effect and the laser field evolution. Thus, our goal in this chapter is to determine a self-consistent and complete set of equations that describe the FEL (the scheme is shown in Fig. 3.1).

We start considering, once again, an electron beam propagating in (the longitudinal) z-direction and a planar wiggler with a time independent and spatially periodic magnetic field, represented by:

$$\vec{A}_w(z) = \frac{mc^2}{e}\frac{a_w}{\sqrt{2}}\left(e^{-ik_w z} + e^{ik_w z}\right)\hat{x}, \tag{3.1}$$

While the radiation vector potential (with radiation frequency $\omega = kc = 2\pi c/\lambda$) would be described by (where $a(z,t)$ is a complex amplitude):

$$\vec{A}(z,t) = -i\,\frac{mc^2}{e}\frac{1}{\sqrt{2}}\left(ae^{i(kz-\omega t+\phi)} - a^* e^{-i(kz-\omega t+\phi)}\right)\hat{x}. \tag{3.2}$$

The electrons interact with the wiggler and laser fields and with themselves (space-charge). Then, it is possible to write:

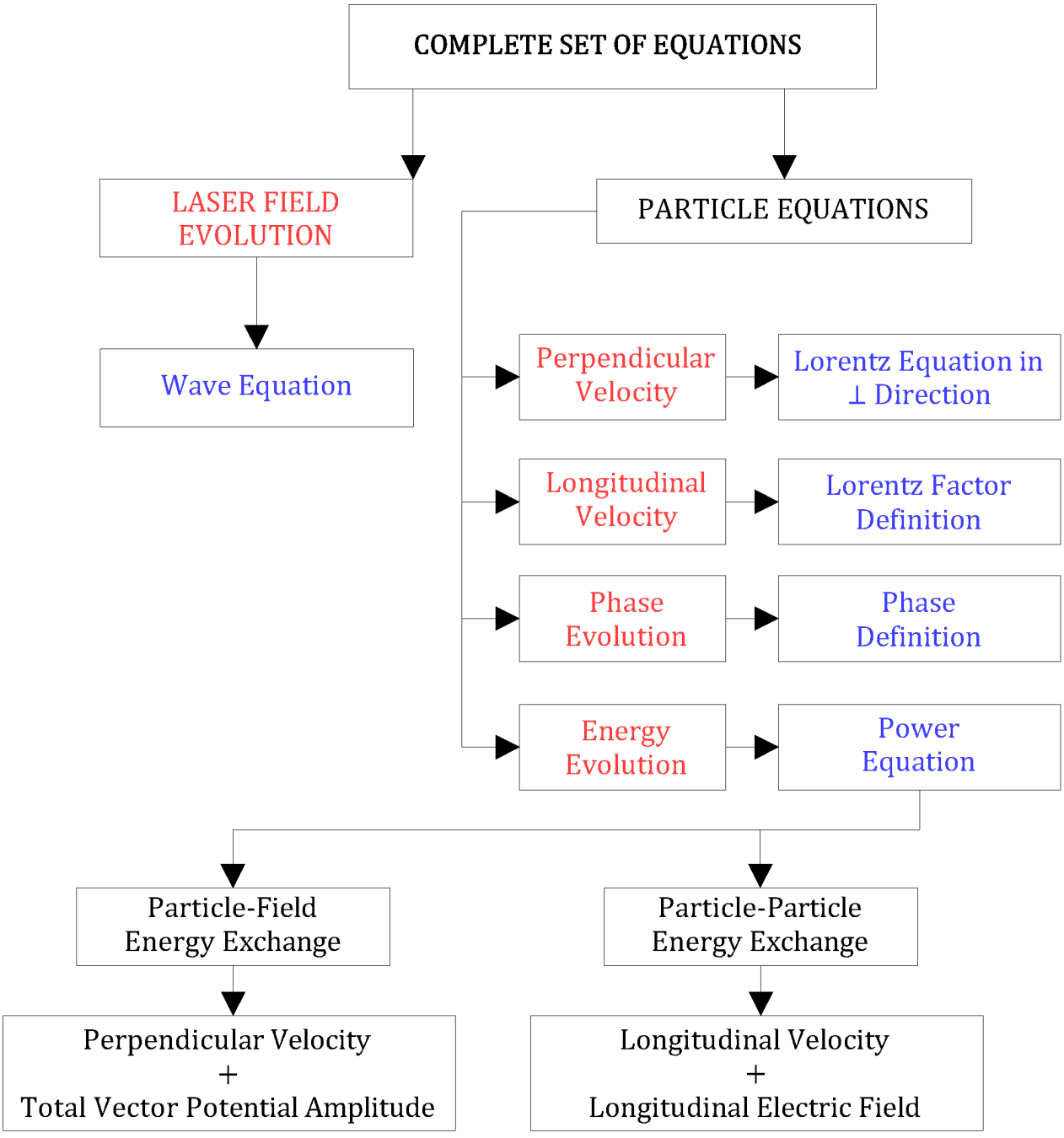

Fig. 3.1: Oversimplified flow chart of FEL equations. In red are the equations which form the complete set of equations. In blue the origin of the equations.

$$\vec{E} = -\frac{1}{c}\frac{\partial}{\partial t}\vec{A}_{tot}\left(z,t\right) - \nabla\Phi, \tag{3.3}$$

$$\vec{B} = \vec{\nabla} \times \vec{A}_{tot}\left(z,t\right). \tag{3.4}$$

In these equations, the total vector potential, $\vec{A}_{tot}$, is the vectorial sum of the radiation and wiggler vector potentials. The scalar potential (Φ) appears from the Coulombian interaction between the electrons (and we consider that this potential has only z dependence, i.e. the transverse space-charge effects are not considered). We may think that could be another electromagnetic field in order to confine the electron beam in the $y = 0$ plane.

3.1 Scalar Potential

The scalar potential over a particle represents the effect of all of the other particles over the first one. We assume that the amplitude of the vector potential of the laser is time independent (the dependence is only in space). Then, it can be considered a steady-state regime. In this work, as we saw in the last chapter, the ponderomotive potential is spatially periodic (with $\lambda_p = 2\pi/k_p$), and the dynamics is studied accompanying the advance of the a single 2π-in-phase interval of the ponderomotive potential through the space. To properly introduce the space-charge effects in the present FEL theory is necessary to have the same spatial periodicity between the ponderomotive potential and the space-charge.

Although a small portion of the electron beam is studied (we remember that we are accompanying only a single 2π-in-phase interval of the ponderomotive potential through the space), the number of the electrons in this region is huge. In order to reduce this number, our work is based on a sheet beam model[14]. Basically, the electrons give place to macro-particles grouped in sheets. The planar electric density is connected with the volumetric density through the number of sheets considered and the wavelength of the ponderomotive well. We emphasize that space-charge effects in the transverse directions are not considered.

Usually, the scalar potential produced by a sheet decays very slightly in space (and, for this reason this approach is unable when we must have the same spatial periodicity between the ponderomotive well and the electric field generated by a single sheet). To contour this problem, we introduce two grounded plates at y= $\pm L/2$. With the presence of these plates, field lines are captured by the plates. As a result, the scalar potential decays less slightly.

Assuming that the electrons are injected and remain confined in the $y = 0$ plane, the Poisson equation is written as:

$$\nabla^2 \Phi = -4\pi\delta(y)\rho, \tag{3.5}$$

where Φ is the scalar potential and ρ is the charge density.

Assuming that the solution for the scalar potential could be expressed by:

$$\Phi\left(y,z\right) = \sum_{n=1}^{\infty} \Phi_n\left(z\right) \cos\left(\frac{n\pi y}{L}\right), \tag{3.6}$$

and, representing the delta function in $y = 0$ as:

$$\delta\left(y\right) = \sum_{n=1}^{\infty} A_n \cos\left(\frac{n\pi y}{L}\right). \tag{3.7}$$

Substituting Eqs. (3.6) and (3.7) in the Poisson equation and making use of the orthogonality properties of the sine and cosine functions, it is possible to obtain an equation for each n-mode. The exact solution for Φ is given by the sum of the n-solutions of Φ_n of the n-equations:

$$\frac{\partial^2}{\partial z^2}\Phi_n\left(z\right) - \left(\frac{n\pi}{L}\right)^2 \Phi_n\left(z\right) = -4\pi\rho\left(z\right) A_n. \tag{3.8}$$

The solutions are $\propto e^{-n(z-z_0)/L}$ and, for this reason (because of the exponential decay which is higher for higher values of n), is acceptable to consider $n = 1$, in a way that $\Phi \sim \Phi_1$. Therefore, the

approximated equation for the scalar potential produced by a macro particle (sheet) is:

$$\frac{\partial^2}{\partial z^2}\Phi_1(z) - \left(\frac{\pi}{L}\right)^2 \Phi_1(z) = -4\pi\sigma(z - z_0)A_1, \tag{3.9}$$

where $A_n = (2/L)\int_{-L/2}^{-L/2} \delta(y)\cos\left[\left(\frac{2n-1}{L}\right)\pi y\right]dy$ and σ is the planar density of charge of the sheet.

This equation produces a family of solutions described by the Eq. (3.10):

$$\Phi_1 = C_1 e^{\frac{\pi z}{L}} + C_2 e^{\frac{-\pi z}{L}} + 2Le^{\frac{\pi(z-z_0)}{L}}\left(-1 + e^{\frac{-2\pi(z-z_0)}{L}}\right)(-1 + \Theta(z - z_0)), \tag{3.10}$$

C_1 and C_2 are constants which depend on the initial conditions of the problem. The function $\Theta(z-z_0)$ is the so called Heaviside function and z_0 is the position of the particle.

As mentioned earlier, it is necessary that the electric field (and the scalar potential) produced by a sheet and the ponderomotive potential have the same wavelength. For the equations, it means that:

$$\Phi_1\left(-\frac{\pi}{(k+k_w)}\right) = \Phi_1\left(\frac{\pi}{(k+k_w)}\right), \tag{3.11}$$

$$-\frac{\partial}{\partial z}\Phi_1\Big|_{z=-\frac{\pi}{(k+k_w)}} = -\frac{\partial}{\partial z}\Phi_1\Big|_{z=\frac{\pi}{(k+k_w)}}. \tag{3.12}$$

The analytical solution for Eq. (3.10) applying the conditions of Eqs. (3.11) and (3.12) is very complicated. From the graphical representation of the numerical solution, we propose to build an alternative function that is similar to the analytical solution. The chosen alternative function is a saw-tooth function (this function matches perfectly with the analytical solution in the limit where we are interested, i.e. $L \to \infty$). The graphical solution for the Eq. (3.10) with the conditions imposed by Eqs. (3.11) and (3.12), in terms of the electric field, is shown in Fig. 3.2, considering that the sheet is located in $z_0 = 0$.

In the Fig. 3.2 are shown graphical solutions for the Eq. (3.10). It is important to notice that the electric field is 2π-in-phase periodic and as the value of the distance L between the plates increases, the shape of the function for the electric field generated by a single sheet becomes more similar to a

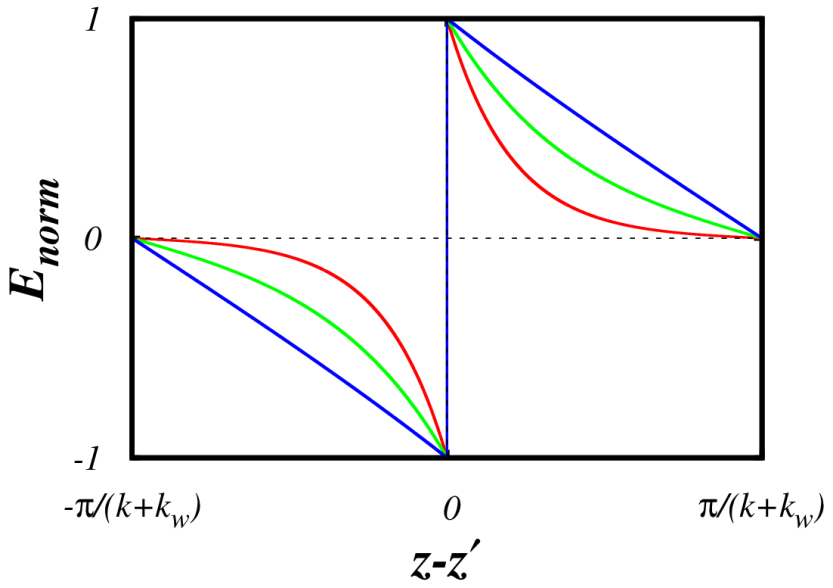

Fig. 3.2: Graphic representation of the solution for the electric field of the Eq. (3.10) for a sheet located in $z_0 = z'$. The solution is shown for three different values of the distance L ($= 2a.u.$, red curve; $= 4a.u.$, green curve; and, $= 16a.u.$, blue curve).

saw-tooth function.

The size of the step of the alternative function must be the same as the analytical solution. Keeping this condition, the alternative function for the electric field is written as:

$$E_z(z) = -2\sigma(k + k_w)(z - z_0) + 2\sigma\pi\frac{(z - z_0)}{|z - z_0|}. \tag{3.13}$$

The entire system is composed by N sheets. Thus, the electric field over the i-th particle (located in z_i) is given by (through the principle of superposition of the electric field):

$$E_{zi} = \sum_{j=1}^{N}\left[-2\sigma(k + k_w)(z_j - z_i) + 2\sigma\pi\frac{(z_j - z_i)}{|z_j - z_i|}\right]. \tag{3.14}$$

Executing a variable transformation in Eq. (3.14) (where $\theta = (k + k_w)z - kc$):

$$E_{zi} = 4\pi\sigma \sum_{j=1}^{N} \left[-\frac{(\theta_j - \theta_i)}{2\pi} + \frac{(\theta_j - \theta_i)}{2\,|\theta_j - \theta_i|} \right]. \tag{3.15}$$

The planar density σ is related with the volumetric density, through the wavelength and also through the number of sheets in this wavelength. Then, we obtain:

$$\sigma = e n_0 \frac{\lambda_p}{N}, \tag{3.16}$$

where n_0 is the volumetric density of electrons in the equilibrium and λ_p ($= 2\pi/(k_w + k)$) is the ponderomotive wavelength. It allows us to write the electric field and the scalar potential, respectively, as:

$$E_{zi} = 4\pi n_0 e \frac{1}{k_p N} \sum_{j=1}^{N} \left[-(\theta_j - \theta_i) + \pi \frac{(\theta_j - \theta_i)}{|\theta_j - \theta_i|} \right], \tag{3.17}$$

$$\Phi_i = 4\pi n_0 e \frac{1}{k_p N} \sum_{j=1}^{N} \left[\frac{(\theta_j - \theta_i)^2}{2} - \pi |\theta_j - \theta_i| \right]. \tag{3.18}$$

These are the final expressions to describe the electric field and the scalar potential due to the space-charge effect over a single sheet.

3.2 Perpendicular Momentum

The charged particles must respect Lorentz equation and have their momentum changed according:

$$\frac{d}{dt}\left(\gamma_i m \vec{v}_i\right) = e\vec{E}_i + e\frac{\vec{v}}{c} \times \vec{B}. \tag{3.19}$$

Projecting Eq. (3.19) in the x-direction, the space-charge is not considered. Thus:

$$\frac{d}{dt}\left(\gamma_i v_{xi}\right) = -\frac{e}{mc}\left[\frac{\partial}{\partial t} A_{tot} - \left(\vec{v} \times \vec{\nabla} \times \vec{A}_{tot} \right)_x \right]. \tag{3.20}$$

And finally (using the adimensional vector potential amplitude definition):

$$\frac{d}{dt}\left(\gamma_i v_{xi}\right) = -c\left[\left(\frac{\partial}{\partial t} + \frac{\partial z}{\partial t}\frac{\partial}{\partial z}\right) a_{tot}\left(z_i, t\right)\right]. \tag{3.21}$$

The total vector potential amplitude depends only on the time and z. So, the sum of the partial derivatives is the total derivative in time $(\partial/\partial t + (\partial z/\partial t)\,\partial/\partial z = d/dt)$. Therefore:

$$v_{xi} = -\frac{c}{\gamma_i} a_{tot}\left(z_i, t\right). \tag{3.22}$$

This relation shows the particles are deflected by the wiggler and laser fields in the x-direction and the modulus of the transverse velocity is proportional to the total vector potential amplitude and inverse in relation to the energy of the particle.

3.3 Energy Evolution

The interaction between the particle and the wiggler and radiation fields causes a deflection in the x-direction over the particles. This transversal component of the particle's velocity coupled with the vector potentials is responsible to a fraction of the energy exchange between the particles and the laser field. The other fraction is due the interaction between the particles and the longitudinal velocity.

The energy (γmc^2) evolution is given by a power equation:

$$\frac{d}{dt}\left(\gamma_i mc^2\right) = e\vec{E}_i \cdot \vec{v}_i. \tag{3.23}$$

This relation can be rewritten, resulting in:

$$\frac{d}{dt}\left(\gamma_i mc^2\right) = eE_{zi}v_{zi} - \left[\frac{e}{c}\frac{\partial}{\partial t}\vec{A}_{tot}\right] \cdot \vec{v}_i, \tag{3.24}$$

where E_{zi} is the electric field over the i-particle due the presence of the other particles.

Eq. (3.24) has two parts: the first term of the right hand side is a particle-particle mechanism of energy exchange; the second one is a particle-fields mechanism of energy exchange (and this one is responsible, effectively, to amplify the laser amplitude). In the next two subsections we discuss about these mechanisms.

3.3.1 Particle-Fields Energy Exchange

The second term of the right hand side of Eq. (3.24) is written as:

$$\left(\frac{d\gamma_i}{dt}\right)_{pf} = \frac{1}{2\gamma_i}\frac{\partial}{\partial t}\left|\vec{a}_{tot}\left(z_i,t\right)\right|^2, \tag{3.25}$$

where $\left|\vec{a}_{tot}\left(z_i,t\right)\right|^2$ is:

$$\left|\vec{a}_{tot}\left(z_i,t\right)\right|^2 = {a_w}^2 + \left|a\right|^2 - i\,a_w\,a\,e^{i\theta} + i\,a_w\,a^*\,e^{-i\theta}. \tag{3.26}$$

The non-resonant terms are not considered because they have a much faster dynamics which is not relevant for the system analysis. The variable $\theta(z_i,t)$ is the particle phase inside the ponderomotive potential. It is defined as:

$$\theta\left(z,t\right) = \left(k_w + k\right)z - \omega t + \phi. \tag{3.27}$$

Although an explicit form for the ponderomotive potential is not shown in this work, the ponderomotive potential is a result of the superposition of the wiggler and laser fields; certainly, it depends on the amplitude of these fields; and, furthermore, it is spatially periodic, with $k_p = k_w + k$ and $\lambda_p = 2\pi/k_p$.

We consider, in this work, that the beam is long enough that FEL works in a steady-state regime. Thus, **the amplitude of the potential vector of the laser is time independent** $(\partial/\partial t)a(z,t) = 0 \rightarrow$

$a(z,t) = a(z)$. With this condition, we have:

$$\left(\frac{d\gamma_i}{dt}\right)_{pf} = -\frac{\omega a_w}{2\gamma_i}\left[a(z)e^{i\theta_i} + a(z)^* e^{-i\theta_i}\right]. \tag{3.28}$$

This is the final expression for the particle-fields energy exchange mechanism.

3.3.2 Particle-Particle Energy Exchange

The longitudinal component of the electric field produced by the scalar potential is the space-charge effects and due the longitudinal velocity of the particles, there is energy exchange between the particles. The electric field over an i-particle can be expressed as:

$$E_{zi} = 4\pi n_0 e \frac{1}{k_p N}\sum_{j=1}^{N}\left[-(\theta_j - \theta_i) + \pi\frac{(\theta_j - \theta_i)}{|\theta_j - \theta_i|}\right]. \tag{3.29}$$

Thus, the last term of the right hand side of Eq. (3.24) is written as:

$$\left(\frac{d\gamma_i}{dt}\right)_{pp} = {\omega_p}^2 \frac{v_{zi}}{c^2}\frac{1}{k_p N}\sum_{j=1}^{N}\left[-(\theta_j - \theta_i) + \pi\frac{(\theta_j - \theta_i)}{|\theta_j - \theta_i|}\right], \tag{3.30}$$

where ${\omega_p}^2 = (4\pi n_0 e^2/m)$ is the square of the system's plasma frequency.

3.3.3 Total Energy Exchange

The total energy exchange is the sum of the particle-particle and particle-fields exchange and it is given by:

$$\frac{d\gamma_i}{dt} = \left(\frac{d\gamma_i}{dt}\right)_{pp} + \left(\frac{d\gamma_i}{dt}\right)_{pf}. \tag{3.31}$$

Then:

$$\frac{d\gamma_i}{dt} = {\omega_p}^2 \frac{v_{zi}}{c^2} \frac{1}{k_p N} \sum_{j=1}^{N} \left[-(\theta_j - \theta_i) + \pi \frac{(\theta_j - \theta_i)}{|\theta_j - \theta_i|} \right] - \frac{\omega a_w}{2\gamma_i} \left[a(z) e^{i\theta_i} + a(z)^* e^{-i\theta_i} \right]. \tag{3.32}$$

Eq. (3.32) is the energy evolution equation for each particle.

3.4 Phase Evolution

The phase of each sheet was defined in Eq. (3.27). To obtain a closed set of differential equations to describe the FEL dynamics we simply derived the phase equation in relation to time, obtaining:

$$\frac{d}{dt}\theta\left(z,t\right) = \left(k_w + k\right) v_{zi} - \omega. \tag{3.33}$$

A particle satisfies the resonance condition if $d\theta/dt = 0$. When this condition is satisfied the longitudinal velocity of the particle is equal to the phase velocity of the ponderomotive well (v_p). Thus:

$$v_{zi} = v_p = \frac{k\,c}{(k_w + k)}. \tag{3.34}$$

As a consequence of the resonant velocity, another resonant quantity is defined: the energy. The particle energy is called resonant when, according to Ref.[11], the relative phase between the transverse oscillations of the particles and the radiation remains constant. The resonant energy is obtained through Lorentz factor definition:

$$\frac{1}{\gamma^2} = 1 - {\beta_\perp}^2 - {\beta_\parallel}^2, \tag{3.35}$$

where $\beta = v/c$, $\beta_\perp$ and $\beta_\parallel$ are the perpendicular and longitudinal light-speed-normalized velocities.

Substituting Eq. (3.22) and Eq. (3.34) in Eq. (3.35):

$$\gamma_{res} = \sqrt{\frac{1+\left|a_{tot}\right|^2}{1-\left(\frac{k}{k_w+k}\right)^2}}. \tag{3.36}$$

The longitudinal velocity of each particle could be evaluated with the help of Lorentz factor definition and is expressed by:

$$v_{zi}\left(\gamma, a_{toti}\right) = c\sqrt{1-\frac{1+\left|a_{tot}(z,t)\right|^2}{{\gamma_i}^2}}. \tag{3.37}$$

The longitudinal velocity of the particle depends on the Lorentz factor (i.e. the energy of the particle) and on the total potential vector amplitude over the particle.

3.5 Laser Evolution

The last quantity that must be evaluated along the time is the vector potential of the radiation. The evolution of the laser field is obtained through the Ampère law, where:

$$\vec{\nabla}\times\vec{B} = \frac{4\pi}{c}\vec{J} + \frac{1}{c}\frac{\partial}{\partial t}\vec{E}. \tag{3.38}$$

Eq. (3.38) is rewritten as:

$$\vec{\nabla}\times\left(\vec{\nabla}\times\vec{A}\right) = \frac{4\pi}{c}\vec{J} + \left[-\frac{1}{c^2}\frac{\partial^2}{\partial t^2}\vec{A} - \frac{1}{c}\frac{\partial}{\partial t}\nabla\Phi\right]. \tag{3.39}$$

Using the Coulomb gauge ($\nabla\left[\nabla\cdot\vec{A}\right]=0$) and projecting Eq. 3.39 in the x-direction:

$$\left(\frac{\partial^2}{\partial z^2} - \frac{1}{c^2}\frac{\partial^2}{\partial t^2}\right)A = -\frac{4\pi}{c}J_\perp\left(z,t\right), \tag{3.40}$$

where $J_\perp\left(=e\sum_{j=1}^{N}\vec{v}_{\perp j}\delta(\vec{x}-\vec{x}_j(t))\right)$ is the transversal current density.

Once again, in this work, we consider that the FEL works in the steady-state regime, so, the amplitude of the vector potential of the laser is **time independent** $[A(z,t) = A(z)]$. Furthermore, the Slow Varying Envelope Approximation (SVEA) is adopted. In this approximation, the amplitude of the vector potential of the laser slowly varies in the space $((\partial^2/\partial z^2)A(z) \sim 0)$. Using these considerations, we work out Eq. (3.40), resulting in:

$$\frac{\partial}{\partial z}a(z) = \frac{4\pi e^2}{mc^2}\frac{1}{2k}\frac{N}{\alpha\lambda_p}\sum_{j=1}^{N}\frac{1}{\gamma_j}\left[a_w e^{-i\theta_j} - ia(z)\right]. \tag{3.41}$$

Defining $\sum_{j=1}^{N} f(\theta_j,\gamma_j)$ as:

$$\sum_{j=1}^{N} f(\theta_j,\gamma_j) = N\langle f\,(\theta,\gamma)\rangle, \tag{3.42}$$

where $f(\theta_j,\gamma_j)$ is a generic function that depends on θ_j and γ_j. While $\langle f(\theta,\gamma)\rangle$ is the mean value of this function.

Through this definition, the Eq. (3.41) can be expressed as:

$$\frac{d}{dz}a(z) = \left(\frac{\omega_p}{\omega}\right)^2\frac{k}{2}\left[a_w\left\langle\frac{e^{-i\theta}}{\gamma}\right\rangle - i\,a(z)\left\langle\frac{1}{\gamma}\right\rangle\right]. \tag{3.43}$$

The partial derivative in Eq. (3.41) gives place to a total z-derivative because the amplitude of the laser depends only on z. In Eq. (3.43) we have the plasma frequency ω_p $(=\sqrt{4\pi e^2 n_0/m})$ of the system.

Since we are accompanying the evolution of a 2π-in-phase window along the longitudinal direction, time and space are connected in a way that:

$$\frac{d}{dz}a(z) = \frac{dt}{d\langle z\rangle}\frac{d}{dt}a(z) = \frac{1}{v_z}\frac{d}{dt}a(z). \tag{3.44}$$

The time derivative of the amplitude must be understood as the time of propagation of an element of the electron beam (the 2π-in-phase window).

Defining a new parameter η ($= \omega_p/\omega$), where this parameter represents the charge in the system, the Eq. (3.43) is rewritten as:

$$\frac{d}{dz}a(z) = \langle v_z \rangle \, \eta^2 \, \frac{k}{2} \left[a_w \left\langle \frac{e^{-i\theta}}{\gamma} \right\rangle - i \, a(z) \left\langle \frac{1}{\gamma} \right\rangle \right]. \tag{3.45}$$

With Eq. (3.45) the set of equations to describe the FEL dynamics is complete.

3.6 Detuning

Although the complete set of equations is obtained, the situation in which the particles velocity is equal to the ponderomotive field velocity is not ideal when we are trying to reach the maximum growth rate for the stimulated radiation[11, 16, 17]. Therefore, a new parameter (the detuning) is introduced to deal with this problem.

Detuning is a parameter that measures somehow the difference in terms of velocity between the ponderomotive well and the electrons. There is two different ways to consider the detuning: the electrons are not injected with the resonant velocity; or, the velocity of the ponderomotive well is changed by modifying the radiation wavelength. It is important to mention that the velocities difference is very small. In the laboratories, there is a huge control over the energy of the electron beam. In this work, we choose to introduce the detuning through a change in the radiation wavelength. Thus, we define the detuning ν as:

$$\nu = \frac{v_p - v_p{}'}{v_p}, \tag{3.46}$$

where v_p is the velocity of injection of the particles and $v_p{}'$ is the ponderomotive well velocity (that depends on the radiation wavelength).

The relation between the wave numbers of the modified wave k' and the original one k is done

by:

$$k^{'} = \frac{k k_w}{k_p} \left(\frac{1-\nu}{\frac{k_w}{k_p} + \frac{k\nu}{k_p}} \right). \tag{3.47}$$

This change in the ponderomotive velocity introduces a change in the phase equation (Eq. (3.33)):

$$\frac{d}{dt}\theta = \left(\frac{k_w + k}{1-\nu} \right) v_z - \omega. \tag{3.48}$$

The inclusion of the detuning closes the theoretical grounding of the FEL studied in this work. In the next section we present the normalization for the complete set of equations.

3.7 Normalization and Complete Set of Equations

In this chapter we presented equations to describe: the longitudinal velocity of the particles (Eq. (3.37)); the square of the modulus of the total vector potential (Eq. (3.26)); the energy evolution of each particle (Eq. (3.32)); the phase of the particles (Eq. (3.48)); and, finally, the laser evolution (Eq. (3.45)). These equation forms a complete and auto-consistent set of equations.

We normalize the velocities by the speed of light ($v/c \rightarrow v$), the time is normalized by the radiation frequency ($\omega t \rightarrow t$) and, at least, time becomes space ($v_p t \rightarrow z$).

With these normalizations, the complete set of equations is expressed by:

$$v_{zi}\left(\gamma, a_{toti}\right) = \sqrt{1 - \frac{1 + \left|a_{tot}(z,t)\right|^2}{{\gamma_i}^2}}, \tag{3.49}$$

$$\left|\vec{a}_{tot}\left(z_i, t\right)\right|^2 = {a_w}^2 + \left|a\right|^2 - i\, a_w\, a\, e^{i\theta} + i\, a_w\, a^*\, e^{-i\theta}, \tag{3.50}$$

$$\frac{d\gamma_i}{dz} = v_{zi} v_p \frac{\eta^2}{N} \sum_{j=1}^{N} \left[-(\theta_j - \theta_i) + \pi \frac{(\theta_j - \theta_i)}{|\theta_j - \theta_i|} \right] - \frac{a_w}{2\gamma_i} \left[a(z) e^{i\theta_i} + c.c. \right], \tag{3.51}$$

$$\frac{d}{dz}\theta_i = \frac{v_{zi}}{v_p^{'}} - 1, \tag{3.52}$$

$$\frac{d}{dz}a(z) = \eta^2\, v_p \left[a_w \left\langle \frac{e^{-i\theta}}{2\gamma} \right\rangle - i\, a(z) \left\langle \frac{1}{2\gamma} \right\rangle \right]. \tag{3.53}$$

This set of equations is used on the following chapters in the particles-wave simulations. The differences between the cases (cold and warm beams) are introduced in the initial conditions of the problem.

Chapter 4

Cold Beam Case

In this chapter we present a low dimensional semi-analytical model based on the compressibility factor to perform analytical estimates of the elapsed time until the onset of mixing and of the saturated amplitude of the radiation field. This model is useful, also, to pinpoint space-charge effects and the corresponding transition from Compton to Raman regimes.

The model consists in: a linear analysis to establish the linear wave dynamics; and, the nonlinear particle dynamics, which introduces the nonlinearities of the problem.

Before the start of the development of the model, we consider that the stimulated radiation is amplified from small values, and that at $z = 0$, particles are distributed uniformly over the phase θ, traveling along the z-axis with velocity $v_{z_{injection}} = v_p$ (the initial distribution is shown in Fig. 4.1). The value of the injection velocity, v_p (which in the case of a cold beam is equal for all of the electrons), is not necessarily equal to the ponderomotive wave phase velocity $v_p{}'$. The reason for that is the consideration of the detuning. This parameter shall always be chosen to optimize the FEL interaction, maximizing the growth rate of the stimulated radiation.

During the dynamics, particles are subjected to the combined action of the ponderomotive and space-charge forces. The relative magnitude between these two forces plays a crucial role in the operation of the FEL (in Compton regime, space-charge force is smaller than the ponderomotive one; while in Raman regime, space-charge force is comparable to the ponderomotive one). In any case,

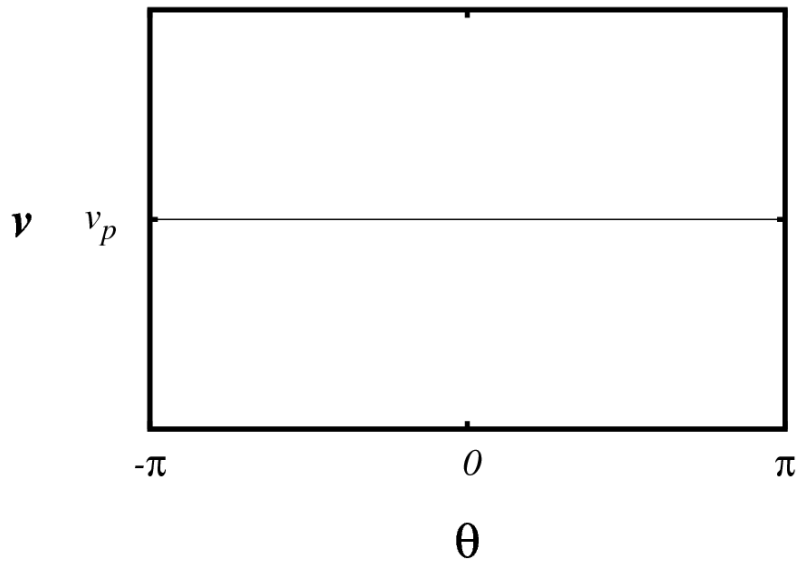

Fig. 4.1: Initial distribution of the electron beam: a monoenergetic and spatially-uniform distribution.

as time evolves, the particle beam undergoes phase-mixing in the phase-space and the whole process reaches saturation afterwards. The **onset of the mixing** process in the phase-space occurs when the distribution of the particles is not a single valuated function anymore[11].

4.1 Linear Analysis

The electron beam is injected with a copropagating radiation field, in a way that the initial amplitude of the laser field is very small in comparison with the wiggler field. Then, the radiation field is considered a perturbation of the vector potential of the wiggler. The radiation and the wiggler fields cause perturbations in the other physical quantities (phase and energy) around the equilibrium values (the equilibrium values are obtained from the zero-order solutions of the equations). In this section, we present a linear analysis based in those perturbations, which implies in a linearization of the complete set of equations from the last chapter. Instead of using the original physical quantities, we made use of the collective variables. The collective variables represent somehow the fluctuations in the va-

lues of the physical quantities. Through this analysis is possible to determine the linear growth rate of the laser field, the instability region (where occurs the laser growing) and the parameters to maximize the growth rate.

To the good working of the linear analysis, it is necessary that the system starts from an equilibrium situation (it means that the initial phase variation must be equal to zero). Then, the interactions among the particles and with the laser and wiggler fields develop perturbations, which can amplify the radiation field and culminate in the phase-space mixing, with velocities/energy spread.

From Eq. (3.52), if the detuning is different from zero, there is an initial variation in the phase. To solve this problem, a new phase variable, $\tilde{\theta}$, is proposed:

$$\theta = \tilde{\theta} + F(\nu)z. \tag{4.1}$$

Imposing that the initial variation of the new phase variable must be zero $\left(d\tilde{\theta}/dz|_{z=0} = 0\right)$, $F(\nu)$ is written as:

$$F(\nu) = \frac{1}{1-\nu} - 1. \tag{4.2}$$

Then, Eq. (3.52) is rewritten:

$$\frac{d}{dz}\tilde{\theta} = \frac{v_z}{v_p{}'} - 1 - F(\nu). \tag{4.3}$$

The change in the phase variable causes a change in the laser amplitude field. The new, $\tilde{a}$, and the old, a, fields are connected according to:

$$\tilde{a}e^{i\tilde{\theta}} = ae^{i\theta}. \tag{4.4}$$

These changes are necessary to properly obtain the laser field evolution in the linear regime.

4.1.1 Phase Equation

The initial vector potential amplitude of the radiation is small ($\tilde{a} \ll 1$) and the energy spread during the linear regime is also small ($\Delta\gamma \ll \gamma$). It allows us to approximate the longitudinal velocity, in a linear way, in the vicinities of $\tilde{a} = 0$ and $\gamma = \gamma_0$ (where γ_0 is the injection electron energy). Thus:

$$v_{zi} \cong v_p + \frac{\partial}{\partial \tilde{a}} v_{zi}\Big|_{injection} \tilde{a} + \frac{\partial}{\partial \gamma_i} v_{zi}\Big|_{injection} (\gamma_i - \gamma_0)\,. \tag{4.5}$$

Executing the expansion for the longitudinal velocity and keeping only the term in phase with $e^{i\tilde{\theta}}$ for $\tilde{a}$, we found:

$$v_{zi} \cong v_p + \frac{1}{2} \frac{i\, {a_w}\, \tilde{a}\, e^{i\tilde{\theta}_i}}{v_p {\gamma_0}^2} + \frac{1 + {a_w}^2}{v_p {\gamma_0}^3} (\gamma_i - \gamma_0)\,. \tag{4.6}$$

Substituting Eq. (4.6) in Eq. (4.3):

$$\frac{d}{dz}\tilde{\theta} = \frac{i}{2} \frac{{a_w}\, \tilde{a}\, e^{i\tilde{\theta}_i}}{v_p {v_p}' {\gamma_0}^2} + \frac{1 + {a_w}^2}{v_p {v_p}' {\gamma_0}^3} (\gamma_i - \gamma_0)\,. \tag{4.7}$$

At this point, the (complex) collective variables are defined in Eqs. (4.8) and (4.9):

$$X = \langle e^{-i\tilde{\theta}_0} \delta\tilde{\theta} \rangle, \tag{4.8}$$

$$Y = \langle e^{-i\tilde{\theta}_0} \delta\gamma \rangle. \tag{4.9}$$

The collective variable X represents somehow the fluctuations in the phase, while the collective variable Y represents somehow the fluctuations in the energy of the electrons.

Multiplying Eq. (4.7) by $e^{-i\tilde{\theta}_0}$, expanding the perturbed quantities (in a linear form $\xi = \xi_0 + \delta\xi$), taking the mean and keeping only the linear perturbative terms, it is found:

$$\dot{X} = i \left[\frac{{a_w}}{2 v_p {v_p}' {\gamma_0}^2} \right] \tilde{a} + \left[\frac{1 + {a_w}^2}{v_p {v_p}' {\gamma_0}^3} \right] Y. \tag{4.10}$$

Or, simply:

$$\dot{X} = cY + id\tilde{a}, \tag{4.11}$$

where:

$$c = \frac{1 + {a_w}^2}{v_p {v_p}' {\gamma_0}^3}, \tag{4.12}$$

$$d = \frac{a_w}{2v_p {v_p}' {\gamma_0}^2}. \tag{4.13}$$

Eq. (4.11) represents the evolution equation for the collective variable X, where X is a complex variable.

4.1.2 Laser Equation

Eq. (3.53) is transformed for the new variables, taking the form:

$$\frac{d}{dz}\tilde{a}(z)e^{-iF(\nu)z} = \eta^2 \, v_p \left[a_w \left\langle \frac{e^{-i\theta}}{2\gamma} \right\rangle - i \, \tilde{a}(z)e^{-iF(\nu)z} \left\langle \frac{1}{2\gamma} \right\rangle \right]. \tag{4.14}$$

In Eq. (4.14), the longitudinal velocity is kept in zero-order. The perturbation comes from the collective variables of the phase and energy, and, of course, from the radiation amplitude itself.

Executing the spatial derivative and multiplying the Eq. (4.14) by $e^{iF(\nu)z}$ it is found that:

$$\dot{\tilde{a}} - i \, F(\nu) \, \tilde{a} = - \left[v_p \frac{a_w \eta^2}{2\gamma_0} \right] \left(i \, X + \frac{Y}{\gamma_0} \right) - i \left(v_p \frac{\eta^2}{2\gamma_0} \right) \tilde{a}. \tag{4.15}$$

Or:

$$\dot{\tilde{a}} = -h \left(iX + \frac{Y}{\gamma_0} \right) - ig\tilde{a}, \tag{4.16}$$

where:

$$g = v_p \frac{\eta^2}{2\gamma_0} - F(\nu), \tag{4.17}$$

$$h = v_p \frac{\eta^2 a_w}{2\gamma_0}. \tag{4.18}$$

Eq. (4.16) is the evolution equation for the laser amplitude in the linear regime.

4.1.3 Energy Equation

The last equation that must be analyzed to establish a complete set of linear equations is the energy equation. For the energy equation, we made use of the Fourier transformation of the space-charge term, considering only the first harmonic. Thus, Eq. (3.51) is rewritten as:

$$\frac{d\gamma_i}{dz} = v_{zi} v_p \frac{\eta^2}{N} \sum_{j=1}^{N} \left[-ie^{i(\tilde{\theta}_j - \tilde{\theta}_i)} + c.c. \right] - \frac{a_w}{2\gamma_i} \left[\tilde{a} e^{i\tilde{\theta}_i} + c.c. \right]. \tag{4.19}$$

Multiplying Eq. (4.19) by $e^{-i\tilde{\theta}_0}$, expanding the perturbed quantities, taking the mean and considering only the perturbative terms in phase, we obtain:

$$\dot{Y} = -\frac{a_w}{2\gamma_0}\tilde{a} - {v_p}^2 \eta^2 X. \tag{4.20}$$

Or, simply:

$$\dot{Y} = -f\tilde{a} - eX, \tag{4.21}$$

where:

$$e = {v_p}^2 \eta^2, \tag{4.22}$$

$$f = \frac{a_w}{2\gamma_0}. \tag{4.23}$$

Eq. (4.21) evaluates the evolution of the fluctuations in the energy of the electrons.

4.1.4 Dispersion Relation

At this moment, the set of linear equations is complete. Thus, we are interested to find a dispersion relation that could provide information about the linear growth of the laser field.

All of the linear equations depend on the three collective variables (Y,X and $\tilde{a}$). It is possible to combine the linear equations in a way that we obtain a cubic dispersion relation[11, 16].

Applying the third derivative in Eq. (4.16):

$$\dddot{\tilde{a}} = -h\left(i\ddot{X} + \frac{\ddot{Y}}{\gamma_0}\right) - ig\ddot{\tilde{a}}. \tag{4.24}$$

Substituting in Eq. (4.24) the derivative of Eqs. (4.11) and (4.25) and then Eqs. (4.11), (4.16) and (4.21):

$$\dddot{\tilde{a}} + ig\ddot{\tilde{a}} - \left(hd + \frac{hf}{\gamma_0} - ce\right)\dot{\tilde{a}} - i\left(cfh + \frac{deh}{\gamma_0} - ceg\right)\tilde{a} = 0. \tag{4.25}$$

Eq. (4.25) depends only on the laser amplitude. In the linear regime, the laser field grows exponentially, that is $\tilde{a} \propto e^{i\lambda z}$. Then, substituting this *ansatz* in Eq. (4.25):

$$\lambda^3 + g\lambda^2 + \left(hd + \frac{hf}{\gamma_0} - ce\right)\lambda + \left(cfh + \frac{deh}{\gamma_0} - ceg\right) = 0. \tag{4.26}$$

Eq. (4.26) is a cubic polynomial equation for λ. There are three possible solutions for a cubic polynomial equation: $1-$ three distinct real roots; $2-$ multiple roots and all its roots are real; $3-$ one real root and two complex conjugate roots.

According to the *ansatz*, the laser field grows if λ has an imaginary part. This is the case where the solution is composed by one real root and two complex conjugate roots. The roots of the cubic polynomial equation could be found analytically with Cardano's Method.

In the cold beam case, the parameters which led to instabilities (and laser field growing) in the particles-wave simulations are the same that led to a complex conjugate roots as solution of Eq. (4.26). This result is better discussed in the Section 4.3. It means that the linear analysis provides a good idea about the initial conditions required by the FEL to amplify the radiation field.

Moreover, in the stability situation (with no laser growth), the particles cannot get closer to each other due to the electric repulsion. Thus, each particle is confined between its neighbors during all the space and there is not significantly energy exchange between the particles and the radiation field. In this situation, the linear equations reproduce exactly the evolution of the laser amplitude obtained

through particles-wave simulations.

4.2 Semi-Analytical Model

In this section, a semi-analytical model is proposed. This semi-analytical model provides a way to calculate the time for the onset of mixing and subsequent relaxation and the saturated amplitude of the radiation field. The model, which is based on the compressibility factor, also helps to identify the presence of space-charge effects in Raman regimes, as the compressibility develops characteristic oscillations in this case.

Basically, in the model, the linear equations of the previous section are used to simulate the laser field growing. It is a good assumption, once the system is almost linear until the onset of mixing (as is seen in the particles-wave simulations). Moreover, nonlinearities caused due the space-charge effects are introduced through a connection between energy and phase equations and some considerations about the charge distribution.

4.2.1 Phase Equation

To build our semi-analytical model, we start with the phase equation; exploring its connection with the energy (the energy is present in the longitudinal velocity). Thus, the transformed phase equation (Eq. (4.3)) is rewritten:

$$\frac{d}{dz}\tilde{\theta} = \frac{v_z}{v_p{}'} - 1 - F(\nu). \tag{4.27}$$

Once again, the longitudinal velocity is expanded around the ponderomotive potential phase velocity:

$$v_z \cong v_z|_{injection} + \delta\left|\vec{\tilde{a}}_{tot}\right|^2 \left(\frac{\partial}{\partial\left|\vec{\tilde{a}}_{tot}\right|^2} v_z\right)\Bigg|_{injection} + \delta\gamma^2 \left(\frac{\partial}{\partial\gamma^2} v_z\right)\Bigg|_{injection}, \tag{4.28}$$

where the fluctuations are denoted by δ.

The velocity fluctuations depend strongly on the γ^2 fluctuations, in a way that $|\tilde{a}_{tot}|^2$ fluctuations can be neglected ($\delta\gamma^2 \gg \delta|\tilde{a}_{tot}|^2$). Therefore:

$$v_z \cong v_p + \delta\gamma^2 \left(\frac{\partial}{\partial\gamma^2} v_z\right)\Bigg|_{injection} = v_p + D_{\gamma^2}\delta\gamma^2, \tag{4.29}$$

where (keeping the fluctuations in first-order):

$$D_{\gamma^2} = \frac{1 + {a_w}^2}{2v_p{\gamma_0}^4}, \tag{4.30}$$

$$\delta\gamma^2 = 2\gamma_0\delta\gamma. \tag{4.31}$$

Substituting Eq. (4.29) in Eq. (4.27):

$$\frac{d}{dz}\tilde{\theta} = \left(\frac{1 + {a_w}^2}{v_p{v_p}'\gamma_0{}^3}\right)\delta\gamma. \tag{4.32}$$

In Eq. (4.32) the connection between the transformed phase $\tilde{\theta}$ and the energy fluctuations $\delta\gamma$ is quite clear.

4.2.2 Energy Fluctuation Equation

The transformed phase equation is related with the energy fluctuation. In this subsection we explore the other side: how the energy fluctuation evolution equation is connected with the transformed phase. The differential equation that describes the evolution of the energy fluctuation is obtained from a power equation and expanding the Lorentz factor in a linear way ($\gamma = \gamma_0 + \delta\gamma$). Then:

$$\frac{d}{dz}\left(\delta\gamma\right) = \frac{e}{kmc^3}\left[\delta\left(v_x E_x\right) + \delta\left(v_z E_z\right)\right]. \tag{4.33}$$

The $\delta\left(v_x E_x\right)$ is proportional to the energy variation due the coupling of the transversal velocity and the wiggler and laser fields; while the $\delta\left(v_z E_z\right)$ is proportional to the energy variation due the

coupling of the longitudinal velocity and the space-charge field.

Keeping the fluctuations in first-order, we obtain:

$$\frac{d}{dz}\left(\delta\gamma\right) = -\frac{a_w}{2\gamma_0}\left(\tilde{a}e^{i\tilde{\theta}} + c.c.\right) + \frac{e}{kmc^3}\left(v_p\, E_z\right). \tag{4.34}$$

In Eq. (4.34) all the terms are known, except the longitudinal electric field E_z. The longitudinal electric field is expressed as:

$$E_z(z) = \int G\left(z, z_0\right) n\left(z_0\right) dz_0, \tag{4.35}$$

where $G(z, z_0)$ is the dimensionless Green function for the electric field, which was somehow derived in the Chapter 3; and $n(z_0)$ is the volumetric density of particles.

The dimensionless Green function can be expressed as (with a variable transformation):

$$G\left(\tilde{\theta}, \tilde{\theta_0}\right) = \begin{cases} -2\pi - 2\left(\tilde{\theta} - \tilde{\theta}_0\right) & \text{if } \tilde{\theta} < \tilde{\theta}_0, \\ 2\pi - 2\left(\tilde{\theta} - \tilde{\theta}_0\right) & \text{if } \tilde{\theta} > \tilde{\theta}_0. \end{cases} \tag{4.36}$$

Substituting Eq. (4.36) in Eq. (4.35):

$$E_z(\tilde{\theta}) = \int_{-\pi}^{\tilde{\theta}} \left[2\pi - 2\left(\tilde{\theta} - \tilde{\theta}_0\right)\right] n(\tilde{\theta}_0) d\tilde{\theta}_0 + \int_{\tilde{\theta}}^{\pi} \left[-2\pi - 2\left(\tilde{\theta} - \tilde{\theta}_0\right)\right] n(\tilde{\theta}_0) d\tilde{\theta}_0. \tag{4.37}$$

Regrouping the terms:

$$E_z = -2\tilde{\theta}\int_{-\pi}^{\pi} n(\tilde{\theta}_0) d\tilde{\theta}_0 + 2\int_{-\pi}^{\pi} \tilde{\theta}_0 n(\tilde{\theta}_0) d\tilde{\theta}_0 - 2\pi\int_{\tilde{\theta}}^{\pi} n(\tilde{\theta}_0) d\tilde{\theta}_0 + 2\pi\int_{-\pi}^{\tilde{\theta}} n(\tilde{\theta}_0) d\tilde{\theta}_0. \tag{4.38}$$

Considering the presence of N sheets with planar density expressed by σ:

$$E_z(\tilde{\theta}) = -2\tilde{\theta}N\sigma + 2\langle\tilde{\theta}\rangle N\sigma - 2\pi\int_{\tilde{\theta}}^{\pi} n(\tilde{\theta}_0) d\tilde{\theta}_0 + 2\pi\int_{-\pi}^{\tilde{\theta}} n(\tilde{\theta}_0) d\tilde{\theta}_0. \tag{4.39}$$

The initial particles distribution is uniform in a way that the center of mass and the mean position

of the distribution are, approximately, null until the onset of mixing (i.e. $\langle\tilde{\theta}\rangle \cong 0$). Moreover, the number of particles to the left of $\tilde{\theta}_0$ is almost constant until the onset of mixing. These considerations allow us to write:

$$\begin{cases} \int_{\tilde{\theta}}^{\pi} n(\tilde{\theta}_0) d\tilde{\theta}_0 = N_+ \sigma, \\ \int_{-\pi}^{\tilde{\theta}} n(\tilde{\theta}_0) d\tilde{\theta}_0 = N_- \sigma, \end{cases} \tag{4.40}$$

where N_+ and N_- is the number of sheets to the left and right of $\tilde{\theta}_0$.

Then:

$$E_z(\tilde{\theta}) = -2\tilde{\theta} N\sigma + 2\pi\sigma\left(N_- - N_+\right). \tag{4.41}$$

There is a proportionality relation between N_+, N_- and N expressed as:

$$N_\pm = \frac{\pi \mp \tilde{\theta}_0}{2\pi} N. \tag{4.42}$$

Substituting Eq. (4.42) in Eq. (4.41) and using the relation between σ and n_0:

$$E_z(\tilde{\theta}) = \frac{4\pi e n_0}{k_p}\left(-\tilde{\theta} + \tilde{\theta}_0\right). \tag{4.43}$$

Substituting Eq. (4.43) and Eq. (3.16) in Eq. (4.34) (using also the definition of $\eta = \omega/\omega_p$):

$$\frac{d}{dz}\left(\delta\gamma\right) = -\frac{a_w}{2\gamma_0}\left(\tilde{a}e^{i\tilde{\theta}} + c.c.\right) + {v_p}^2\eta^2\left(\tilde{\theta}_0 - \tilde{\theta}\right). \tag{4.44}$$

Eq. (4.44) is an equation to describe the evolution of the energy fluctuation and depends on the laser amplitude (that is described by the linear equations) and on the phase $\tilde{\theta}$ (there is no γ-dependence).

4.2.3 Second-Order ODE for the Phase

The ordinary differential equations (ODEs) for the phase and the energy fluctuation can be combined in a single second-order ODE. For this, Eq. (4.32) is derived again in relation to the space. Then:

$$\frac{d^2}{dz^2}\tilde{\theta} = \left(\frac{1+{a_w}^2}{v_p {v_p}' {\gamma_0}^3}\right)\frac{d}{dz}\left(\delta\gamma\right). \tag{4.45}$$

Substituting the first-order ODE for the energy fluctuation Eq. (4.44) in Eq. (4.45) is found that:

$$\frac{d^2}{dz^2}\tilde{\theta}_j = -\chi_1\left(\tilde{a}e^{i\tilde{\theta}_j} + c.c.\right) + \chi_2\left(\tilde{\theta}_{oj} - \tilde{\theta}_j\right), \tag{4.46}$$

where:

$$\chi_1 \equiv \left(\frac{a_w}{2v_p {v_p}'}\right)\left[\frac{1+{a_w}^2}{{\gamma_0}^4}\right], \tag{4.47}$$

$$\chi_2 \equiv \eta^2\left(\frac{v_p}{{v_p}'}\right)\left[\frac{1+{a_w}^2}{{\gamma_0}^3}\right]. \tag{4.48}$$

Eq. (4.46) is a simplified equation to describe the particle dynamics. The particle phase $\tilde{\theta}_j$ depends on the particle initial phase $\tilde{\theta}_{0j}$.

4.2.4 Second-Order ODE for the Compressibility

One of the targets of the semi-analytical model is to estimate the position of the onset of mixing. To find this position, we look at the particle phase evolution for different initial phases. The position $\tilde{\theta}_0$ is known, unless $\partial\tilde{\theta}_i/\partial\tilde{\theta}_{0i} \to 0$. If $\partial\tilde{\theta}_i/\partial\tilde{\theta}_{0i} = 0$, there is local divergence in the charge density, what pinpoints the onset of mixing. At this moment the model is not valid anymore.

The position which physically represents the onset of mixing is obtained, via the semi-analytical model, through the variation of the initial phase $\tilde{\theta}_{0i}$: the initial phase that minimizes the position z until the onset of mixing is the one with physical meaning and its position when $\partial\tilde{\theta}_i/\partial\tilde{\theta}_{0i} = 0$ is approximately the time of the onset of mixing.

Thus, defining a new quantity, the compressibility factor (C), as:

$$C \equiv \frac{\partial \tilde{\theta}}{\partial \tilde{\theta}_0}. \tag{4.49}$$

And deriving Eq. (4.46) with respect to $\tilde{\theta}_0$:

$$\frac{d^2}{dz^2}C = -i\chi_1 \left(\tilde{a} e^{i\tilde{\theta}_j} - c.c. \right) + \chi_2 \left(1 - C \right). \tag{4.50}$$

The evolution of the compressibility factor is obtained with the simultaneous integration of the complete set of linear equations (Eqs. (4.11), (4.16) and (4.21)), the second-order differential phase equation (Eq. (4.46)) and the second-order differential compressibility equation (Eq. (4.50), with the following initial conditions (where $\dot{\xi} = d\xi/dz$):

$$\begin{cases} \tilde{\theta}\left(z=0\right) = \tilde{\theta}_0, \\ \dot{\tilde{\theta}}\left(z=0\right) = 0, \\ C\left(z=0\right) = 1, \\ \dot{C}\left(z=0\right) = 0. \end{cases} \tag{4.51}$$

Compressibility oscillates fast with a slow modulation. The modulation is scaled by the laser field growth.

When space-charge effects are insignificant, the coulombian repulsion between the particles is small. Then, the laser dynamics driven the particles motion, making the particles get closer from each other. Even when the local density in the bottom of the ponderomotive well is big, the ponderomotive force is greater than the coulombian repulsion force. Thus, particles overtake each other in the phase-space ($\tilde{\theta} \times v_z$ or $\tilde{\theta} \times \gamma$). This is the case of the Compton regime. In terms of the compressibility factor, in its evolution, the compressibility factor goes to zero without oscillations.

In the other hand, when space-charge effects are relevant in the dynamics, coulombian repulsion between the particles is comparable to the ponderomotive well. In this case we are in the Raman

regime. When local density in the bottom of the ponderomotive well is big, the ponderomotive force is comparable to the coulombian force. Moreover, there is a big electric barrier, which imposes some difficulty when particles overtake each other in the phase-space. Typically, in the compressibility evolution, it is seen an extra cycle added before compressibility goes to zero.

Finally, when the current density exceeds the maximum value to generate the proper conditions for the laser growing, the particles, as already stated, do not overtake each other in the phase-space, because the laser field does not grow and, then, the ponderomotive force is smaller than the coulombian repulsion. In this case, the compressibility oscillates around its initial value with small amplitude. It means that the local density does not vary significantly.

4.3 Results

In this section, the results are presented. A comparison between the results given by the particles-wave equations and the semi-analytical model is made. Some of the results are also shown in Refs. [16, 17].

4.3.1 Equivalence in Stable Regions

The FEL dynamics is completely described by the linear set of equations in the stable regime (with no laser field growing). In Fig. 4.2 the equivalence is shown through the evolution of the laser amplitude for 1000 interacting particles. The parameters used are $a_w = 0.4; a(z = 0) = i\, a_w\, 10^{-5}; \eta = 0.07; \nu = 0.01; v_p = 0.99$. Those parameters, as can be seen in Fig. 4.4, correspond to a stable region.

The solid curve represents the solution through the integration of the particles-wave set of equations, while the circles are from the integration of the linear set of equations. The linear equations can provide a very good agreement with the particles-wave set of equations in stable regions.

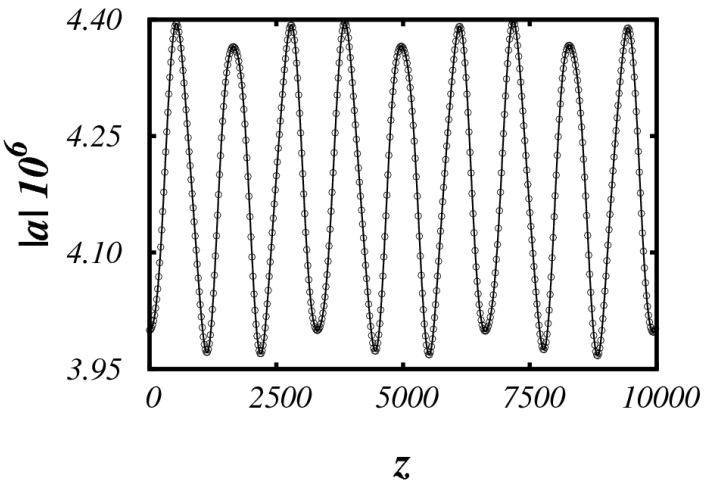

Fig. 4.2: Equivalence in a stable region. The solid curve was obtained from the integration of the particles-wave equations, while the circles were obtained from the linear set of equations.

4.3.2 Limit Curves

The limit curves of instability delimits the parameters which led to instabilities and consequently to laser field growth. The limit and the maximum growing rate curves can be found through the dispersion relation Eq. (4.26), imposing that λ must be complex. These curves are of great importance in the laboratory, because it leads to a reduction of the wiggler length. The limit curves and the maximum growing rate curve are shown in Fig. 4.3 (with $a_w = 0.5; a(z=0) = i\,a_w\,10^{-5}; v_p = 0.99$) and in Fig. 4.4 (with $a_w = 0.4; a(z=0) = i\,a_w\,10^{-5}; v_p = 0.99$).

In Figs. 4.3 and 4.4, the colors indicate the time until the onset of mixing (z_{wb}). This time decreases as the charge of the system (η) increases. The curve of maximum growth rate is identical to the curve of minimum z_{wb} varying η (as can be seen better in Fig. 4.4). Another feature that can be seen in the map is that as the value of η decreases, the detuning needed to enable the laser growth is smaller. In the limit of $\eta \to 0$ the instable region extends to values increasingly negative of detuning.

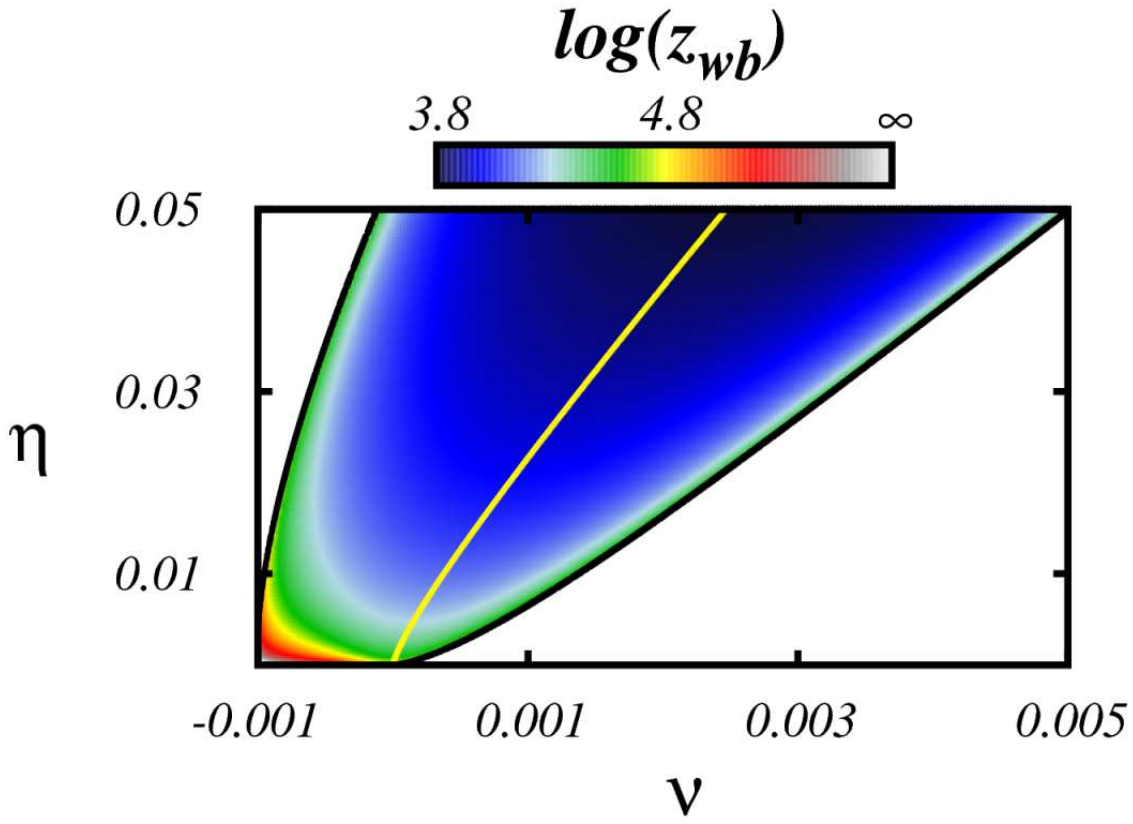

Fig. 4.3: Map of parameter space. White regions represent stability (no laser field growth). Colors indicate the time until the onset of mixing via particles-wave set of equations. Yellow solid line means the detuning which maximizes the growth rate for a specific η via linear analysis. Black lines delimit the instability region, through linear analysis. The figure was made with: $a_w = 0.5; a(z = 0) = i\, a_w\, 10^{-5}; v_p = 0.99$.

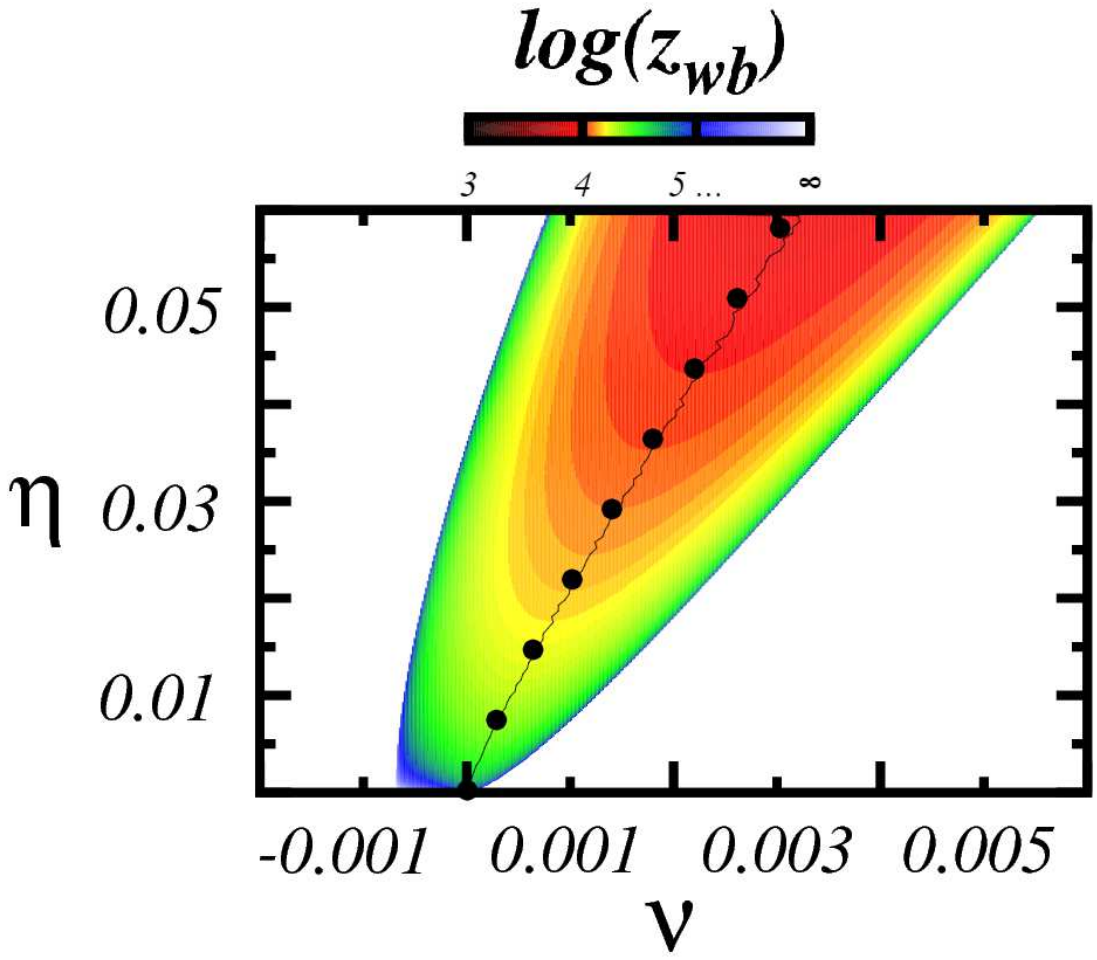

Fig. 4.4: Map of parameter space. White regions represent stability (no laser field growth). Colors indicate the time until the onset of mixing via particles-wave set of equations. The circles symbolize the parameters for the maximum growth rate curve while the thin line represents the parameters for minimum time for the onset of mixing. The figure was made with: $a_w = 0.4; a(z = 0) = i\, a_w\, 10^{-5}; v_p = 0.99; N = 1000$ particles.

4.3.3 Time until the Onset of Mixing

One of the goals of the semi-analytical model is to estimate the time until the onset of mixing. In Fig. 4.5 the time predicted by the model is compared with the results given by the integration of the particles-wave equations. This figure was generated for $a_w = 0.4; a(z=0) = i\, a_w\, 10^{-5}; v_p = 0.99$.

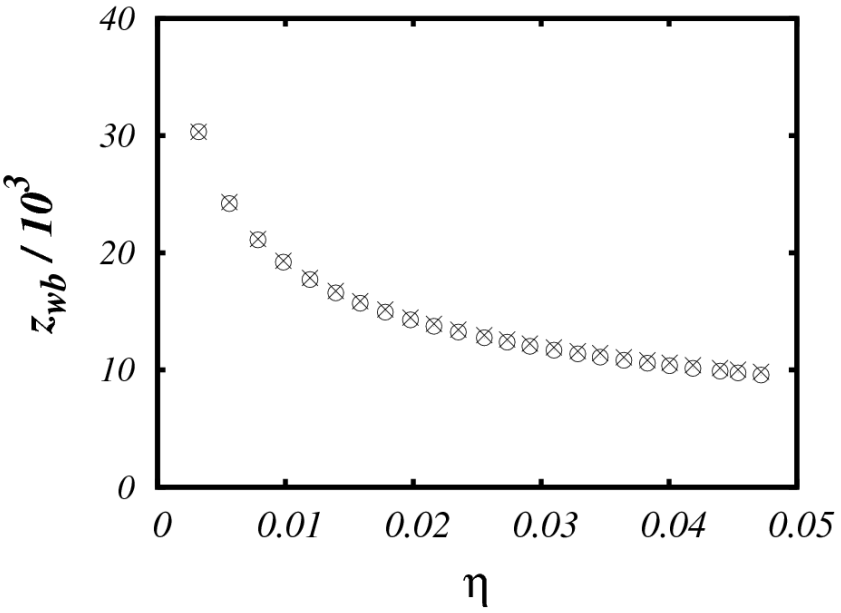

Fig. 4.5: Time until the onset of mixing vs. η. The time obtained through the model is represented by the crosses, while the time obtained via particles-wave simulations is shown with circles.

In Fig. 4.5, the chosen ν for each η corresponds to the pair $\eta - \nu$ which maximizes the growth rate curve, according to the solid thin line of Fig. 4.4. To execute the particles-wave simulations, 5000 particles were used.

The results given by the model are reasonable in comparison with the particles-wave simulations.

4.3.4 Saturation Amplitude Estimative

The model is useful to estimate the saturation amplitude of the laser field as well. The saturation of the amplitude is related with the relaxation process in FEL. There is a non-stationary final state in which the electrons are distributed in the phase-space with large energy dispersion. This dispersion

does not enable the electrons to form bunches as in the linear regime. Then, the radiation amplitude varies around a mean value.

The saturation amplitude is simply estimated as the linear amplitude of the laser obtained from the simplified model, evaluated at the mixing onset time z_{wb}: $a_{sat}^{mod} \equiv |a(z = z_{wb}|$. The corresponding relaxed amplitude arising from simulations a_{sat}^{sim} is calculated as we perform a time average of the amplitude over a relatively large time stretch following the onset of mixing. Our choice here is to perform the average from z_{wb} to $3\, z_{wb}$.

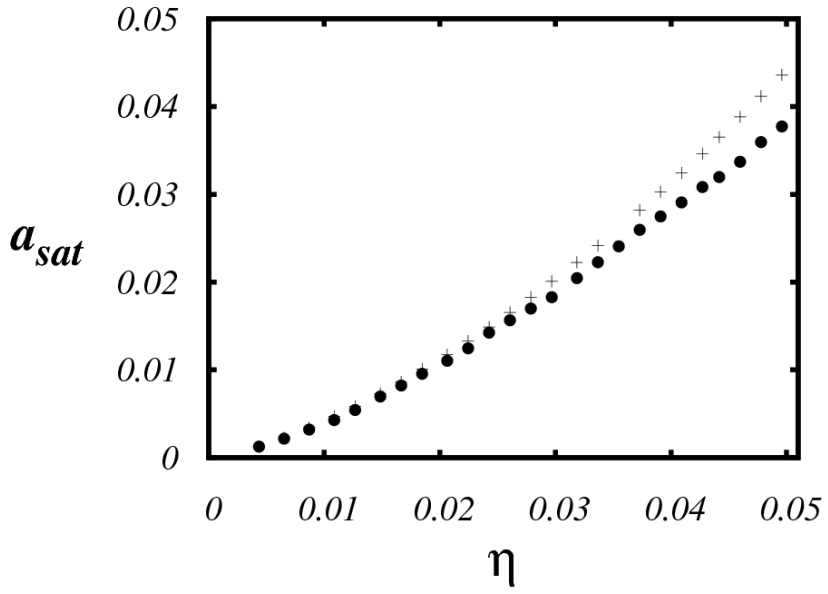

Fig. 4.6: Saturated amplitudes of the stimulated laser field. The crosses were obtained from the semi-analytical model, while the filled circles were obtained from particles-wave simulations with $N = 1000$ particles.

Results are plotted in Fig. 4.6 and indicate good agreement between the two approaches. A more judicious look at Fig. 4.6 actually shows that the two curves begin to move apart at larger values of the charge and field. The discrepancy is mainly related to the assumption of a linear dynamics for the laser field: any small error in the onset time leads to relatively large errors in the estimates of the exponentially growing stimulated radiation.

4.3.5 Phase Position on the Onset of Mixing

As an academic prediction (there is no practical application for this), the model is able to estimate the position, inside of the ponderomotive potential, of the onset of mixing. In this position, the particle distribution in the phase-space becomes a non-single-valued function anymore. This position is obtained in the particles-wave simulations when a particle overtakes another one for the first time; in the model, this position is given by $\tilde{\theta}$ when compressibility goes to zero (the transformed phase $\tilde{\theta}$ must be converted in the original one θ through Eq. (4.1)).

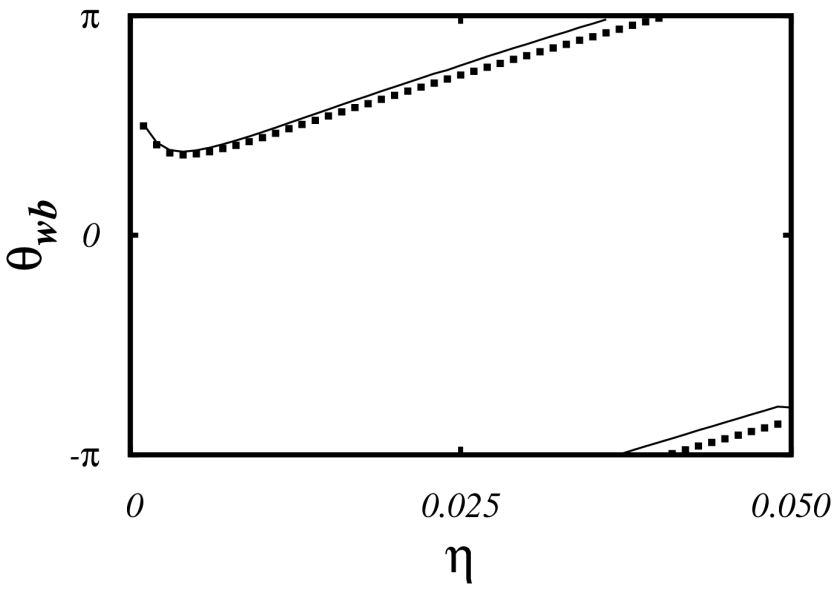

Fig. 4.7: Position of the onset vs. η. Filled squares are the results from particles-wave simulations (with $N = 1000$ particles) and the solid line is the result from the semi-analytical model, with $a_w =$ **0.5**; $a(z = 0) = i\, a_w\, 10^{-5}$; $v_p = 0.99$, over the curve of maximum growth rate.

The results are presented in Fig. 4.7 for $a_w =$ **0.5**; $a(z = 0) = i\, a_w\, 10^{-5}$; $v_p = 0.99$. Once again, the η is connected with ν to fill the condition of the maximum growth rate, denoted by the yellow line in Fig. 4.3. The model results are given by the solid line, while the particles-wave results are given by the filled squares. The agreement between the results is reasonable.

4.3.6 Regimes Definitions

In a simply way, if the charge in the system is small, the compressibility goes to zero without oscillations. But, if the charge is big, the compressibility goes to zero after oscillates around its initial value. This behavior can be seen in Fig. 4.8 (the figure was built with $a_w = 0.4; a(z = 0) = i\, a_w\, 10^{-5}; v_p = 0.99; N = 1000$ particles).

In panel (a) of Fig. 4.8, the evolution of the compressibility is shown for the Compton regime (with $\eta = 0.001$: this charge corresponds to the Compton regime, as it can be seen in Fig. 4.9). In panel (b) of the same figure, the compressibility is presented for the Raman regime (with $\eta = 0.05$). In panel (c), that is a zoom of panel (b), we put in evidence the initial oscillations of the compressibility around its initial value. These oscillations show that space-charge effects are relevant for the system evolution.

The distinction between the regimes is, therefore, based on compressibility: moving over the maximum growth rate curve, we analyze the number of times that compressibility passes by its initial value. If the charge adds an extra cycle in compressibility, this charge is named the critical charge of the transition between Compton and Raman regimes (η_c).

The critical charge (η_c) is plotted against the wiggler field amplitude (a_w) in Fig. 4.9. The solid line is the result obtained from the semi-analytical model. The filled squares are the results from the particles-wave simulations (the compressibility factor was introduced in the integration process, to establish its evolution). The case of $a_w = 1$ has been discussed in Ref.[11]. For $v_p = 0.99$, the chosen value of η to illustrate space-charge effects reads 0.04, which is indeed already in the Raman region obtained with the present analysis $\eta_c(a_w = 1) \sim 0.025$[16].

The region above (bellow) the transition curve corresponds to the Raman (Compton) regime, in which space-charge-effects are (not) relevant for the system dynamics. A good agreement is seen between the results. It evidences the good estimation power of the model.

At last, the way the onset of mixing takes form in Compton and Raman regimes is absolutely different. As discussed early, in Compton regime, the space-charge effects are not relevant for the

system dynamics. Thus, the onset of mixing in this regime occurs like the particle distribution revolves as whole around itself in phase-space, as can be seen in panel (a) of Fig. 4.10 (the figure was built with $a_w = 0.4; a(z=0) = i\,a_w\,10^{-5}; v_p = 0.99; \eta = 0.001$)[23].

In Raman regime, relaxation is better described in terms of jets emanating from the core of the particle distribution, as in core-halo systems, like is shown in panel (b) of Fig. 4.10 (the figure was built with $a_w = 0.4; a(z=0) = i\,a_w\,10^{-5}; v_p = 0.99; \eta = 0.05$)[29]. Jets are formed by charge density piling up, which creates regions of singular acceleration. Jets are not actually absent in the Compton regime, but due to low amount of charge, they are overshadowed by the ponderomotive acceleration.

Even though the ponderomotive well is not stationary, the dynamics at low and high values of η, respectively, bear some resemblance to the dynamics of fast and slow wave-breaking in magnetostatically confined beams. We recall that fast wave-breaking occurs when magnetic focusing is strong and waves break in less than an oscillatory cycle, with slow wave-breaking occurring only after a series of oscillatory cycles[29, 30].

4.4 Conclusion

In this chapter a linear analysis was developed, providing the parameters that lead to instability and to the laser growth. A semi-analytical model based on the compressibility factor (whose zeroes of the compressibility indicate the onset of mixing in the particle phase-space) was proposed to estimate some FEL quantities in the moment of the onset of mixing: the time until the onset; the saturated amplitude of the stimulated radiation field; the position of the onset. Furthermore, the model shown to be able to set a distinction between Compton and Raman regimes. Making use of this delimitation, we compared the phase-space of the system immediately after the onset of mixing for Compton and Raman regimes. There is a significant difference in the form which the mixing occurs and, certainly, the difference is caused due to the space-charge effects. Some of the results shown here were presented in a paper[16].

Finally, the model proved to be reasonable to estimate those quantities, as can be seen in the Section 4.3, being a powerful tool to predict the system behavior with smaller computational time spent in comparison to the particles-wave simulations. It is an interesting feature when you are looking for the parameters which maximize the FEL efficiency. This way, we may consider compressibility a helpful tool to model FEL dynamics.

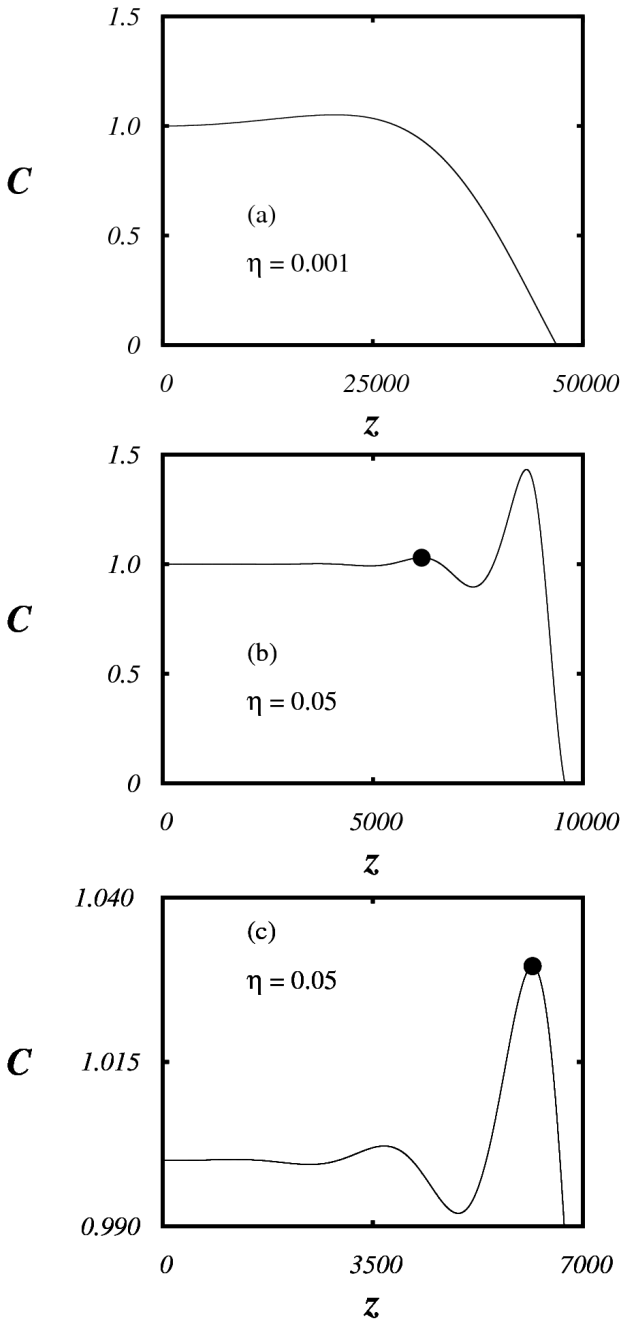

Fig. 4.8: Evolution of C *versus* z: in panel (a) is the Compton regime; in panel (b) and (c) is the Raman regime. The panel (c) is a zoom of panel (b) to emphasize the extra cycle added in compressibility due the space-charge effects. The filled circles represent the same point in panel (b) and (c). The parameters are over the maximum growth rate curve.

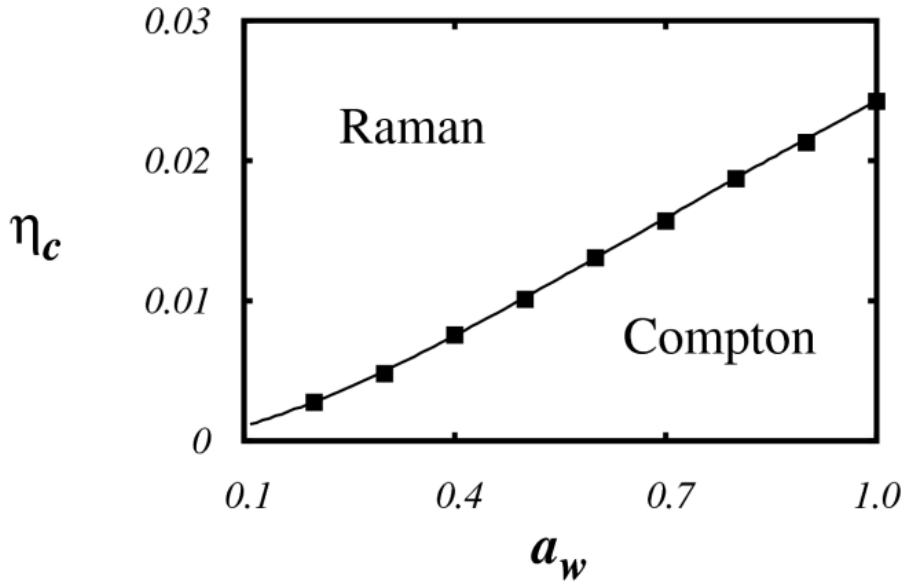

Fig. 4.9: Critical charge (η_c) for different a_w values over the maximum growth rate curve. Filled squares represent the results obtained from particles-wave simulations and the solid line represents the semi-analytical results. The curve is an interface between Raman (above) and Compton (bellow) regimes.

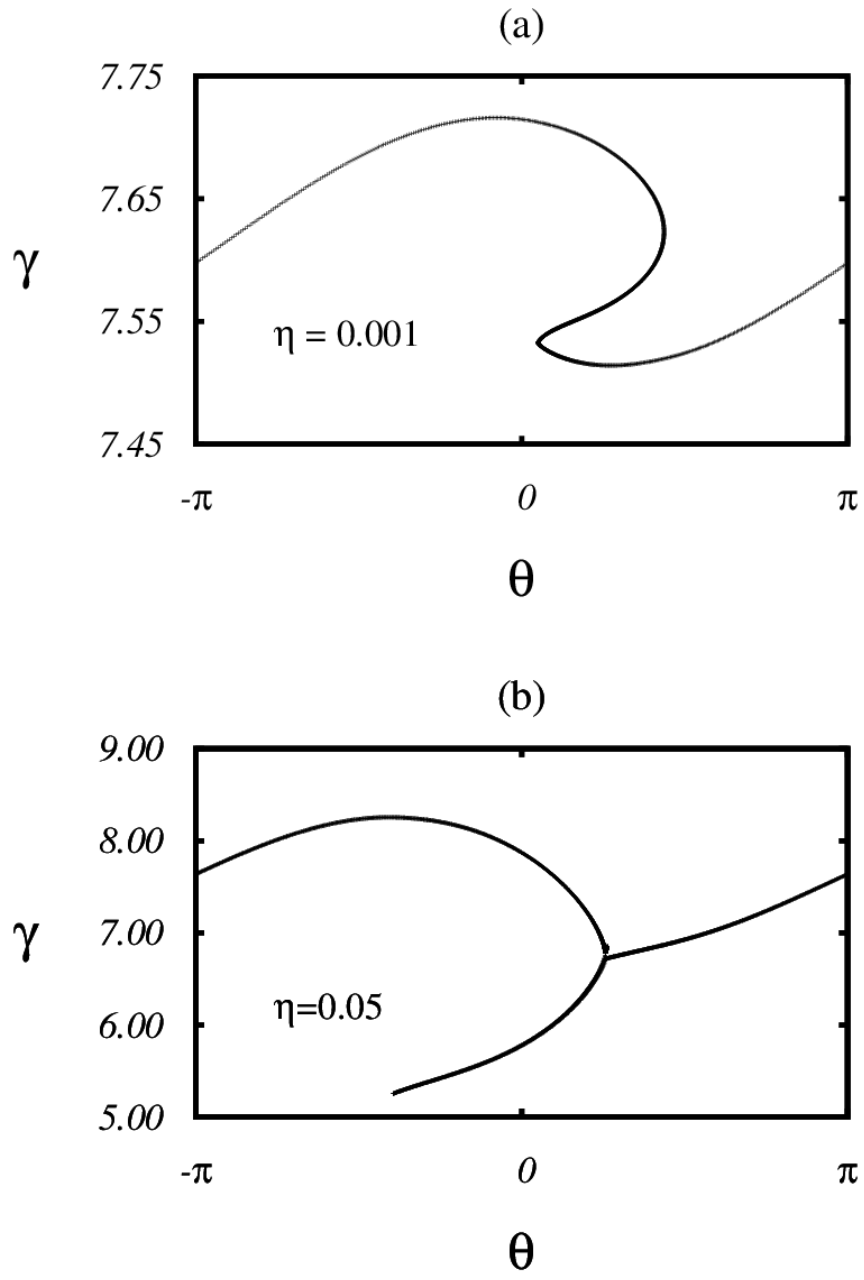

Fig. 4.10: Phase-space configuration just after the onset of mixing. In panel (a), Compton regime: the space-charge effects are not relevant for the system dynamics. In panel (b), Raman regime: space-charge effects cause a jet of particles emitted from the core of the distribution.

Chapter 5

Water Bag Distribution

During the acceleration and transport processes of the electron beam, some electrons receive more energy than the others, i.e. the particle accelerator is unable to provide a completely monoenergetic beam. The width and the shape of the energy spread are function of the quality and type of the particle accelerator. But, in fact, besides its quality, the energy distribution always occurs.

The presence of velocity spread in the transport of charged beams affects the overall system performance for any application where beams interact with ambient wave modes. Interestingly, not always is the spread detrimental. In the case of beams with inhomogeneous transverse profiles, for instance, a coplanar transverse velocity spread may actually prevent the appearance of strong nonlinear features like wave-breaking and the undesired associated emittance growth[29]. In most cases, however, fine tuning control between the beam velocity and the phase-velocities of the relevant wave modes present in the system is needed. Under these conditions, the usual requirement for a good quality beam is that the velocity spread of the beam be much smaller than all relevant velocity scales of the problem[18].

In Free-Electron Lasers, to obtain an efficient interaction, large velocity spreads (in the order of the detuning that maximizes the laser growth rate) must be avoided[11, 31, 32, 33].

For a monoenergetic beam, the onset of mixing was associated to the zeroes of the compressibility factor. But, in fact, the compressibility factor is the inverse of the density function. Thus, the zeroes

of the compressibility factor indicates an infinite local value of the density function (that is exactly in the position of the onset of mixing).

After the onset of mixing, coherence is lost and the amplifying signal saturates. Based on this set of features, a cold fluid model was then developed to estimate both the transition time and the saturated levels. The model was shown to agree well with particles-wave simulations.

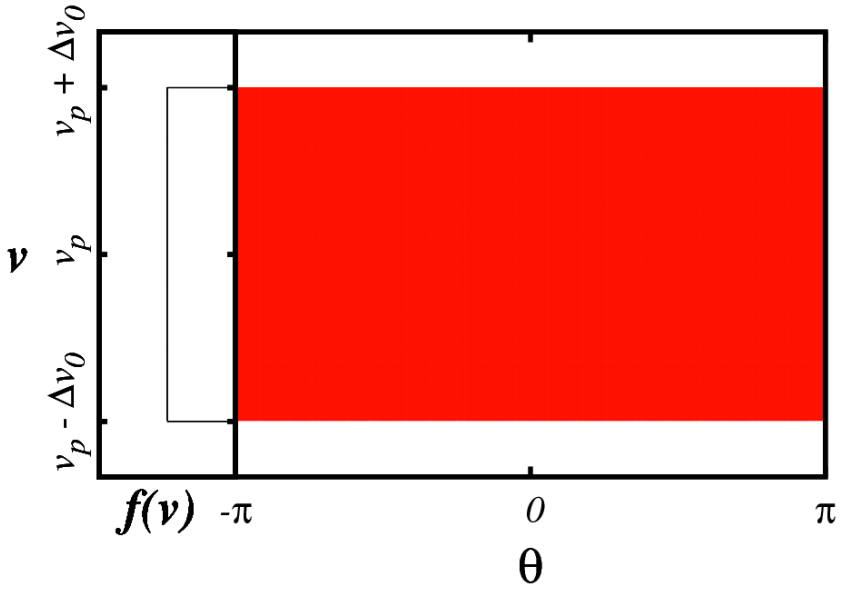

Fig. 5.1: Initial distribution $f(v)$ of the electron beam: a water bag distribution. The color represents the homogeneous electron density in the phase-space.

In this chapter we include thermal effects (caused due to the presence of the velocity spread) in the original model based on the compressibility factor, considering an uniform water bag lying along the phase θ, with a small half-width Δv_0 around an average injection velocity v_0 (the distribution function is shown in Fig. 5.1). We point out that due to the smallness of the velocity width, a very realistic assumption for FELs,[34] the connections between the widths in velocity, momentum, and energy spaces are approximately linear. Under the linearity condition, if the phase-space density is a constant in one representation, it is also constant in the others. With views at the warm fluid modeling, this is why we decided to work with the velocity space[18].

We should like to perform a similar analysis made in the Chapter 4, but now for a warm beam

with a small but finite spread of longitudinal velocities. This poses an initial problem which comes from the fact that, in principle, even the laminar regime here requires a kinetic description based on the full phase-space. To deal with this problem, and still make use of macroscopic fluid quantities like the compressibility, we add a pressure term to the cold fluid model developed in Chapter 4. This technique has been applied in related beam systems[30] and revealed nice agreement with full simulations[18].

The presence of infinite densities ceases to occur when the velocity spread is added. The reason is because the spread is equivalent to the inclusion of temperature and the expanding effects of pressure in the fluid equations. However, preceding mixing regimes, one still encounters singularities, now arising from the formation of discontinuities in the compressibility and density. This is precisely what has been recently observed in the dynamics of inhomogeneous magnetically confined warm beams, where divergent density peaks of cold beams are replaced with density discontinuities as pressure is added to the system[30]. The results given by the nonlinear model are compared with the particles-wave simulations and a discussion is made to investigate the role of velocity spreads in the instability, mixing and saturation of FELs[18].

5.1 Pressure Term

In the present section we develop the thermal effect in order to add it in the previous model. First, we establish a linear relation to add the pressure term in the linear set of equations. Second, we go further and we consider nonlinearities due to the thermal effect: the resulting term is added to the nonlinear model.

We start considering the phase-space $\theta \times \dot{\theta}$: the electronic density (n) can be expressed in terms of the electronic distribution function (f) in the form:

$$n(\theta, t) = \int f(\theta, \dot{\theta}, t) d\dot{\theta}. \tag{5.1}$$

The mean velocity is obtained from the mean definition, resulting in:

$$\bar{\dot{\theta}}(t) = \frac{\int \dot{\theta} f(\theta, \dot{\theta}, t) d\dot{\theta}}{\int f(\theta, \dot{\theta}, t) d\dot{\theta}} = \frac{\int \dot{\theta} f(\theta, \dot{\theta}, t) d\dot{\theta}}{n(\theta, t)}. \tag{5.2}$$

Usually, the standard solution for the Vlasov equation requires a chain of moments equations. Then, Eq. (5.2) is generalized for the r-order moment:

$$\bar{\dot{\theta}}^r n = \int \dot{\theta}^r f(\theta, \dot{\theta}, t) d\dot{\theta}. \tag{5.3}$$

Neglecting the effects of collisions, the electronic distribution function must satisfy the unidimensional Vlasov equation:

$$\frac{\partial f}{\partial t} + \dot{\theta}\frac{\partial f}{\partial \theta} + \ddot{\theta}\frac{\partial f}{\partial \dot{\theta}} = 0. \tag{5.4}$$

The continuity equation is obtained integrating Eq. (5.4) over the velocities:

$$\int_{-\infty}^{\infty} \frac{\partial f}{\partial t} d\dot{\theta} + \int_{-\infty}^{\infty} \dot{\theta}\frac{\partial f}{\partial \theta} d\dot{\theta} + \ddot{\theta}\int_{-\infty}^{\infty} \frac{\partial f}{\partial \dot{\theta}} d\dot{\theta} = 0. \tag{5.5}$$

Using the commutability between time and velocity, the first term of Eq. (5.5) is written as:

$$\int_{-\infty}^{\infty} \frac{\partial f}{\partial t} d\dot{\theta} = \frac{\partial}{\partial t}\int_{-\infty}^{\infty} f d\dot{\theta} = \frac{\partial}{\partial t} n. \tag{5.6}$$

Using the commutability between velocity and position, the second term of Eq. (5.5) is written as:

$$\int_{-\infty}^{\infty} \dot{\theta}\frac{\partial f}{\partial \theta} d\dot{\theta} = \frac{\partial}{\partial \theta}\int_{-\infty}^{\infty} \dot{\theta} f d\dot{\theta} = \frac{\partial}{\partial \theta}\left(n\bar{\dot{\theta}}\right). \tag{5.7}$$

While, the third term of Eq. (5.5) vanishes:

$$\ddot{\theta}\int_{-\infty}^{\infty} \frac{\partial f}{\partial \dot{\theta}} d\dot{\theta} = f|_{\dot{\theta}=\infty} - f|_{\dot{\theta}=-\infty} = 0. \tag{5.8}$$

This way, Eq. (5.5) is finally rewritten as:

$$\frac{\partial}{\partial t}n = \frac{\partial}{\partial \theta}\left(n\bar{\dot{\theta}}\right). \tag{5.9}$$

Eq. (5.9) clearly depends on n and $\bar{\dot{\theta}}$. To form a closed set of equations, Eq. (5.4) is multiplied by the velocity and then integrated over the velocities, resulting in:

$$\int_{-\infty}^{\infty}\dot{\theta}\frac{\partial f}{\partial t}d\dot{\theta} + \int_{-\infty}^{\infty}\dot{\theta}^2\frac{\partial f}{\partial \theta}d\dot{\theta} + \ddot{\theta}\int_{-\infty}^{\infty}\dot{\theta}\frac{\partial f}{\partial \dot{\theta}}d\dot{\theta} = 0. \tag{5.10}$$

Making use of the commutability between time and velocity, the first term of (5.10) becomes:

$$\int_{-\infty}^{\infty}\dot{\theta}\frac{\partial f}{\partial t}d\dot{\theta} = \frac{\partial f}{\partial t}\int_{-\infty}^{\infty}\dot{\theta}d\dot{\theta} = \frac{\partial}{\partial t}\left(n\bar{\dot{\theta}}\right). \tag{5.11}$$

Using the commutability between velocity and position, the second term of (5.10) becomes:

$$\int_{-\infty}^{\infty}\dot{\theta}^2\frac{\partial f}{\partial \theta}d\dot{\theta} = \frac{\partial f}{\partial \theta}\int_{-\infty}^{\infty}\dot{\theta}^2 d\dot{\theta} = \frac{\partial f}{\partial \theta}\left(\bar{\dot{\theta}^2}\right). \tag{5.12}$$

While the third term of (5.10) is reduced to:

$$\int_{-\infty}^{\infty}\dot{\theta}\frac{\partial f}{\partial \dot{\theta}}d\dot{\theta} = \dot{\theta}f|_{v=\pm\infty} - \int_{-\infty}^{\infty}f d\dot{\theta} = -n. \tag{5.13}$$

Therefore, the first order moment of the Vlasov equation becomes:

$$\frac{\partial}{\partial t}\left(n\bar{\dot{\theta}}\right) + \frac{\partial}{\partial \theta}\left(n\bar{\dot{\theta}^2}\right) - n\ddot{\theta} = 0. \tag{5.14}$$

Or, simply:

$$\left(\frac{\partial \bar{\dot{\theta}}}{\partial t} + \bar{\dot{\theta}}\frac{\partial \bar{\dot{\theta}}}{\partial \theta}\right) + \frac{1}{m\,n}\left(\frac{\partial p}{\partial \theta}\right) - \ddot{\theta} = 0, \tag{5.15}$$

where p is the fluid pressure, that depends on the velocity spread and m is the mass of the electron.

Eq. (5.15) for the beam is similar to the Navier-Stokes equation.

It is possible to identify in Eq. (5.15) the thermal contribution for the system dynamics. This contribution is expressed as:

$$\ddot{\theta}|_{ther} = \frac{\partial^2\theta}{\partial t^2}\Big|_{ther} = -\frac{1}{m\,n}\left(\frac{\partial p}{\partial \theta}\right). \tag{5.16}$$

Considering a steady-state regime, i.e. **time independent**, from Eq. (5.9) we obtain that:

$$n\bar{\dot{\theta}} = n_0\bar{\dot{\theta}}_0, \tag{5.17}$$

or:

$$n\partial\theta = n_0\partial\theta_0. \tag{5.18}$$

Thus:

$$\frac{\partial^2\theta}{\partial t^2}\Big|_{ther} = \frac{\partial^2\theta}{\partial z^2}\Big|_{ther} = \frac{1}{m\,n}\left(\frac{\partial p}{\partial \theta_0}\right). \tag{5.19}$$

The electric distribution function (f), for the initial configuration, is written as a constant:

$$f = \frac{n_0}{2\Delta\dot{\theta}_0}. \tag{5.20}$$

While the pressure for the charged fluid is described by (the following expression is valid for nonrelativistic water bag distributions with constant density over the phase-space)[35]:

$$p = m\left(\frac{\Delta\dot{\theta}_0}{3{n_0}^2}\right)n^3. \tag{5.21}$$

This way, the force due to the thermal effects is written as:

$$\frac{\partial^2\theta}{\partial z^2}\Big|_{ther} = -\left(\frac{\Delta\dot{\theta}^2}{3{n_0}^3}\right)\frac{\partial n^3}{\partial\theta_0} = -\frac{\Delta\dot{\theta}^2}{n_0}\frac{\partial n}{\partial\theta_0}. \tag{5.22}$$

Defining the compressibility factor as:

$$C = \frac{n_0}{n} = \frac{\partial \theta}{\partial \theta_0}. \tag{5.23}$$

During the linear regime, we assume that the compressibility factor is around its initial value, then:

$$n = \frac{n_0}{C} \cong n_0(1 - \delta C), \tag{5.24}$$

and:

$$\delta C = \frac{\partial \theta}{\partial \theta_0} - 1 = \frac{\partial}{\partial \theta_0}(\theta - \theta_0) = \frac{\partial \delta\theta}{\partial \theta_0}. \tag{5.25}$$

Thus:

$$\frac{\partial^2 \theta}{\partial z^2}\Big|_{ther} = -\Delta\dot{\theta}^2 \frac{\partial}{\partial \theta_0}(1 - \delta C) = \Delta\dot{\theta}^2 \frac{\partial^2}{\partial {\theta_0}^2}(\delta\theta). \tag{5.26}$$

For the **linear treatment** (used to simulate the laser field growing), an approximation is done for n, around its initial value, $n \approx n_0\,(1 - \delta C)$. Assuming initials oscillations in phase-space have the same wavelength of the ponderomotive well, $\frac{\partial^2}{\partial {\theta_0}^2}\delta\theta = -\delta\theta$:

$$\left(\frac{\partial^2 \theta}{\partial z^2}\right)_{ther} = -{v_p}^2 \Delta {\dot{\theta}_0}^2 (\theta - \theta_0). \tag{5.27}$$

Through the evolution of energy equation, it is possible to establish a connection between Eq. (5.8) and the linear set of equations described by the collective variables, then the additional term due to the thermal effect is written as:

$$\left(\dot{Y}\right)_{ther} = -\frac{\Delta {v_0}^2}{2 D_{\gamma^2} \gamma_0} X, \tag{5.28}$$

where Δv_0 is the initial half-width of the longitudinal velocity spread and $D_{\gamma^2} = \partial^2 v / \partial \gamma^2$.

In order to include **nonlinearities in the semi-analytical model** we rewrite Eq. (5.26) without

linear approximations:

$$\left(\frac{d^2\theta}{dz^2}\right)_{ther} = -\Delta {v_0}^2 \left[\frac{\partial\delta\theta}{\partial\theta_0} + 1\right]^{-4} \frac{\partial^2\delta\theta}{\partial {\theta_0}^2}. \tag{5.29}$$

5.2 Linear Analysis

In this section, we present a linear analysis based in perturbations, which implies in a linearization of the complete set of particles-wave equations and includes thermal effects. Instead of using the original physical quantities, we made use of the collective variables. The collective variables represent somehow the fluctuations in the values of the physical quantities. Through this analysis is possible to determine the linear growth rate of the laser field, the instability region (where occurs the laser growing) and the parameters to maximize the growth rate.

5.2.1 Phase Equation

The phase equation is not modified by the presence of the thermal effects. Thus, this equation is written exactly as Eq. (4.11):

$$\dot{X} = cY + id\tilde{a}, \tag{5.30}$$

where:

$$c = \frac{1 + {a_w}^2}{v_p {v_p}' {\gamma_0}^3}, \tag{5.31}$$

$$d = \frac{a_w}{2 v_p {v_p}' {\gamma_0}^2}. \tag{5.32}$$

5.2.2 Laser Equation

The laser equation is not modified by the presence of thermal effects as well. This equation is written exactly as Eq. (4.16):

$$\dot{\tilde{a}} = -h\left(iX + \frac{Y}{\gamma_0}\right) - ig\tilde{a}, \tag{5.33}$$

where:

$$g = v_p\frac{\eta^2}{2\gamma_0} - F(\nu), \tag{5.34}$$

$$h = v_p\frac{\eta^2 a_w}{2\gamma_0}. \tag{5.35}$$

5.2.3 Energy Equation

Finally, the energy equation is modified by the presence of thermal effects. A term expressed in Eq. (5.29) must be added in the cold beam case energy equation (Eq. (4.21)), in way that:

$$\dot{Y} = \left(\dot{Y}\right)_{ther} + \left(\dot{Y}\right)_{cold}. \tag{5.36}$$

Therefore:

$$\dot{Y} = -f\tilde{a} - eX, \tag{5.37}$$

where:

$$e = {v_p}^2\eta^2 + \frac{\Delta{v_0}^2}{2D_{\gamma^2}\gamma_0}, \tag{5.38}$$

$$f = \frac{a_w}{2\gamma_0}. \tag{5.39}$$

Eq. (5.37) evaluates the evolution of the fluctuations in the energy of the electrons.

With Eqs. (5.30), (5.33) and (5.37), the linear set of equations is complete. Through the linear set is possible to determine the parameters which lead to the maximum growth rate of the laser field. This set of equations simulate the laser amplitude evolution as well.

5.3 Nonlinear Model

In this section, a nonlinear model is proposed. The model provides a way to calculate the time for the breakdown of the laminar regime and subsequent relaxation and the saturated amplitude of the radiation field. The model, which is based on the compressibility factor, is used to evaluate the role of thermal effects. Instead of the cold beam case, compressibility does not vanish when there is an initial velocity spread, for this reason, a new model must be done. Basically, in the model, the linear equations of the previous section are used to simulate the laser field growing. It is a good assumption, once the system is almost linear until the breakdown of the laminar regime (as is seen in the particles-wave simulations). Moreover, nonlinearities caused due the presence of thermal and space-charge effects are introduced through an adiabatic fluid consideration and a connection between energy and phase equations and some considerations about the electric distribution.

The effect of the initial velocity spread over the dynamics of the variable θ is expressed in Eq. (5.29). This term must be add in Eq. (4.46) in order to have:

$$\frac{d^2}{dz^2}\tilde{\theta}_j = \frac{d^2}{dz^2}\tilde{\theta}_j\Big|_{cold} + \frac{d^2}{dz^2}\tilde{\theta}_j\Big|_{ther}. \tag{5.40}$$

Thus:

$$\frac{d^2}{dz^2}\tilde{\theta}_j = -\chi_1\left(\tilde{a}e^{i\tilde{\theta}_j} + c.c.\right) + \chi_2\left(\tilde{\theta}_{oj} - \tilde{\theta}_j\right) - {\Delta v_0}^2\left[\frac{\partial\delta\theta_j}{\partial\theta_{0j}} + 1\right]^{-4}\frac{\partial^2\delta\theta_j}{\partial{\theta_{0j}}^2}. \tag{5.41}$$

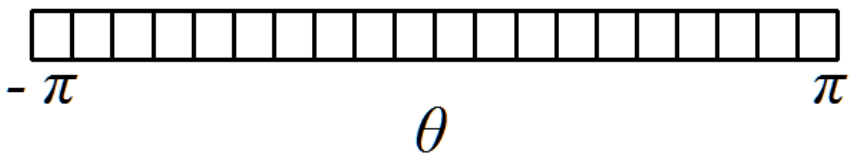

Fig. 5.2: Division of the particle beam in some elements between $\theta = -\pi$ and $\theta = \pi$.

In the case where thermal effects are included, the compressibility is not a direct tool to determine when occurs the onset of mixing, because particles overtake each other since the initial moment.

Therefore, the criterium adopted to determine the onset of mixing (i.e. the breakdown of the laminar regime) is the presence of discontinuities in the second derivative of the phase fluctuation in relation to the initial position of the element. It is important to notice that Eq. (5.41) is a partial differential equation that depends on z and on θ_0. To solve this equation, we divide the beam in elements, as can be seen in Fig. 5.2, integrating all of the elements simultaneously with a chain relation, where a periodic condition is imposed $\left(\delta\tilde{\theta}|_{\tilde{\theta}_0=-\pi} = \delta\tilde{\theta}|_{\tilde{\theta}_0=\pi}\right)$.

5.4 Results

In this section the results obtained from the particles-wave and the nonlinear model simulations are shown and compared. Some of the results are also shown in Ref.[18].

5.4.1 Maximum Growth Rate

The maximum growth rate curve has great importance in laboratories. The main reason for that is a better efficiency in the energy conversion process. Then, to obtain this curve is necessary to adjust the detuning.

In Fig. 5.3, a comparison is made between the maximizing detuning as a function of the initial spread Δv_0, both from the particles-wave simulations and from the simplified warm fluid model. The growth rate is obtained from simulations through a linear fitting for the numerically obtained $log(|a(z)|)$. The simulations were performed for $a_w = 0.4; a(z=0) = i\,a_w\,10^{-5}; v_p = 0.99; \eta = 0.03; N = 10000$ particles, which the parameters correspond to the high-gain Raman regime[11, 23, 36].

It is seen that despite the approximation based on the smallness of the velocity spread used for the warm fluid model, both results agree well. As a matter of fact, slight deviations can be observed from $\Delta v_0 = 0.001$ on, but those do not affect the general adequacy of the model within the range we are interested in. In this work we consider the maximum spread in the order of ν ($\Delta v_0 \sim \nu \sim 0.0002$). Higher values of the spread implicate in lower efficient interactions. Under the condition of $\nu > \Delta v_0$

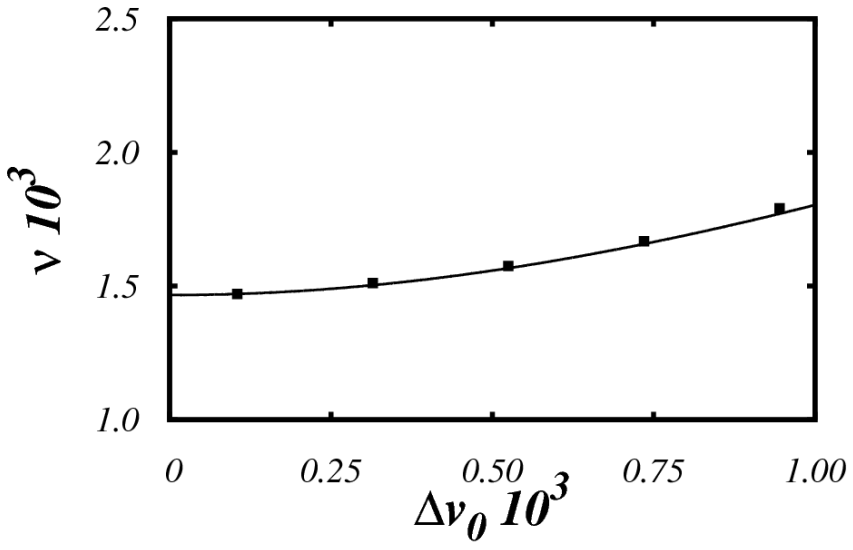

Fig. 5.3: The detuning ν for the maximum growth rate *versus* the initial spread Δv_0. Solid line was obtained from nonlinear model and filled squares from particles-wave simulations.

the system is as in a hydrodynamical regime[37]. The hydrodynamical regime therefore survives until $\Delta v_0 \sim \nu$, beyond which is becomes kinetic. The transition is not sharply defined, but with help of the linear dispersion relation one can solve for the corresponding Δv_0 satisfying the previous similarity condition.

The maximizing ν is calculated in terms of η with help of the cold beam dispersion relation (Eq. 4.26 with the inclusion of the pressure term shown in Eq. 5.38), we can estimate the transition value for Δv_0 directly in terms of the space-charge factor. As one reduces the spread, the beam gradually tends to the cold limit. The same occurs with the maximizing ν[18].

5.4.2 Laminar *versus* Mixing Regimes

When thermal effects are neglected, the transition can be identified with help of singularities in the electron density[16], as can be seen in Chap. 4. At the transition, the compressibility vanishes and the density diverges, which reflects the fact that the laminar electron distribution of cold beams is

twisted in a way that one can no longer establish single fluid variables at the same θ, i.e. the electric distribution is not a single valued function anymore. For sufficiently large values of the space-charge factor η, this kind of behaviour has been recognized in previous investigations as similar to wave-breaking processes[16, 18, 27, 38].

In the presence of thermal effects, the transition cannot be identified directly when the compressibility vanishes: it does not occur. The thermal effects add pressure to the warm fluid. Thus, local density never diverges.

The transition between the laminar and mixing regimes takes place when the compressibility and density become discontinuous. The instant when it occurs is denoted as z_b, with b standing for $breakdown$ (breakdown of the laminar regime). The meaning of this discontinuity is that fronts with different densities collide at the same phase coordinate[18].

The nonlinear model estimates the evolution of the electric density until the breakdown of the laminar regime. The electric density just after the breakdown is presented in Figs. 5.4 and 5.5. The Fig. 5.4 was built for $a_w = 0.4; a(z = 0) = i\, a_w\, 10^{-5}; v_p = 0.99; \eta = 0.03; \Delta v_0 = 0.00016$, while Fig. 5.5 was built for $a_w = 0.4; a(z = 0) = i\, a_w\, 10^{-5}; v_p = 0.99; \eta = 0.03; \Delta v_0 = 0.001$ (it is important to notice that in Fig. 5.5 the spread is ~ 6 times greater). The detuning used in the figures is the one which maximizes the growth rate.

In both figures, in panel (a) is shown the electric density obtained from the particles-wave simulations and in the panel (b) is shown the electric density obtained from the nonlinear model. The nonlinear model has a good agreement with the particles-wave simulations when we look at the peak, peak position and shape of the electric distribution in both cases.

The phase-space is presented in panel (c) of the Figs. 5.4 and 5.5. When the spread is small (Fig. 5.4), on the breakdown the peak of the local density is higher than when the spread is greater (Fig. 5.5). It occurs because smaller spreads correspond to smaller pressure forces. With smaller pressures, the particles can be closer to each other. The snapshots, revealing fingers that protrude from the lower border of the electron distribution, are also taken at the precise instant $-$ nearly the same as in the density counterparts $-$ where the density (obtained as an integral along the vertical axis) at both sides

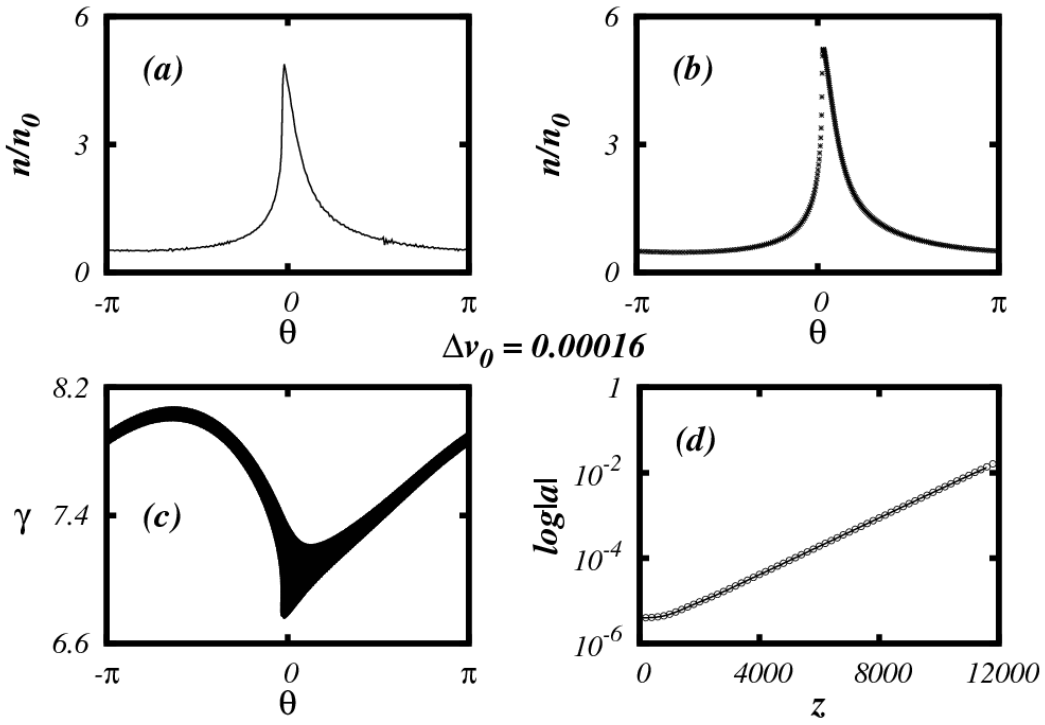

Fig. 5.4: (a) Longitudinal density obtained from particles-wave simulation on the breakdown; (b) Longitudinal density obtained from the nonlinear model on the breakdown; (c) Phase-space configuration for the wave-particles simulation; (d) Wave amplitude evolution along the time, for particles-wave simulation (solid line) and for the linear analysis (circles). The particles-wave simulation was performed with 40000 particles. The velocity half width is $\Delta v_0 = 0.00016$.

of the left boundary of the fingers becomes discontinuous as well. With greater spreads, can be the case that not all the electrons of the warm beam are active participants in the FEL interaction (in Fig. 5.5 an equivalently small fraction of electrons forms the finger)[18].

Finally, the panel (d) of the Figs. 5.4 and 5.5 shows the evolution of the modulus of the amplitude of the vector potential of the laser for the particles-wave simulations (solid line) and linear analysis (circles). The evolution described by the linear analysis well agree with the particles-wave simulations in the laminar regime.

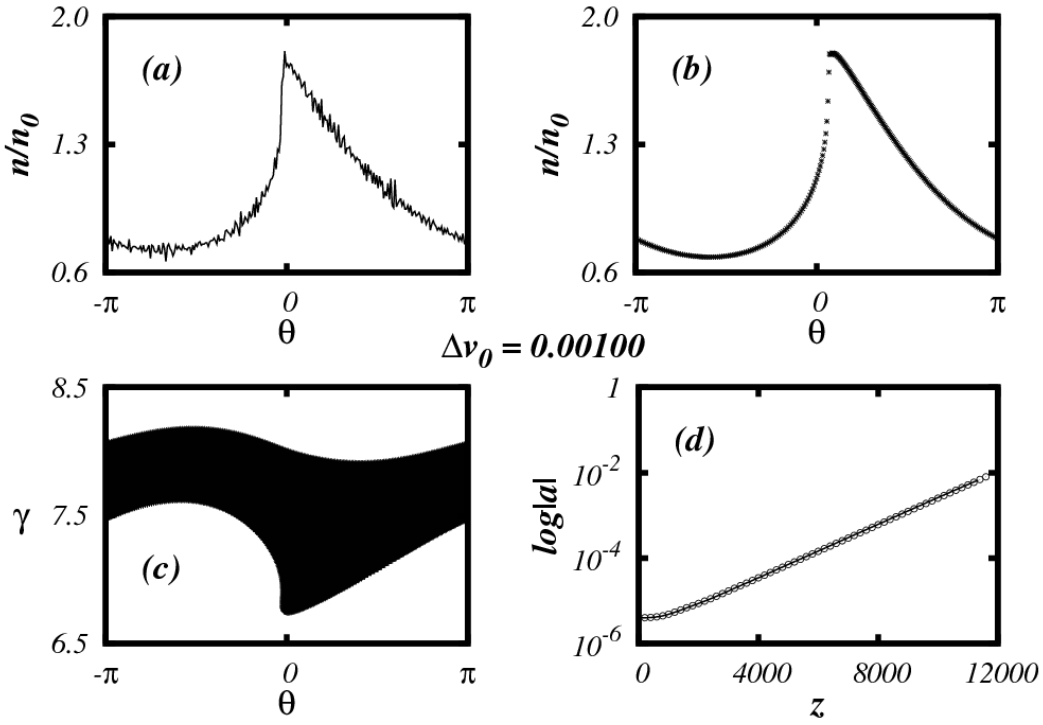

Fig. 5.5: (a) Longitudinal density obtained from particles-wave simulation on the breakdown; (b) Longitudinal density obtained from the nonlinear model on the breakdown; (c) Phase-space configuration for the wave-particles simulation; (d) Wave amplitude evolution along the time, for particles-wave simulation (solid line) and for the linear analysis (circles). The particles-wave simulation was performed with 40000 particles. The velocity half width is $\Delta v_0 = 0.001$.

5.4.3 Time Span for the Laminar Regime

The laminar regime extends up to the point where the fluid description based on single valued contours breaks down. From that point on, mixing process starts and the laser growth ceases. The breakdown time z_b is a critical time scale for our problem. We find this time when the compressibility develops discontinuities in the nonlinear model. In the particles-wave simulations the criterium adopted to determine the breakdown time is that this time occurs when the lower border of the distribution is no longer a single valued function.

Fig. 5.6, built for $a_w = 0.4; a(z = 0) = i\, a_w\, 10^{-5}; v_p = 0.99; \eta = 0.03$, shows a comparison between the results for z_b for the model and for the simulations. The breakdown time does not depend too heavily on the initial spread Δv_0, exactly as it had been revealed in Ref. [30]. Basically, it occurs

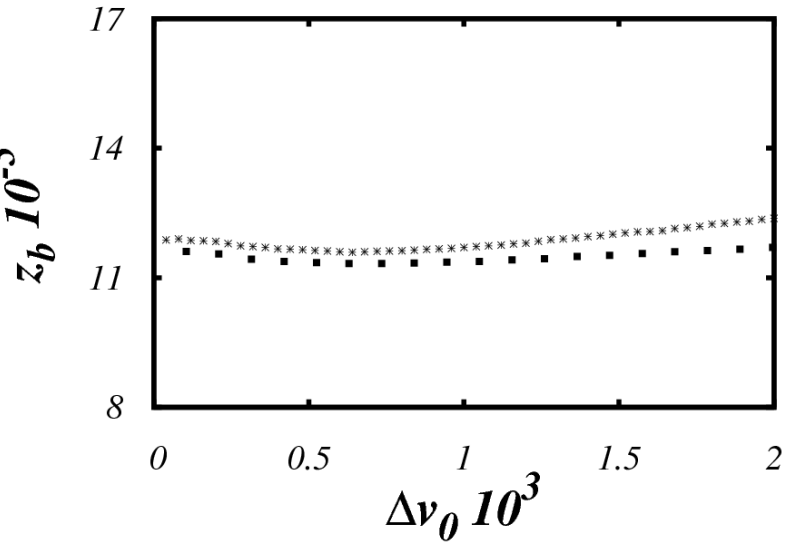

Fig. 5.6: Plots of z_b *versus* the spread Δv_0, both from particles-wave simulations (filled squares) and model (stars).

because we are investigating a hydrodynamic regime, where the gap between the ponderomotive wave velocity and the beam velocity is larger than de velocity spread. Besides this weak dependence, the crucial feature is the way the breakdown takes place[18].

The breakdown time z_b is associated with density discontinuities of warm beams, the discontinuities evolving into divergences as Δv_0 goes to zero[18].

5.4.4 Saturation Peak of the Stimulated Laser

After the breakdown time, the onset of saturation process of the FEL interaction takes place. With the value of the laser field amplitude for the breakdown time is possible to estimate the intensity of the first peak of radiation.

Given the relative accuracy of the linear approximation up to breakdown, we let the linear system evolutes in time until the breakdown. Then, we freeze the bunching factors X and Y at that time. This is an attempt to emulate the saturated state. With the collective variables X and Y freezed, the

Δv_0	a_{simul}^{peak}	a_{model}^{peak}
0.0002	0.026	0.028
0.0006	0.023	0.019
0.0011	0.019	0.014
0.0015	0.015	0.012
0.0020	0.012	0.009

Tab. 5.1: Comparison of full simulations and analytical estimates for the first peak of the laser amplitude.

laser amplitude oscillates. Thus, we capture the maximum amplitude in this oscillatory motion. To freeze the collective variables is equivalent to consider that the electric density has a (poor) remaining coherence yet.

The comparison between the results given by the simulations and the model are shown in Tab. 5.1. A graphical representation for the model can also be seen as the dashed curve of Fig. 5.7, where we indicate the modeled (circle) and particles-wave simulated (triangles) breakdown times.

It is important to notice, in Tab. 5.1, that the peak decreases as the spread increases. This is a typical feature for FELs: as the spread increases, less particles participate in the FEL interaction.

The hypotheses of linearity and of a strictly constant bunching in the mixing phase introduce additional approximations to the model, but in spite of these the table still reveals a reasonable agreement between simulations and model. Considering the simplicity of the steps adopted here to estimate the peak, we believe that the table serves its purposes[18].

5.4.5 Role of Space-Charge

In this Chapter, all of the results were shown for $\eta = 0.03$, which corresponds to a Raman regime. To completely understand role of space-charge in the system dynamics, we varies the value of η and make a discussion based on Fig. 5.8, that has been build with the particles-wave simulations and with the model, and the results agreed very well. To evaluate the density discontinuities in a quick and reliable way, we uniformly partition the horizontal θ axis of the density plots into a large number of discrete elements and select the one with the largest density variation at the breakdown time. For the

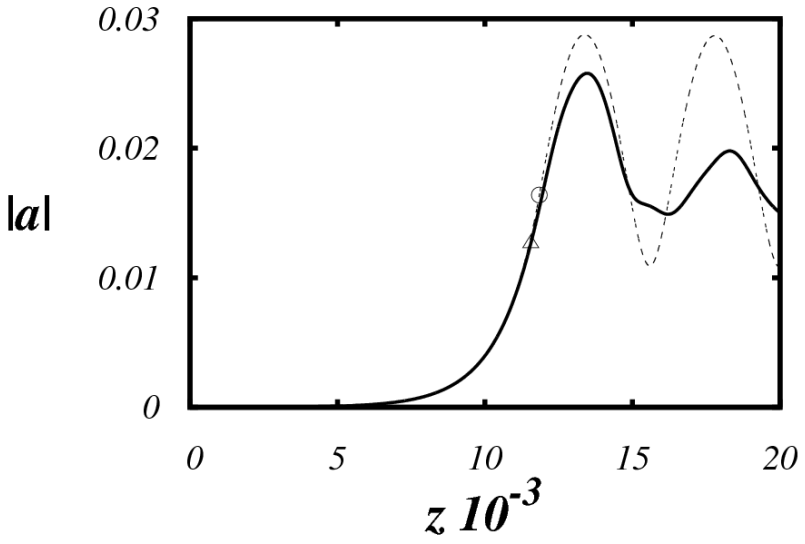

Fig. 5.7: Amplitude of the stimulated radiation against time: particles-wave simulations represented by the solid line, approximate model based on estimated values for the bunching factors represented by the dotted line. Circle (triangle) indicates the breakdown time according to the model (particles-wave simulations); $\Delta v_0 = 0.0002$.

model, 100 to 150 partitions elements were used to produce the results[18].

Panel (a) represents the size of the density discontinuity as a function of η. This panel was made for two different initial spreads ($\Delta v_0 = 0.0002$ and $\Delta v_0 = 0.0004$), and in both cases, the size of the density discontinuities decrease as η increases. We can briefly look at Eq. 5.38: in this equation, the coefficient e has a term that depends on η and another one that depends on Δv_0. The increase of η makes the relative contribution of the spread to be less important. Thus, the size of the discontinuity is bigger (the extreme case is a cold beam, which has an infinite discontinuity). Basically, the space-charge acts in a way that if it increases, the importance of the spread becomes smaller.

In the panel (b), the breakdown time z_b is plotted *versus* η for two different initial spreads. The breakdown time, as seen in Fig. 5.8, weakly depends on the initial spread (for the same η). It is interesting to see that z_b decreases as η increases. Smaller values of η are associated with slower dynamics and larger breakdown times, the expected result arising from shallower ponderomotive wells.

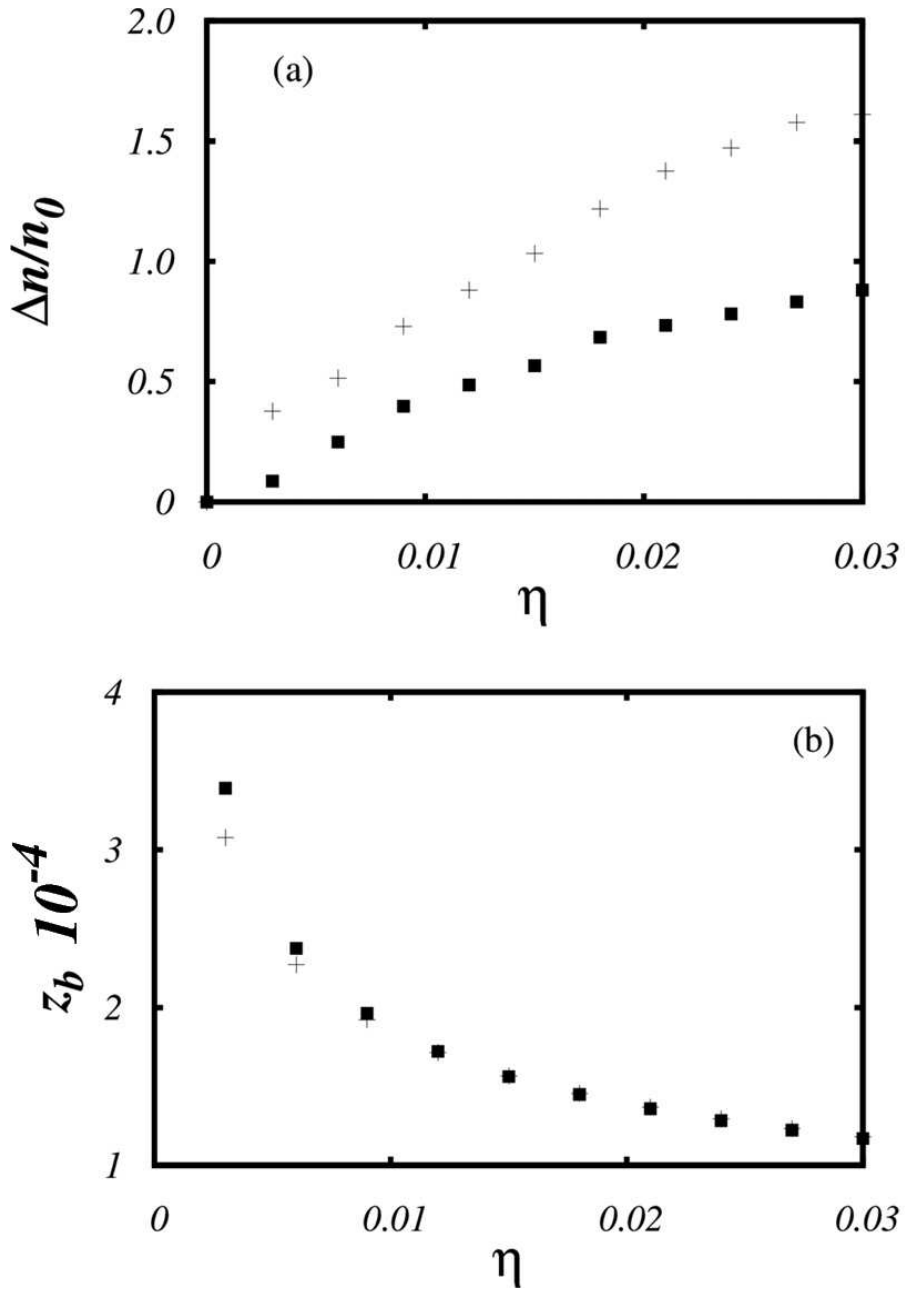

Fig. 5.8: Effect of space-charge on the density discontinuities (a) and on the breakdown time (b). Crosses represent $\Delta v_0 = 0.0002$ and filled squares $\Delta v_0 = 0.0004$.

At larger value of η, region of hydrodynamical regimes, z_b, is quite insensitive to the spread. This is what we commented earlier when we discussed the relative constancy of z_b against the spread, seen in Fig. 5.8. However, when we abandon the hydrodynamical regimes at small η's, the spread

can no longer be considered a small term, acquiring a noticeable effect on the breakdown time. Panel (b) complements the information gained earlier in the text, when we focused attention on the hydrodynamical regimes.

5.5 Gaussian Initial Distribution

In the nonlinear model presented in this work, the water bag distribution was considered, for simplicity, as the initial distribution for the velocities. However, the energy distribution for the beam is better described by other distributions, as Gauss distribution.

It would be interesting to verify the agreement between the nonlinear model and the integration of the particles-wave equations for initial Gauss velocity distribution by the comparison of their results.

Typically, the Gauss distribution function is expressed as:

$$f_{Gauss}(v) = Ce^{-\frac{(v-\bar{v})^2}{2\sigma^2}}, \tag{5.42}$$

where σ is the standard deviation, $\bar{v}$ is the mean velocity and C is a normalization constant:

$$C = \frac{1}{\int e^{-\frac{(v-\bar{v})^2}{2\sigma^2}} dv}. \tag{5.43}$$

Gauss distribution for the initial velocities is symmetrical in relation to the mean velocity, as can be seen in Eq. 5.42.

The initial distribution is illustrated in Fig. 5.10. The colors indicate the electronic density in the corresponding region of the phase-space (red/green color represents the bigger/smaller densities). The longitudinal distribution, as can be seen, is homogeneous, i.e., the distribution function has not θ dependence. For the simulations, the distribution was limited to the range between $\bar{v} - 3\sigma$ and $\bar{v} + 3\sigma$ to make possible to emulate an initial situation of equilibrium.

In order to compare the different distributions, we must define an equivalent parameter in terms

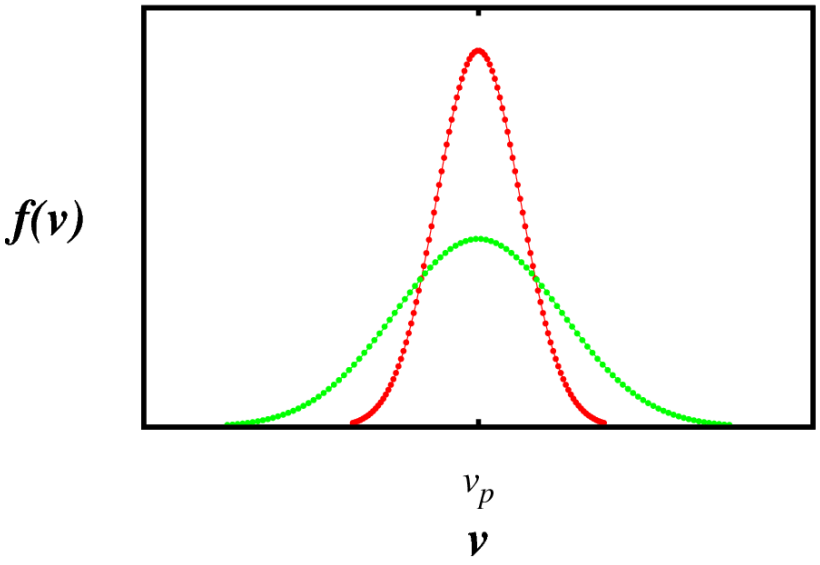

Fig. 5.9: Gauss distribution $f(v)$ for $\sigma = 0.001$ is expressed by the red solid line (filled circles), while Gauss distribution for $\sigma = 0.002$ is expressed by the green solid line (filled circles).

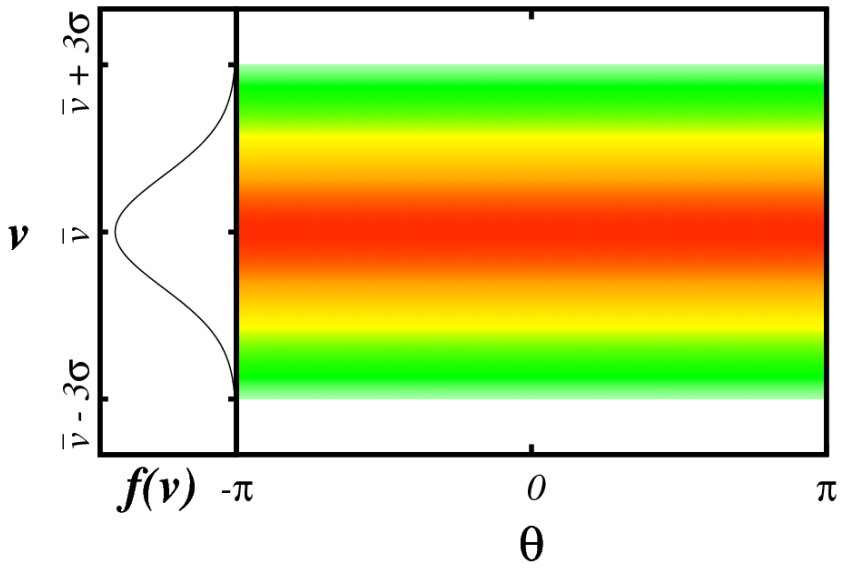

Fig. 5.10: Graphic representation of the Gaussian distribution $f(v)$. The colors indicate the electronic density: red color corresponds to higher densities. The distribution is limited to the region between $v_p - 3\sigma$ and $v_p + 3\sigma$.

of the spread. For this, we consider that the area of the distribution function is equivalent to the probability to find a particle in the limits of this area.

Thus, in the hydrodynamical regime, we assume the Gaussian distribution could be composed by a sum of water bag distributions, with different half-widths (Δv_0), as shown in Fig. 5.11. It allows us to find an equivalent half-width for the Gaussian distribution:

$$\Delta v_{0_{eq}} = \sum_{1}^{N} \Delta v_{0,i} A_i, \tag{5.44}$$

where A_i is the area of the i-th water bag distribution and N is the number of water bag distributions to compose the original distribution with the normalization condition that:

$$A = \sum_{1}^{N} A_i = 1, \tag{5.45}$$

where A is the total area bellow the distribution curve.

On the other hand, the i-th area is a function of $\Delta v_{0,i}$ and its limited by the thickness considered for $f(v)$, which is expressed by:

$$t = \frac{f_{max}}{N}, \tag{5.46}$$

where t is the thickness considered for $f(v)$, f_{max} is the maximum value of $f(v)$ and N is, once again, the number of water bag distributions to compose the original distribution.

This way is possible to establish a connection between σ and Δv_0. This equivalence is shown in Tab. 5.2 for $v_p = \bar{v} = 0.99$.

5.5.1 Results

The detuning which maximizes the laser growth rate is shown *versus* the equivalent spread in Fig. 5.12 for $a_w = 0.4; a(z=0) = i\, a_w\, 10^{-5}; \eta = 0.03; v_p = 0.99$ (the value of η is maintained constant in this section $-$ the role of the space-charge effect was already discussed in Subsection 5.4.5). The

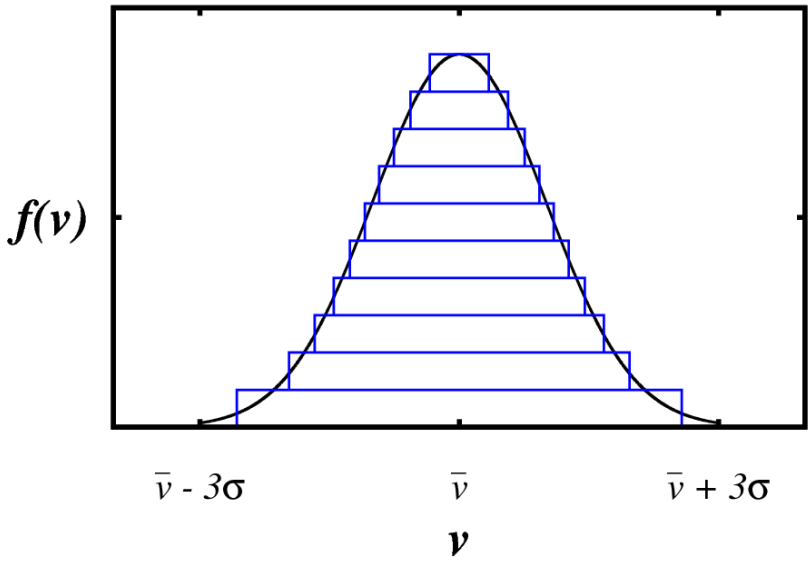

Fig. 5.11: The original distribution can be expressed through a sum of water bag distributions, exactly as shown in this figure.

solid line is the result obtained through the nonlinear model, while the black filled circles are obtained *via* the integration of the particles-wave equations for a water bag distribution, using 20000 particles. Finally, the red filled circles are from the integration of the particles-wave equations for a Gaussian distribution (with its corresponding equivalent spread), using 40000 particles. The results shows a good agreement between the different distributions.

Although the detuning which maximizes the radiation growth rate is similar for water bag and Gaussian distributions, the effective value of the laser growth rate must be compared. As it was already mentioned in this work, until the breakdown of the laminar regime, the laser growing is almost linear. Thus, the logarithm of the modulus of the laser field amplitude ($log\,|a|$) could be fitted to a straight line, where τ is the slope $-$ corresponding to the growth of the laser field.

In Fig. 5.13, the growth rate τ of the laser field is compared for the different distributions, over the curve of maximum growth rate shown in Fig. 5.12. The solid black line was obtained through particles-wave simulations of water bag distributions, while the red filled circles were obtained from the particles-wave simulations of Gaussian distributions.

σ	Δv_{0eq}
0.0001	0.000158
0.0002	0.000316
0.0003	0.000474
0.0004	0.000633
0.0005	0.000791
0.0006	0.000949
0.0007	0.001107
0.0008	0.001265
0.0009	0.001423
0.0010	0.001580

Tab. 5.2: Variance of the Gaussian distribution σ and its equivalent spread Δv_{0eq}.

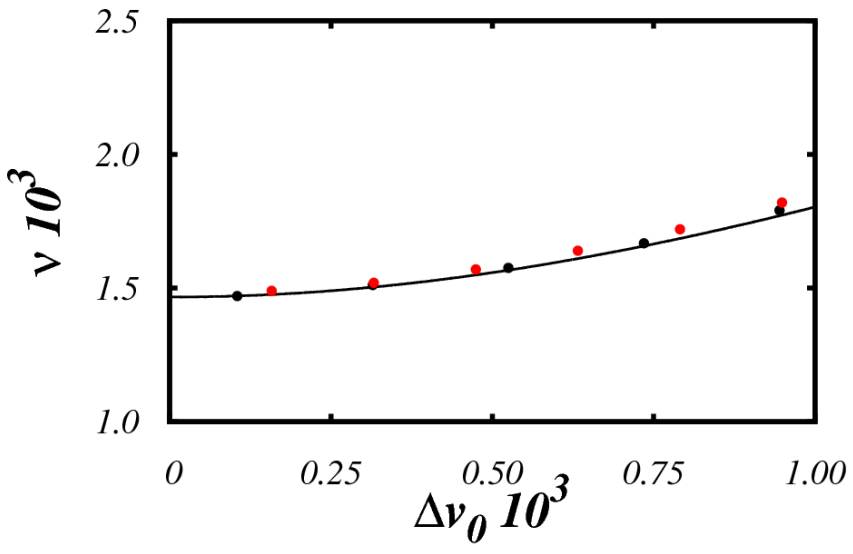

Fig. 5.12: The detuning ν that maximizes the laser growth rate *versus* the equivalent initial velocity spread. The solid line is from the nonlinear model. Black (red) filled circles are the results from the particles-wave simulations for the water bag (Gaussian) distribution.

The results well agree until $\Delta v_0 \sim 0.0007$. This point forward, the growth rates begin to diverge. The reason for that is quite simple: spreads, naturally, decrease the growth rate, but with greater deviations (σ), an increasing fraction of particles ceases to interact with the system, because an increasing fraction of particles has velocities much different to the ponderomotive field one (we remember here that Gaussian distribution is distributed over a velocity-range larger in comparison to the wa-

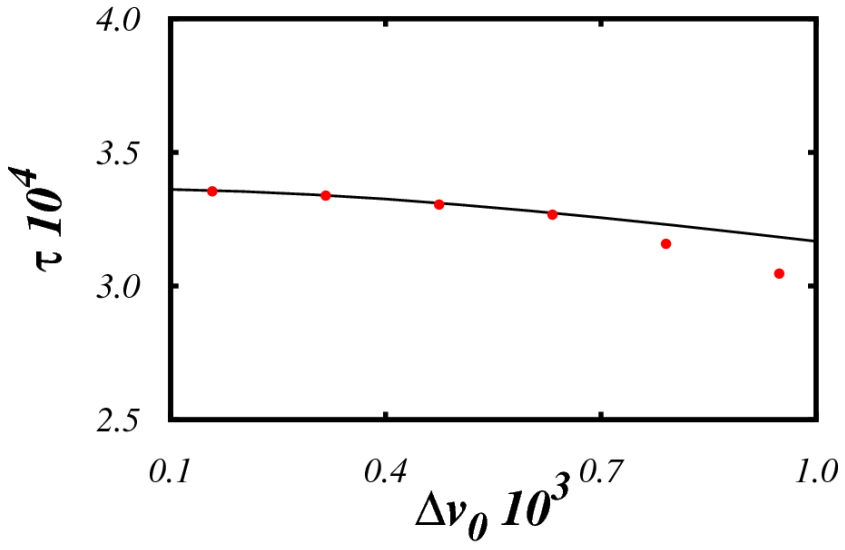

Fig. 5.13: The linear coefficient of the growth rate τ is plotted *versus* the equivalent initial spread Δv_0. The solid line is from water bag distributions and the filled circles are from Gaussian distributions. The results were performed through particles-wave simulations.

ter bag distribution), then the ponderomotive field is not able to trap these particles. The immediate consequence is the decreasing of the growth rate.

The evolution of the laser amplitude of the water bag and the Gaussian distributions is shown in the panel (a) of Figs. 5.14 and 5.15. In Fig. 5.14, $\Delta v_{0_{eq}} = 0.000158$ ($\sigma = 0.0001$). The evolution of the stimulated amplitude is quite similar for the both distributions, it occurs due the growth rate, as can be seen in Fig. 5.13. The time until the breakdown of the laminar regime is quite similar in this case ($z \cong 11500$). In Fig. 5.14(a) this time is expressed by a circle, in the case of the water bag distribution, and by a cross, in the case of the Gaussian distribution. The criterium adopted to determine the breakdown of the laminar regime is the same for the both distributions: the breakdown occurs when the lower border of the distribution becomes a non-single-valued function anymore (however, the linear regime still occurs for a while after this time).

In the panel (b) of Fig. 5.14 is shown a snapshot of the phase-space just after the breakdown. The colors indicate the electronic density (where red/green are used for larger/smaller values of the

local density). We may see that the electronic distribution still resemble the initial distribution $-$ *it is, actually, a good evidence to allow us to use the superposition of the water bag distributions*. The panel (c) shows the electronic density in the phase-space for the water-bag initial distribution just after the breakdown. It is possible to see that the distribution is almost constant over the occupied area (once again, the colors indicate the value of the electronic density). This condition was used to formulate the nonlinear model.

Fig. 5.15 was built for $\Delta v_{0_{eq}} = 0.000632$ ($\sigma = 0.0004$). Panel (a) shows that the evolution of the laser field amplitude diverge a little between Gauss (green line) and water bag (red line) initial distributions. Through Fig. 5.13 is possible to realize this difference. The green/red line was obtained from the Gauss/water bag initial distribution. The circle is the breakdown from the simulations. The star is the breakdown time and amplitude estimated by the nonlinear model. Although the growth is a little different between the distributions, the maximum value of the laser field is very close. The breakdown time $-$ using the criterium already mentioned $-$ differs $\sim 10\%$ between the distributions.

In the panel (b) of Fig. 5.15 is shown a snapshot of the phase-space just after the breakdown. The colors indicate the electronic density (where red/green are used for larger/smaller values of the local density). The electronic distribution still resemble the initial distribution. The panel (c) shows the electronic density in the phase-space for the water-bag initial distribution just after the breakdown. It is possible to see that the distribution is almost constant over the occupied area.

5.6 Conclusion

In this chapter, we presented a nonlinear model, based on the compressibility factor, able to deal with thermal effects, considering an initial water bag distribution for the velocities. A linear analysis was made to provide the optimal parameters to maximize the growth rate. The maximum growth rate curve given by the linear analysis was compared with the particles-wave one, showing a good agreement.

The compressibility factor is related to the electronic density in the laminar regime. When spatial

discontinuities occur, this is a sign of transition from laminar to mixing regimes. The discontinuities are associated to singular behavior of the lower boundary of the electronic distribution (in a very similar way that occurs with the cold beam case).

The laser amplitude was emulated, as in the cold beam case, by the linear set of equations (but now including the thermal effect), while the nonlinearities were described by a macroscopic phase equation (this equation is a partial differential equation).

The breakdown time is determined in simulations as the instant where the lower border of the distribution starts to twist around itself. One possibility is to pinpoint the onset of mixing through the abrupt growth of the beam emittance which has already been done in related systems[18, 30].

One also observes that our approximation on the connection between momentum and velocity is limited by the magnitude of the initial velocity spread Δv_0. However, given the narrow spreads in FELs[34], the linear connection is fairly accurate[18].

As we mention along the work, the present strategy based on the compressibility suggests a way to estimate the fraction of the electron population actively participating in the FEL interaction. Large and small discontinuities are, respectively, related to large and small fractions of participants: the larger the discontinuity, the larger the number of particles in the protruding finger. This issue and others, like the effects involved with the diffraction of the stimulated signal, are of relevance for the optimization and efficiency of the FEL interaction[18].

In general, the results, as can be seen in Section 5.4, given by the model were satisfactory in comparison to the particles-wave ones. It make us consider the model as a powerful tool to analyze FEL dynamics.

The results of a $1D$ FEL considering two different initial distributions were compared. We also compared the results with a nonlinear model proposed initially for water bag initial distribution. Although the differences between water bag and Gaussian distributions, the results well agree in the limit of very small spreads, as can be seen in Figs. 5.14 and 5.15. With small spreads, all of the particles are trapped by the ponderomotive potential, but with larger spreads, some particles do not interact effectively with the ponderomotive potential. The presence of particles beyond the limits of

the water bag distribution in the Gauss distribution is noticed in the growth rate for equivalent spreads ~ 0.0007. It is important to notice that the electronic density $-$ in both cases: water bag and Gaussian initial distributions $-$ still resemble with the initial distribution when the lower border becomes a non single valued function anymore $-$ *and it is actually a good evidence to allow us to use Eq. 5.44*. After this moment, the laser field amplitude still grows linearly for the Gaussian case: because the core of the distribution is more important to the system dynamics than the lower border or any other region.

As a final conclusion, this work shown that the nonlinear model is able to deal with the Gauss initial distribution for the longitudinal velocities in the limit of very small spreads, $-$ in the *hydrodynamical regime* $-$ but the model lacks to give precise data about the system when the initial spread is larger. In this limit, a kinetic theory must be made.

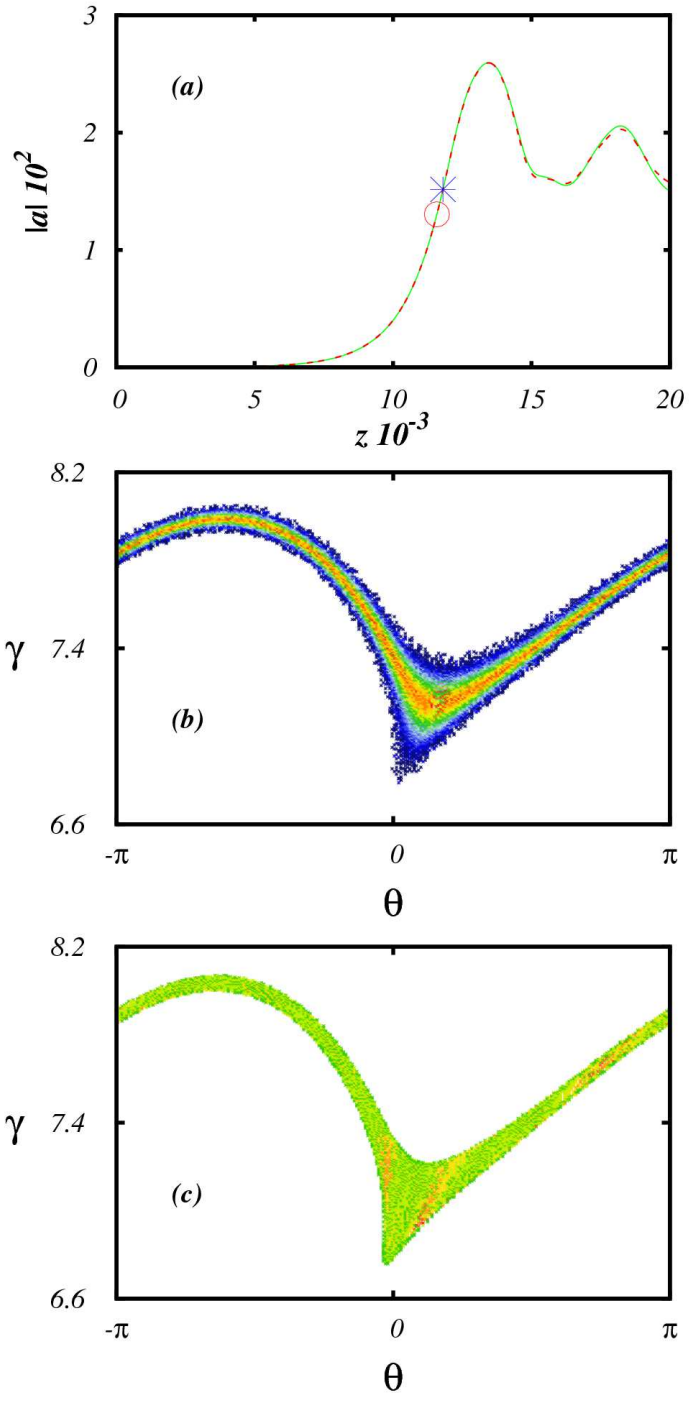

Fig. 5.14: In panel (a), it is plotted the evolution of the laser amplitude for the water bag (red curve) and Gaussian (green) initial distributions. Panel (b) and (c) show the electronic density (through colors − where red is the bigger value) in the phase-space for the Gaussian and water bag initial distributions, respectively. Parameters used: $a_w = 0.4, a(z = 0) = -i\,a10^{-5}, v_p = 0.99, \Delta v_0 = 0.000158, 40000$ particles.

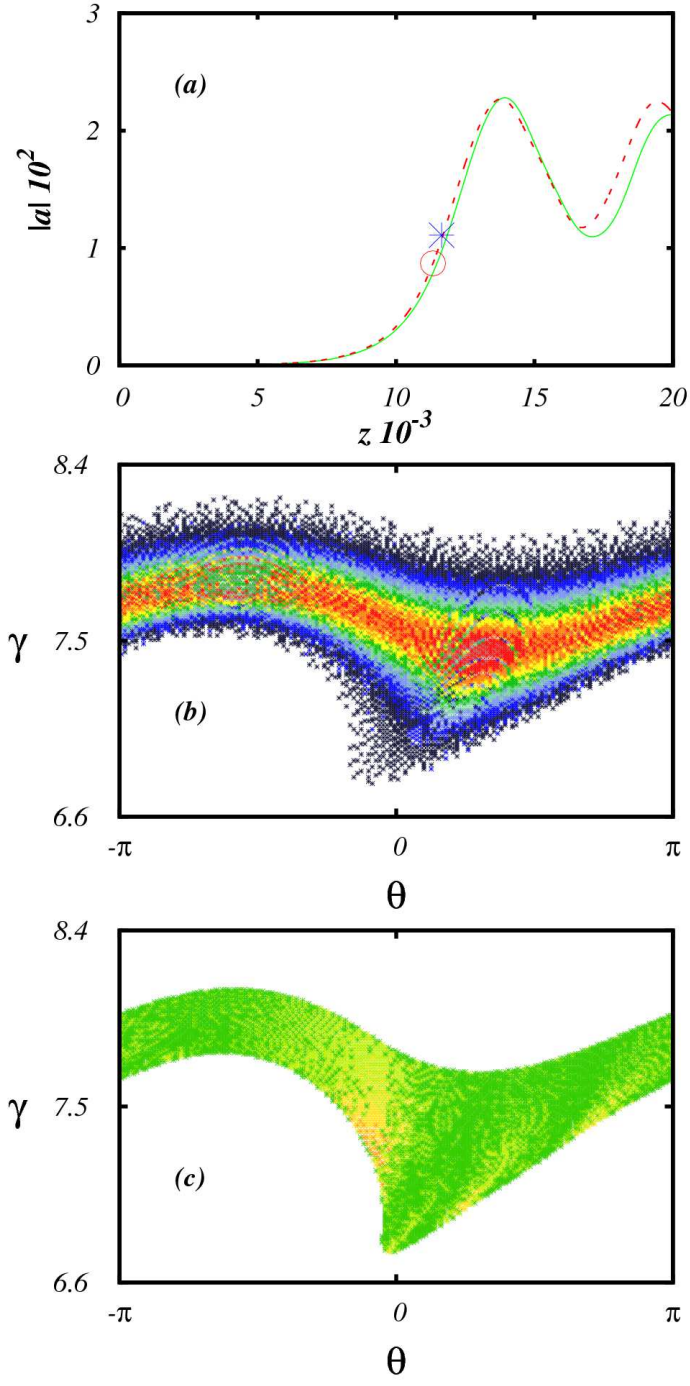

Fig. 5.15: In panel (a), it is plotted the evolution of the laser amplitude for the water bag (red curve) and Gaussian (green) initial distributions. Panel (b) and (c) show the electronic density (through colors – where red is the bigger value) in the phase-space for the Gaussian and water bag initial distributions, respectively. Parameters used: $a_w = 0.4, a(z = 0) = -ia_w 10^{-5}, v_p = 0.99, \Delta v_0 = 0.000632, 40000$ particles.

Chapter 6

Final Remarks

In this work we studied the Free-Electron Laser. We started from the very beginning, making a very short travel through the history of this device. The different types of FEL and wigglers were also mentioned.

The chosen FEL studied here was a single-pass configuration FEL. In this configuration, the laser growth occurs in only one passage of the beam through the wiggler. Equations for spontaneous regime and stimulated emission regime were shown, step by step. The limit of a single electron was explored to reach the famous pendulum-like FEL equation.

After this brief introduction, we derived the $1D$ FEL equations for the high gain regime. A scheme of the complete set of equations to fully describe the system was presented. Basically, to describe the FEL dynamics, we must the evolution of the laser field, the evolution of the electron phase (inside the ponderomotive potential), the evolution of the electron energy and, finally, some helpful relations, as the electron longitudinal velocity (how it relates with electron energy, electron phase and fields amplitudes) and the square of the modulus of the total vector potential amplitude.

A model based on the compressibility factor was developed to estimate some results of the FEL for a cold electron beam (no initial velocity spread), including longitudinal space-charge effects. To build the model, some considerations were made: initially, the particles were homogeneous distributed over the space; the laser growth is linear until the onset of mixing (the laser growth, then, is emulate by a

linear set of equations); the system starts from a *quasi-equilibrium* state − no initial fluctuations in phase.

The model proved to be reasonable to estimate: the linear growth rate; the detuning to maximize the growth rate; the time of the onset of mixing (we remember that the onset of mixing is defined when the particles distribution in phase-space is not a single valued function anymore) − the onset of the mixing occurs in the model when the compressibility factor vanishes (it corresponds to a infinite local density); the saturated amplitude of the stimulated radiation; and, the most important, the boundary between the Compton and Raman regimes.

A nonlinear model to deal with thermal effects was proposed as well, considering the beam as a fluid for water bag initial distribution. The model proved to be reasonable in the hydrodynamical regime, i.e., for very small initial spreads. The laser field evolution was emulated by a linear set of equations (with the inclusion of a pressure term, with compete with ponderomotive potential), while the nonlinearities of the problem were introduced through the space-charge and thermal effects.

The compressibility factor is also helpful in this analysis. The mixing (breakdown of the laminar regime) in phase-space starts when singularities appears in the compressibility or in the electronic density. Actually, the process is understood as collisions among fronts of different densities at the same phase coordinate. The breakdown is defined in the particles-wave simulations when the lower border of the distribution becomes a non single valued function anymore.

The nonlinear model gave good estimations about (in comparison with the particles-wave simulations): the time of the breakdown z_b; the longitudinal density distribution at z_b; the maximum value of the radiation field amplitude; and, the value of ν to maximize the laser growth rate.

The model was developed for water bag initial distributions. We extended the model by applying it to a Gauss initial distribution. For that, we considered, in the hydrodynamical regime, the Gauss distribution could be expressed as a sum of water bag distributions. Basically, the idea behind this assumption is the superposition of different fluids, with different densities, which produces a total pressure.

The extension proved to properly work for very small spreads. A snapshot just before the break-

down of the laminar regime shows that the distribution still resemble the initial distribution (what is necessary for the theory applied). The model estimates well the linear growth rate and the detuning needed to maximize the laser growth rate.

As a final conclusion, the model proposed, based on the compressibility factor, seems to be a helpful tool to analyze the FEL dynamics.

6.1 Future Perspectives

In the present work, we considered a $1D$ FEL. The transverse space-charge effects were ignored. For a better understanding of the FEL, these effects must be included. A more detailed thermal comprehension demands a kinetic theory treatment. These two consideration could be studied in next works.

FELs are devices with a promising future, due their tunability and efficiency. But, unfortunately, the manufacturing process of wigglers impose some physical restrictions about the distance between the magnets λ_w. The immediate consequence of this limitation is the beam energy needed to generate shorter wavelengths radiation must be higher (to remember: $\lambda = \left[\left(1 + {a_w}^2\right)/2\gamma^2\right]\lambda_w$). It demands more powerful (and physically larger) particles accelerators and, evidently, more costs[36, 39, 40].

As a future work, we suggest the study of this kind of configuration, exploring the co-propagating and the counter-propagating wiggler waves, and a similar analysis to build a simplified model.

References

[1] C. Pellegrini. The history of x-ray free-electron lasers. *The European Physical Journal H*, 37(5):659–708, 2012.

[2] C. Hitz, J. Ewing, and J. Hecht. *Introduction to Laser Technology*. New York: Wiley-IEEE Press, 2012.

[3] M. Csele. *Fundamentals of Light Sources and Lasers*. Hoboken, NJ: Wiley, 2004.

[4] H. Motz, W. Thon, and R. N. Whitehurst. Experiments on radiation by fast electron beams. *Journal of Applied Physics*, 24(7), 1953.

[5] John M. J. Madey. Stimulated emission of bremsstrahlung in a periodic magnetic field. *Journal of Applied Physics*, 42(5), 1971.

[6] G. Dattoli, A. Renieri, and A. Torre. *Lectures on the Free Electron Theory and Related Topics*. Singapore: World Scientific Publishing Company, 1993.

[7] D. A. G. Deacon, L. R. Elias, J. M. J. Madey, G. J. Ramian, H. A. Schwettman, and T. I. Smith. First operation of a free-electron laser. *Phys. Rev. Lett.*, 38:892–894, Apr 1977.

[8] Norman M. Kroll and Wayne A. McMullin. Stimulated emission from relativistic electrons passing through a spatially periodic transverse magnetic field. *Phys. Rev. A*, 17:300–308, Jan 1978.

[9] F. A. Hopf, P. Meystre, M. O. Scully, and W. H. Louisell. Strong-signal theory of a free-electron laser. *Phys. Rev. Lett.*, 37:1342–1345, Nov 1976.

[10] C.W. Planner. Numerical solutions to the non-linear phase equation for the free electron laser. *Physics Letters A*, 67(4):263 – 265, 1978.

[11] Bonifacio, R., Casagrande, F., Cerchioni, G., de Salvo Souza, L., Pierini, P., and N. Piovella. Physics of the high-gain fel and superradiance. *La Rivista del Nuovo Cimento (1978-1999)*, 13(9):1–69, 1990.

[12] J. A. Pasour, eds: R. Wayant, and M. Ediger. *Free electron lasers. Electro-Optics Handbook*. McGraw-Hill, Chapter 8, 2000.

[13] G. Marcus, E. Hemsing, and J. Rosenzweig. Gain length fitting formula for free-electron lasers with strong space-charge effects. *Phys. Rev. ST Accel. Beams*, 14:080702, Aug 2011.

[14] F. B. Rizzato. Dispersive effects on the main-wave modulational instability in free-electron lasers. *Phys. Rev. A*, 41:1629–1633, Feb 1990.

[15] R. B. Miller. *An Introduction to the Physics of Intense Charged Particle Beams*. Cambridge: Plenum Press, 1982.

[16] E. Peter, A. Endler, F. B. Rizzato, and A. Serbeto. Mixing and space-charge effects in free-electron lasers. *Physics of Plasmas*, 20(12):–, 2013.

[17] E. A. Peter, A. Endler, F. B. Rizzato, and A. Serbeto. Mixing and space-charge effects in free-electron lasers. In *6th International Particle Accelerator Conference, 2015. IPAC 2015. Proceedings of the*, volume 1, pages 1410–1412, 2015.

[18] E. Peter, A. Endler, and F. B. Rizzato. Nonlinear model for thermal effects in free-electron lasers. *Physics of Plasmas*, 21(11):–, 2014.

[19] G.R. Neil. Fel oscillators. In *Particle Accelerator Conference, 2003. PAC 2003. Proceedings of the*, volume 1, pages 181–185 Vol.1, May 2003.

[20] M. V. Yurkov E. L. Saldin, E. A. Schneidmiller. *The Physics of Free Electron Lasers*. Springer Berlin Heidelberg, 2000.

[21] M. S. Livingston and J. P. Blewett. *Particle Accelerators*. London: McGraw-Hill Company, 1962.

[22] P. Luchini and H. Motz. *Undulators and Free-Electron Lasers*. Oxford: Clarendon Press, 1990.

[23] P. Sprangle, Cha-Mei Tang, and W. M. Manheimer. Nonlinear theory of free-electron lasers and efficiency enhancement. *Phys. Rev. A*, 21:302–318, Jan 1980.

[24] J.B. Murphy, C. Pellegrini, and R. Bonifacio. Collective instability of a free electron laser including space charge and harmonics. *Optics Communications*, 53(3):197 – 202, 1985.

[25] Yoonho Seo and E.H. Choi. A submillimeter raman free-electron laser in a dense plasma background. *Plasma Science, IEEE Transactions on*, 25(2):360–363, Apr 1997.

[26] M. Wang, X. Xiao, and Z. Liang. Nonlinear study on raman regime free electron laser with elliptical waveguide. *Journal of Physics D: Applied Physics*, 39(15):3332, 2006.

[27] F. B. Rizzato, R. Pakter, and Y. Levin. Wave breaking and particle jets in intense inhomogeneous charged beams. *Physics of Plasmas*, 14(11):–, 2007.

[28] E. G. Souza, A. Endler, R. Pakter, F. B. Rizzato, and R. P. Nunes. The controlling role of envelope mismatches in intense inhomogeneous charged beams. *Applied Physics Letters*, 96(14):–, 2010.

[29] A. Antoniazzi, D. Fanelli, J. Barré, P.-H. Chavanis, T. Dauxois, and S. Ruffo. Maximum entropy principle explains quasistationary states in systems with long-range interactions: The example of the hamiltonian mean-field model. *Phys. Rev. E*, 75:011112, Jan 2007.

[30] E. G. Souza, A. Endler, F. B. Rizzato, and R. Pakter. Adiabatic-nonadiabatic transition in warm long-range interacting systems: The transport of intense inhomogeneous beams. *Phys. Rev. Lett.*, 109:075003, Aug 2012.

[31] T. C. Marshall. *Free-Electron Lasers*. New York: Macmillan Publishing Company, 1985.

[32] C. Brau. *Free-Electron Lasers*. Boston: Academic Press, 1990.

[33] H. P. Freund and T. M. Antonsen. *Principles of Free-Electron Lasers*. London: Chapman and Hall, 1996.

[34] A. Chakhmachi and B. Maraghechi. Stability properties of free-electron laser in raman regime with thermal electron beam. *Physics of Plasmas*, 16(4):–, 2009.

[35] T. P. Coffey. Breaking of large amplitude plasma oscillations. *Physics of Fluids*, 14(7), 1971.

[36] L. F. Monteiro, A. Serbeto, K. H. Tsui, J. T. Mendonça, and R. M. O. Galvão. Quantum fluid model of coherent stimulated radiation by a dense relativistic cold electron beam. *Physics of Plasmas*, 20(7):–, 2013.

[37] K. V. Lotov and I. V. Timofeev. Transition regime of the one-dimensional two-stream instability. *ArXiv e-prints*, August 2014.

[38] John M. Dawson. Nonlinear electron oscillations in a cold plasma. *Phys. Rev.*, 113:383–387, Jan 1959.

[39] Y. Seo. The nonlinear evolution of a free electron laser with electromagnetic wigglers. *Physics of Fluids B*, 3:797–810, March 1991.

[40] P. L. Similon and J. S. Wurtele. Depletion and diffraction of an electromagnetic wiggler field during the free electron laser interaction. *Physics of Fluids B*, 1(6), 1989.